THESIS

Active Vibration Isolation for a Laser Interferometric Gravitational Wave Detector using a Suspension Point Interferometer

懸架点干渉計を用いたレーザー干渉計型重力波検出器の能動防振

Yoichi Aso

Department of Physics, Faculty of Science,
University of Tokyo.

January 2006

Abstract

Gravitational waves are distortions of spacetime which propagate through space as waves. It was theoretically predicted by Einstein about 90 years ago as a consequence of his theory of general relativity [1]. The indirect evidence for the existence of gravitational waves was found by Taylor and Hulse [2]. They discovered a binary system which is composed of a pulsar and a companion neutron star. From the long term precise observations of the pulsar frequency, the decay rate of the orbital period was found to be consistent with the prediction from the energy loss due to the gravitational radiation. For this discovery, they were awarded the Nobel prize in physics in 1993. Nonetheless, no one has succeeded in the direct detection of gravitational waves up to the present. This is because the interaction of gravitational waves with matter is extraordinarily weak.

Currently there is an array of large scale interferometric gravitational wave detectors in operation around the world. The detection of gravitational waves will open a new window to look at universe for us, bringing us information about dynamic astronomical phenomena, such as the coalescence of neutron stars and the consequent formation of a black hole, gravitational collapse of the heavy cores of old stars, and even the inflation of the universe just after its birth. This type of information has never been available with observations using electro-magnetic waves.

To realize an interferometer with enough sensitivity to detect weak effects of gravitational waves, various noises have to be reduced. Among the noises, the seismic vibration is one of the most serious noise sources at low frequencies. The mirrors of an interferometer are suspended by wires as pendulums in order to attenuate the seismic noise at the observation frequencies. This is a passive way of vibration isolation. All of the large-scale interferometers currently in operation employ this approach. However, the vibration isolation provided by simple pendulums is no longer sufficient when it comes to the next generation interferometers. Therefore, better vibration isolation mechanisms are needed, especially one which is effective at low frequencies.

This thesis focuses on an active vibration isolation scheme called suspension point interferometer (SPI), which provides additional vibration isolation to passive suspension systems and works effectively at very low frequencies. The SPI was originally proposed by Drever many years ago [3]. The SPI scheme makes use of an auxiliary interferometer for active suppression of seismic vibration. The auxiliary interferometer is installed at the suspension points of the mirrors for the main interferometer; thus the auxiliary interferometer is called the suspension point interferometer. The vibrations transmitted from the

ground through the suspension wires are first detected by the SPI. Then the servo system of the SPI exerts forces on the mirrors of the SPI to cancel the vibration. In this way, the transmission of the vibration to the mirrors of the main interferometer is blocked by the SPI.

In the first chapter of this thesis, the basics of interferometric detection of gravitational waves are briefly reviewed. In the second chapter, the principle and the theoretical performance of the SPI are examined along with the advantages of this scheme. Then an experiment to confirm the principle and study the practical performance of an SPI is explained. The experimental setup is a Fabry-Perot interferometer of 1.5 m long equipped with an SPI and a rigid-cavity mode cleaner. With this apparatus, the enhancement of the vibration isolation using the SPI by a factor of 100 at maximum was observed with spectral measurements below 10Hz, down to very low frequencies (below 0.1 Hz). The total residual motion of the mirrors was reduced by a factor of 9.

Those are encouraging results for the application of this scheme to next generation large scale interferometers.

要約

重力波とは、時空の歪みが波のように伝わっていく現象である。この現象は、一般相対性理論の帰結として、アインシュタインによって約 90 年前に予言された [1]。また、重力波の存在に対する間接的な証明は、Taylor と Hulse によってなされた [2]。彼らは、片方がパルサーである連星中性子星系を発見したのである。長期間にわたるパルサー周期の精密な観測から、軌道周期の減少率が重力波の放出による理論的な予言と一致することがわかった。この発見によって、彼らは 1993 年のノーベル物理学賞を受賞した。しかし、現在までのところ、誰も重力波の直接検出には成功していない。これは、重力波と物質との相互作用があまりにも弱いためである。

現在世界中に干渉計型重力波検出器のネットワークが完成しつつある。重力波の直接検出は宇宙を見る新しい窓を開くとともに、中性子星の合体やそれに伴うブラックホールの形成、星のコアの重力崩壊、さらには宇宙開闢直後のインフレーションからの重力波など、ダイナミックな天体現象に関する情報を我々にもたらしてくれる。このような情報は、従来の電磁波による観測では得ることができない。

重力波の直接検出が可能な高感度の干渉計を作るには、様々な雑音を低減しなければならない。その中でも、地面振動は低周波に於いて最も深刻な雑音源の一つである。観測帯域に於いて地面振動を減衰させるために、干渉計の鏡はワイヤーに吊られている。これは受動的な防振方法であり、大型干渉計は全てこの方法を用いている。しかし、次世代干渉計のためには単純な振り子による防振では不十分である。そこで、よりよい防振方法、特に低周波で高性能なものが必要となる。

この論文は、Suspension Point Interferometer (SPI) と呼ばれる能動防振方法について書かれている。SPI は Drever によって考案された方法で [3]、受動防振装置に対して付加的に防振性能を上積みし、低周波に於いても性能を発揮する。SPI では補助的な干渉計を用いて、能動的に振動を抑制する。この補助干渉計は、メイン干渉計の鏡の懸架点 (Suspension Point) に構成される。従ってこれは Suspension Point Interferometer と呼ばれる。ワイヤーを伝わってきた地面振動は、まずこの SPI によって検出される。SPI のサーボシステムは、この振動を打ち消すような力を SPI の鏡に加える。これによって、主干渉計の鏡への振動伝達はブロックされる。

この論文では、SPI の原理と、その理論的性能、利点などがまず調べられる。そして、この原理や、現実的な性能などを調べるための実験について述べられる。実験装置は、1.5 m の Fabry-Perot 干渉計で、SPI と固定キャビティによるモードクリーナーを備えている。この装置を用いたスペクトル測定では、10 Hz 以下、0.1 Hz 程度の非常に低周波まで、最大 100 倍の、SPI による防振性能の向上が見られた。また、鏡の残留振動は、約 9 分の 1 に抑えられた。

これらの結果は、次世代干渉計へこの技術を応用する上で有用である。

Acknowledgements

I am indebted to my supervisor Kimio Tsubono for constant support and patient encouragement he gave me to accomplish this work. Masaki Ando has always been my first person to ask for advice. His practical advice based on the deep experience on interferometric experiments was invaluable help for me. I am also greatly obliged to Shigemi Otsuka and Yoshikatsu Nanjo for their help to manufacture the suspension systems of my experiment. Without their help, this experiment would have never been accomplished.

I had the great fortune to work with Riccardo DeSalvo at California Institute of Technology. The design and production of the MGAS filters was made possible with the help of him and Virginio Sannibale. A great deal of gratitude goes to Szabolcs Márka for his encouragement and proof reading of this thesis. I am also thankful to Michael Hall, Kelin Wang, and Hareem Tariq for their support to my life in the United States and useful discussions. I really respect Ron Drever for his inventions of various technologies for interferometric gravitational wave detectors including the suspension point interferometer, and I am grateful from my heart to him for the useful discussions and encouragement. I am thankful to Albrecht Rüdiger, Norna Robertson, Rana Adhikari and Richard Savage for being interested in my experiment and their kind encouragement.

I am thankful to the following people: Noritaksu Mio for negotiating with Japan Aviation Electronics to make the mirrors for the mode cleaner. Takamori Akiteru for useful discussions on the suspension systems and providing me with the transfer functions of the LCGT suspension system. Takashi Uchiyama for providing me with the results of his simulation on the vibration attenuation of the heat links by SPI. Michael Forgan for patiently proof reading this thesis. Kenji Numata and Koji Arai for giving me a lot of insights and good stimulations. Koji Ishidoshiro for patiently soldering a lot of electric circuits for me. Keita Kawabe was my first adviser when I started to work on this subject more than six years ago. His encouragement was a great help for me.

A part of this research was supported by a Grant-in-Aid for JSPS Fellows and a Grant-in-Aid for Scientific Research on Priority Areas (415) of the Ministry of Education, Culture, Sports, Science and Technology.

Finally, I am thankful to my parents for their patient encouragement and support. I also cannot be more grateful to my wife Shoko for her irreplaceable support.

To Lucky

Glossary

Here commonly used terms, abbreviations, and symbols throughout this thesis are listed with a brief description.

BS: Beam Splitter.

c: The speed of light, $c = 3 \times 10^8\,\mathrm{m/s}$.

δ**:** One way phase change of a Fabry-Perot cavity. $\delta = L\Omega/c$, where L is the length of the cavity.

e**:** The elementary charge.

EOM: Electro-Opto Modulator.

f**:** Frequency in Hz.

$\mathcal{F}$**:** Finesse of a Fabry-Perot cavity.

FDT: Fluctuation-Dissipation Theorem.

g**:** The gravitational acceleration of the Earth.

G**:** The gain of a control loop, or Newton's gravitational constant.

$g_{\mu\nu}$**:** Metric tensor.

$\Gamma^{\lambda}_{\mu\nu}$**:** Christoffel symbol.

h **or** $h_{\mu\nu}$**:** The amplitude of a gravitational wave.

$\hbar$**:** The Plank's constant divided by 2π. $\hbar = 1.05457148 \times 10^{-34}\,\mathrm{m^2kg/s}$.

HWP: Half Wave Plate = $\lambda/2$.

k_{B}**:** Boltzmann's constant. $k_{\mathrm{B}} = 1.3806503 \times 10^{-23}\,\mathrm{m^2kg/s^2K}$

λ**:** Wavelength.

LCGT: Large-scale Cryogenic Gravitational-wave Telescope.

LD: Laser Diode.

LIGO: Laser Interferometer Gravitational-wave Observatory.

LISA: Laser Interferometer Space Antenna.

MC: Mode Cleaner.

MGAS: Monolithic Geometric Anti-Spring.

MIF: Main Interferometer.

ω**:** Angular frequency [rad/sec].

Ω**:** Angular frequency of light.

PBS: Polarizing Beam Splitter.

PD: Photo Detector.

PDH: Pound-Drever-Hall.

PS: Photo Sensor.

PSD: Position Sensitive Detector.

PZT: Plumbum (lead) Zirconate Titanate. Often used to refer to a piezoelectric actuator.

QWP: Quarter Wave Plate = $\lambda/4$.

RIN: Relative Intensity Noise.

SPI: Suspension Point Interferometer.

SQL: Standard Quantum Limit.

Contents

Abstract iii

要約 v

Acknowledgements vii

Glossary ix

1 Interferometric Detection of Gravitational Waves 1
1.1 Gravitational Waves . . . 1
1.1.1 Metric Tensor and Gravity . . . 1
1.1.2 Linearized Einstein's Equation . . . 2
1.1.3 Monochromatic Plain-Wave Solution . . . 3
1.1.4 Interaction with Free Particles . . . 3
1.1.5 Polarizations . . . 4
1.1.6 Generation of Gravitational Waves . . . 5
1.2 Sources of Gravitational Waves . . . 6
1.2.1 Coalescence of Compact Binary Stars . . . 6
1.2.2 Burst Sources . . . 6
Ring-down of a Black Hole's Quasi-Normal Oscillation . . . 6
Supernova . . . 7
1.2.3 Continuous Wave Sources . . . 7
Pulsars . . . 7
Galactic Binaries . . . 7
1.2.4 Cosmological Sources . . . 7
1.3 Interferometric Gravitational Wave Detector . . . 8
1.3.1 Michelson Interferometer . . . 8
1.3.2 Response of a Michelson Interferometer to Gravitational Waves . . . 9
Frequency Response . . . 10
1.3.3 Fabry-Perot Interferometer . . . 11
Response of a Fabry-Perot Interferometer to Gravitational Waves 14
1.3.4 Noise Sources . . . 15
Shot Noise . . . 16

Radiation Pressure Noise . . . 17
Thermal Noise . . . 17
Seismic Noise . . . 18
Laser Noises . . . 19
Residual Gas Noise . . . 19
Control System Noise . . . 19
1.3.5 Current Projects . . . 20
TAMA . . . 20
LCGT . . . 20
LIGO . . . 20
GEO . . . 21
VIRGO . . . 21
LISA . . . 21

2 Suspension Point Interferometer 23
2.1 Suspension System of Interferometric Gravitational Wave Detectors . . . 23
2.1.1 Simple Pendulum Suspension . . . 24
2.1.2 Other Degrees of Freedom . . . 25
2.2 Active Vibration Isolation . . . 27
2.2.1 Accelerometer . . . 28
2.3 Working Principle of the SPI . . . 29
2.3.1 Rigid Bar Picture . . . 31
2.3.2 Response to Gravitational Waves . . . 31
2.4 Theoretical Performance . . . 32
2.4.1 Asymmetry of the Suspension . . . 32
2.4.2 Couplings from Other Degrees of Freedom . . . 34
2.4.3 Laser frequency noise . . . 36
2.4.4 Suspension Thermal Noise . . . 37
2.4.5 Noise of the SPI . . . 38
2.5 Applications to Advanced Detectors . . . 39
2.5.1 Seismic noise . . . 39
2.5.2 Vibration from Heat links . . . 39
2.5.3 RMS reduction . . . 40
2.5.4 Actuator noise . . . 40
2.5.5 Lock Acquisition . . . 41

3 1.5 m Prototype Fabry-Perot Interferometer 43
3.1 Optics . . . 44
3.1.1 Laser and mode cleaner . . . 44
Laser Bench . . . 44
Intensity monitor . . . 46
Mode Cleaner . . . 47
3.1.2 Main and Suspension Point Interferometers . . . 51

3.2 Suspension system . . . 53
3.2.1 Overview . . . 53
3.2.2 Sensors and Actuators . . . 53
Photo Sensor . . . 55
Coil-Magnet actuator . . . 55
Optical Lever . . . 56
3.2.3 MGAS filter . . . 56
Intuitive Interpretation of the Working Principle . . . 58
Theory of the MGAS filter . . . 60
Design Principle . . . 63
Practical Design Procedure . . . 64
Tuning . . . 67
3.2.4 Top Stage . . . 68
3.2.5 Damping Mass . . . 69
3.2.6 SPI Mirror . . . 72
3.2.7 Main Mirror and Recoil Mass . . . 74
3.3 Vacuum System . . . 77
3.4 Operation of the Interferometers . . . 79
3.4.1 Control System . . . 79
Intensity Stabilization . . . 79
Frequency Stabilization . . . 82
MGAS Filter Working Point Stabilization . . . 88
Length Control of the MIF and the SPI . . . 90
3.4.2 Alignment Adjustment . . . 92
3.4.3 Lock Acquisition . . . 92
3.4.4 Calibration . . . 93

4 Results **95**
4.1 Spectral Measurement . . . 95
4.2 Transfer Function Measurement . . . 98
4.2.1 Interpretation of the Measured Transfer Functions . . . 100
4.2.2 Asymmetry of the Main Pendulums . . . 101
4.3 Noise Estimation . . . 101
4.3.1 Seismic Noise . . . 102
4.3.2 Electronic and Detector Noises . . . 104
4.3.3 Laser Intensity Noise . . . 106
4.3.4 Laser Frequency Noise . . . 106
4.3.5 Other Noises . . . 108
Shot Noise . . . 108
Thermal Noises . . . 108
Residual Gas Noise . . . 109
4.3.6 Noise of the SPI . . . 110
4.3.7 Summary of the Noises . . . 110

5 Conclusion and Future Works **113**
5.1 Conclusion 113
5.2 Future Works 113
5.2.1 Alignment Mechanism 113
5.2.2 SPI at an Upper Stage of a Suspension System 114
5.2.3 Dual Band Interferometers 115

A Application to LCGT **117**
A.1 Attenuation of Vibrations Introduced from Heat Links 118
A.2 Reduction of the RMS Motion of the Mirrors 118
A.3 Works to be done for LCGT 122

B Pound-Drever-Hall scheme **123**

C Shooting Method **125**
C.1 Boundary Value Problem 125
C.2 Boundary Value Problem with Integral Constraint 126

D Vertical Suspension Point Interferometer **127**
D.1 Principle 127
D.2 Experiment 128

Chapter 1

Interferometric Detection of Gravitational Waves

In this chapter, the basics of interferometric gravitational wave detection are explained. First, the gravitational wave is derived as a wave solution of the linearized Einstein's equation. After its characteristics are explained, possible sources of gravitational waves for interferometric gravitational wave detectors are summarized. Then the principles of interferometric detection of gravitational waves are described. Finally, the current status of the large scale interferometric gravitational wave detectors around the world is reviewed.

1.1 Gravitational Waves

1.1.1 Metric Tensor and Gravity

In the theory of general relativity, spacetime structure is determined by a tensor $g_{\mu\nu}$, which is called "metric tensor"[1]. Using $g_{\mu\nu}$, the world distance between two events can be written as follows:

$$\Delta s^2 = g_{\mu\nu}\Delta x^\mu \Delta x^\nu. \tag{1.1}$$

Here, $\{\Delta x^\mu\}$ are the differences between the coordinate values of the two events.

Once the metric tensor is given, the trajectory of a free particle in a gravitational field, i.e. the geodesic line, is determined by the following equation:

$$\frac{d^2x^\lambda}{d\tau^2} = -\Gamma^\lambda_{\mu\nu}\frac{dx^\mu}{d\tau}\frac{dx^\nu}{d\tau}. \tag{1.2}$$

Here, τ is the proper time of the particle, $\Gamma^\lambda_{\mu\nu}$ is the Christoffel symbol, which is defined using $g_{\mu\nu}$ as

$$\Gamma^\lambda_{\mu\nu} = \frac{1}{2}g^{\lambda\alpha}\left(\frac{\partial g_{\alpha\mu}}{\partial x^\nu} + \frac{\partial g_{\alpha\nu}}{\partial x^\mu} - \frac{\partial g_{\mu\nu}}{\partial x^\alpha}\right). \tag{1.3}$$

[1]Here after, Greek indices, such as μ, ν, take $\{0, 1, 2, 3\}$, whereas Roman indices, such as i, j, take $\{1, 2, 3\}$

Multiplying both sides of (1.2) with the mass m of the particle, one obtains the equation of motion for the particle in the gravitational field. The right side of the equation,

$$- m\Gamma^{\lambda}_{\mu\nu}\frac{dx^{\mu}}{d\tau}\frac{dx^{\nu}}{d\tau}, \tag{1.4}$$

represents the gravitational force acting on the particle and $\Gamma^{\lambda}_{\mu\nu}$ represents the magnitude of the gravitational field. Since $\Gamma^{\lambda}_{\mu\nu}$ is derived from the partial derivatives of $g_{\mu\nu}$ in (1.3), $g_{\mu\nu}$ can be regarded as the gravitational potential.

1.1.2 Linearized Einstein's Equation

Gravitational waves are the variations of $g_{\mu\nu}$ which spread out through spacetime as waves. The dynamics of $g_{\mu\nu}$ is governed by the Einstein's equation,

$$R_{\mu\nu} - \frac{1}{2}g_{\mu\nu}R = \frac{8\pi G}{c^4}T_{\mu\nu}. \tag{1.5}$$

Here, $R_{\mu\nu}$ is the Ricci tensor, which is the contraction of Riemann tensor $R^{\lambda}_{\mu\rho\nu}$ about λ, ρ. R is the contraction of the Ricci tensor and called the scalar curvature.

$$R^{\lambda}_{\mu\rho\nu} = \frac{\partial\Gamma^{\lambda}_{\mu\nu}}{\partial x^{\rho}} - \frac{\partial\Gamma^{\lambda}_{\mu\rho}}{\partial x^{\nu}} + \Gamma^{\lambda}_{\alpha\rho}\Gamma^{\alpha}_{\mu\nu} - \Gamma^{\lambda}_{\beta\nu}\Gamma^{\beta}_{\mu\rho} \quad \text{:Riemann tensor} \tag{1.6}$$

$$R_{\mu\nu} = R^{\alpha}_{\mu\alpha\nu} \quad \text{:Ricci tensor} \tag{1.7}$$

$$R = g^{\mu\nu}R_{\mu\nu} \quad \text{: Scalar curvature} \tag{1.8}$$

$T_{\mu\nu}$ is the energy-momentum tensor, G is the Newton's gravitational constant, c is the speed of light.

From now on, gravitational waves are treated as small deviations of $g_{\mu\nu}$ from the Minkowski spacetime $\eta_{\mu\nu}$,

$$g_{\mu\nu} = \eta_{\mu\nu} + h_{\mu\nu}, \tag{1.9}$$

$$\eta_{\mu\nu} = \begin{pmatrix} -1 & 0 & 0 & 0 \\ 0 & 1 & 0 & 0 \\ 0 & 0 & 1 & 0 \\ 0 & 0 & 0 & 1 \end{pmatrix}. \tag{1.10}$$

Here, $h_{\mu\nu}$ is a small perturbation of the spacetime, and it represents the gravitational wave.

By substituting (1.5) with (1.9), and disregarding the terms of $\mathcal{O}\left(h^2_{\mu\nu}\right)$, one obtains a simple equation,

$$\frac{\partial^2\bar{h}_{\mu\nu}}{\partial x^{\alpha}\partial x_{\alpha}} = \Box\bar{h}_{\mu\nu} = -\frac{16\pi G}{c^4}T_{\mu\nu}, \tag{1.11}$$

under the Lorentz gauge,

$$\frac{\partial\bar{h}^{\mu}{}_{\nu}}{\partial x^{\mu}} = 0, \tag{1.12}$$

$$\left(\bar{h}_{\mu\nu} = h_{\mu\nu} - \frac{1}{2}\eta_{\mu\nu}h, \qquad h = h^{\lambda}{}_{\lambda}\right).$$

In a vacuum space, $T_{\mu\nu} = 0$. Therefore,

$$\Box \bar{h}_{\mu\nu} = 0. \tag{1.13}$$

This is a wave equation which states that $h_{\mu\nu}$ propagates through spacetime as a wave.

1.1.3 Monochromatic Plain-Wave Solution

A monochromatic plain-wave solution of (1.13) is given as

$$\bar{h}_{\mu\nu} = A_{\mu\nu} e^{ik_\alpha x^\alpha}. \tag{1.14}$$

Substituting (1.12) and (1.13) with the above expression, the following conditions are derived:

$$A^{\mu\alpha} k_\alpha = 0 \tag{1.15}$$

$$k_\alpha k^\alpha = 0. \tag{1.16}$$

(1.15) states that gravitational waves are transverse waves. From (1.16) one can see that gravitational waves propagate at the speed of light.

Using the transverse-traceless gauge (TT-gauge),

$$A^\alpha_\alpha = 0, \tag{1.17}$$

$$A_{\mu\nu} \delta^\nu_0 = 0, \tag{1.18}$$

the symmetric and traceless form of $A_{\mu\nu}$ is derived as

$$A_{\mu\nu} = \begin{pmatrix} 0 & 0 & 0 & 0 \\ 0 & h_+ & h_\times & 0 \\ 0 & h_\times & -h_+ & 0 \\ 0 & 0 & 0 & 0 \end{pmatrix}. \tag{1.19}$$

Here, h_+ and $h_\times$ correspond to the two polarizations of a gravitational wave.

1.1.4 Interaction with Free Particles

Here, the effect of a gravitational wave to a free particle at rest in the background Minkowski spacetime is considered[2]. Since the particle is at rest,

$$\frac{dx^\mu}{d\tau} = \{1, 0, 0, 0\}. \tag{1.20}$$

[2]Here the geometric unit, in which $c = 1$, is used.

From (1.2), the force exerted by the gravitational wave to the particle is,

$$\begin{aligned}\frac{d^2x^\lambda}{d\tau^2} &= -\Gamma^\lambda_{00} \\ &= \frac{1}{2}\eta^{\lambda\alpha}\left(\frac{\partial \bar{h}_{\alpha 0}}{\partial x^0} + \frac{\partial \bar{h}_{\alpha 0}}{\partial x^0} - \frac{\partial \bar{h}_{00}}{\partial x^\alpha}\right) \\ &= 0. \end{aligned} \tag{1.21}$$

Therefore, no force acts on the particle; TT-gauge is a gauge in which the coordinate system changes so that the effect of the gravitational wave is cancelled.

Although the coordinate values of the particle do not change, the proper distance between two free-particles changes because the metric tensor changes. To see this, consider two particles resting at $(0,0,0,0)$ and $(0,\epsilon,0,0)$ in the background spacetime. The proper distance δl between the particles is

$$\begin{aligned}\delta l = \int \left|ds^2\right|^{1/2} = \int \left|g_{\mu\nu}dx^\mu dx^\nu\right|^{1/2} \\ = \int_0^\epsilon \left|g_{11}\right|^{1/2} dx \simeq \left|g_{11}\right|^{1/2}\epsilon = \left(1 + \frac{1}{2}\bar{h}_{11}\right)\epsilon. \end{aligned} \tag{1.22}$$

Gravitational waves change the proper distance between the two free masses. This is the physical quantity measured by interferometers for the detection of gravitational waves.

1.1.5 Polarizations

A gravitational wave appears as a tidal force to free particles. To see this visually, consider an array of particles circularly arranged (Fig. 1.1).

When a gravitational wave propagating in z-direction (perpendicular to the paper) arrives, the proper distance between the center of the circle and a particle at $(\epsilon\cos\theta, \epsilon\sin\theta)$ changes as

$$\delta l \simeq \left(1 + \frac{1}{2}h_+ \cos 2\theta\right)\epsilon, \tag{1.23}$$

in the case of h_+ polarization.

For $h_\times$ polarization, the change is

$$\delta l \simeq \left(1 + \frac{1}{2}h_\times \sin 2\theta\right)\epsilon. \tag{1.24}$$

The shapes of those modes are shown in Fig. 1.1. The tidal effect of a gravitational wave stretches spacetime in one direction while compressing it in the perpendicular direction. The two polarizations of the gravitational wave, h_+ and $h_\times$ are 45° apart.

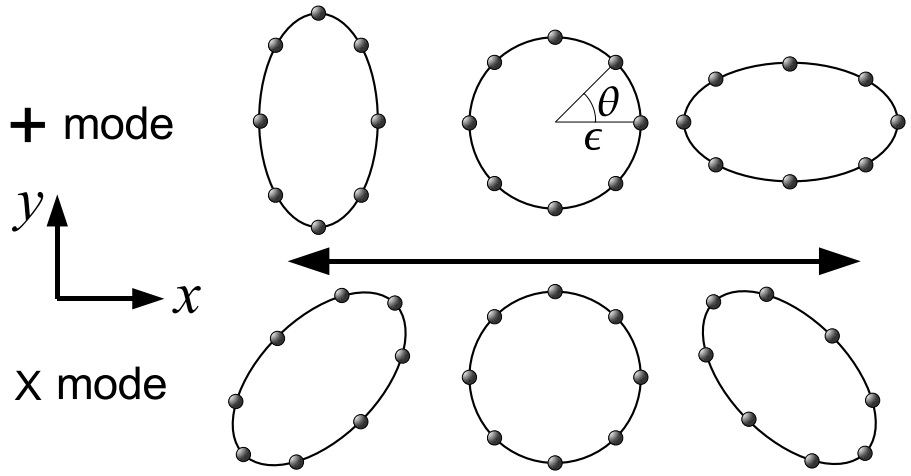

Fig. 1.1: Polarizations of gravitational waves. +mode represents h_+ polarization and ×mode represents $h_\times$ polarization.

1.1.6 Generation of Gravitational Waves

In order to discuss the generation of gravitational waves, (1.11) has to be solved. Using a retarded potential, a solution of (1.11) can be written as

$$\bar{h}_{\mu\nu}\left(x^0,\vec{x}\right)=\frac{4G}{c^4}\int\frac{T_{\mu\nu}\left(x^0-\frac{|\vec{x}-\vec{x}'|}{c},\vec{x}'\right)}{|\vec{x}-\vec{x}'|}d^3x'. \tag{1.25}$$

If the region of $T_{\mu\nu}\neq 0$ is sufficiently small, and the observer is far enough from the source, the above expression can be approximated by,

$$\bar{h}_{ij}\left(x\right)=\frac{2G}{c^4 r}\ddot{Q}_{ij}\left(t'\right), \tag{1.26}$$

where $r\equiv|\vec{x}-\vec{x}'|$ and $t'\equiv t-r/c$. Q_{ij} is the quadrupole momentum of the mass distribution $\rho\left(\vec{x'},t'\right)$,

$$Q_{ij}\left(t'\right)=\int\rho\left(\vec{x'},t'\right)\left(x'_i x'_j-\frac{1}{3}\delta_{ij}x'^i x'^j\right)d^3x'. \tag{1.27}$$

The energy of the gravitational wave radiated by this source in a unit time is,

$$\frac{dE}{dt}=\frac{G}{45c^5}\dddot{Q}^2_{ij}. \tag{1.28}$$

The dipole moment of a gravitational field is always zero if the origin of the coordinate system is chosen to be the center of gravity. Therefore, there is no dipole radiation of gravitational waves in contrast to electro-magnetic waves. In other words, at least a quadrupole moment of a system has to be changed to generate a gravitational wave.

1.2 Sources of Gravitational Waves

Gravitational waves are in principle generated by any motion of masses which involves the change of their quadrupole moment. However, the direct detection of gravitational waves is only possible with an extraordinarily strong wave because the interaction of a gravitational wave with a detector is very weak. The possible sources of detectable gravitational waves are of astronomical origin. In this section, several types of gravitational wave sources are reviewed.

1.2.1 Coalescence of Compact Binary Stars

A binary system of compact stars, such as neutron stars or black holes, loses its orbital energy by radiating gravitational waves as the two stars approach each other. This process is called "inspiral". Eventually, the two stars collide, and in many cases merge to form a black hole. During the last minute of the inspiral, strong gravitational waves are emitted.

The waveform of the gravitational waves from the inspiral can be predicted analytically by Post-Newtonian approximations. This is a great advantage for searching a faint gravitational wave signal in the noisy output of a detector; one can use matched-filtering scheme to pick up the gravitational wave signal efficiently.

From the waveform of the gravitational waves from the coalescence, various information of the binary system can be extracted. For example, the mass and the radius of neutron stars can be determined by analyzing the inspiral and the merger waveforms. Then, the equation of state of neutron stars can be inferred from the relation between the mass and the radius [6].

The event rate of the coalescence of neutron star binaries was estimated from the observations of binary radio pulsars [5]. The estimated coalescence rate is 83^{+209}_{-56} events/Myr/Galaxy. Then the expected detection rate for LCGT[3], the Japanese next generation detector, is $7.9^{+20.4}_{-6.5}$ events/year [19].

Recently, observational evidences of the connection between the coalescence of binary neutron stars and short gamma-ray bursts were reported [7]. Therefore, short gamma-ray bursts may be used as a coincidence partner for the search of binary coalescence.

1.2.2 Burst Sources

Ring-down of a Black Hole's Quasi-Normal Oscillation

Once a black hole is formed by the merger of massive stars, it emits ring-down gravitational waves. The ring-down waveform can be predicted from the black hole perturbation theory. Therefore, matched filtering technique can be used as in the case of the inspiral.

From the waveform of the ring-down gravitational waves, the angular momentum (Kerr parameter) and the mass of the black hole can be determined. Therefore, with gravitational waves, one can directly observe black holes.

[3] See section 1.3.5.

Supernova

The gravitational collapse of the heavy core of a star induced by a supernova may emits gravitational waves if the collapse is asymmetric. It is difficult to predict the exact waveform of the gravitational waves generated by such a collapse. However the recent progress in the field of numerical relativity gives us some estimation on the magnitude of the emitted gravitational waves [8]. Estimated amplitudes of gravitational waves from galactic supernovae are of the order of $h \sim 10^{-21}$ to 10^{-20}. If a supernova occurs in one of the near by galaxies, the gravitational wave from the event may be detectable with LCGT or other advanced detectors.

1.2.3 Continuous Wave Sources

Pulsars

A fast spinning neutron star emits strong gravitational waves if it has asymmetry around its rotation axis or R-mode instability. If a radio pulsar emits strong gravitational waves, there is an advantage for the detection, i.e. the frequency of the gravitational wave is known. Therefore the signal to noise ratio can be improved by integrating it over a long period of time.

The maximum possible amplitude of the gravitational wave emitted by a pulsar can be determined from its spin down rate. Assuming the maximum gravitational waves are really emitted by pulsars, there are several known pulsars that can be detected by LCGT with 1 year of integration [19].

Galactic Binaries

There are a large numbers of binary systems in this galaxy. Those systems emit gravitational waves at very low frequencies and the sum of those gravitational radiations will be a stochastic background gravitational wave of the order of $h \sim 10^{-20}$ below 0.1 mHz. Those waves are undetectable with ground based interferometers. However, space interferometers like LISA may detect the gravitational waves from those binaries. Also gravitational waves from some of nearby binary systems may be resolved to the individual signals.

1.2.4 Cosmological Sources

Various scenarios on the generation of gravitational waves during the inflation or phase transitions of the universe are proposed [9]. The magnitude and the frequency of those gravitational waves varies from theory to theory. For instance, an estimated amplitude of the gravitational waves from the QCD phase transition is $h \sim 10^{-17}$ at 10^{-8} Hz [10].

If gravitational waves from the inflation period are detected, one can obtain information about the universe after only 10^{-22} seconds from its birth, which is impossible with electromagnetic observations.

Since the cosmological gravitational waves are thought to be stochastic, a coincidence analysis between several independent detectors is effective to search for this class of gravitational waves.

1.3 Interferometric Gravitational Wave Detector

In this section, the principles of interferometric gravitational wave detectors are explained.

1.3.1 Michelson Interferometer

The most basic configuration of an interferometric gravitational wave detector is the Michelson interferometer (Fig. 1.2).

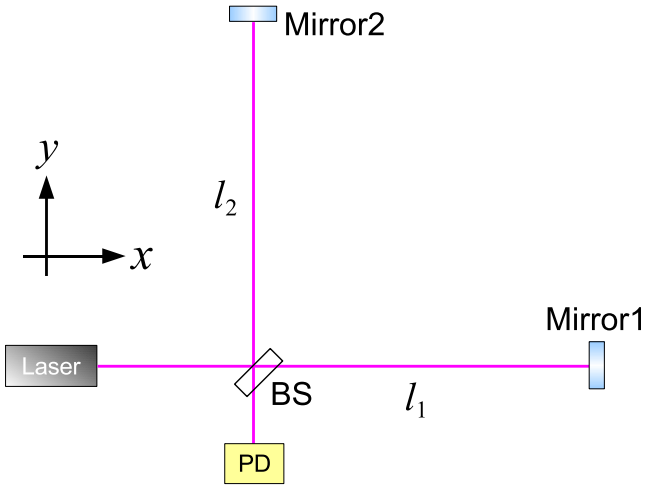

Fig. 1.2: A Michelson Interferometer

Now the electric field of the light emitted from the laser is written as

$$E_{\rm in} = E_0 e^{i\Omega t}. \tag{1.29}$$

This light is split by the beam splitter (BS) into two beams. Each beam is reflected by the end mirrors (M1 and M2), and then recombined at the BS again. Assuming that the phase changes of the light through the round trip from the BS to M1 and M2 are ϕ_1 and ϕ_2, respectively, the recombined light field on the photo detector (PD) is

$$E_{\rm PD} = E_1 e^{i(\Omega t - \phi_1)} - E_2 e^{i(\Omega t - \phi_2)}. \tag{1.30}$$

Here, E_1, E_2 are the amplitudes of the light returning from M1 and M2, respectively. In the ideal case, $E_1 = E_2 = \frac{1}{2}E_0$. However, if the reflectivities of the end mirrors are different, $E_1 \neq E_2$.

The power of the light detected by the PD is

$$\begin{aligned} P_{\mathrm{PD}} = |E_{\mathrm{PD}}|^2 &= E_1^2 + E_2^2 + 2E_1E_2\cos(\phi_1 - \phi_2) \\ &= \frac{P_{\max} + P_{\min}}{2} + \frac{P_{\max} - P_{\min}}{2}\cos(\phi_1 - \phi_2), \end{aligned} \tag{1.31}$$

where,

$$\begin{aligned} P_{\max} &\equiv (E_1 + E_2)^2, \\ P_{\min} &\equiv (E_1 - E_2)^2. \end{aligned} \tag{1.32}$$

The light power on the PD varies as the cosine of the phase difference $\phi_1 - \phi_2$. P_{PD} reaches the maximum $P_{\max}$ when $\phi_1 - \phi_2 = 0$, and the minimum $P_{\min}$ when $\phi_1 - \phi_2 = \pi$. Using $P_{\max}$ and $P_{\min}$, the visibility (or contrast) K of the interferometer is defined as

$$K = \frac{P_{\max} - P_{\min}}{P_{\max} + P_{\min}}. \tag{1.33}$$

K is the index of clarity for the interference pattern on the PD. It is desirable to keep K as high as possible, as poor visibility increases the shot noise of the interferometer.

1.3.2 Response of a Michelson Interferometer to Gravitational Waves

Here, the response of a Michelson interferometer to a gravitational wave is considered. Consider a Cartesian coordinate whose x and y axes are parallel to the arms of the interferometer. Then, suppose a gravitational wave coming from z direction with h_+ polarization.

Under the TT-gauge,

$$ds^2 = -c^2dt^2 + (1+h)\,dx^2 + (1-h)\,dy^2 + dz^2. \tag{1.34}$$

Since light travels on the world line of $ds^2 = 0$, the light traveling on the x axis satisfies

$$\frac{dx}{dt} = \pm\frac{c}{\sqrt{1+h}} \simeq \pm\left(1 - \frac{1}{2}h\right)c, \tag{1.35}$$

where the $+$ sign represents the light traveling in the positive x direction and the $-$ sign corresponds to the negative x direction.

Integrating dx over the round trip path from the BS to M1,

$$\int dx = 2l_1 = c\int_{t-\tau_1}^{t}\left\{1 - \frac{1}{2}h(t')\right\}dt'. \tag{1.36}$$

Therefore,

$$\tau_1 = \frac{2l_1}{c} + \frac{1}{2}\int_{t-\tau_1}^{t} h(t')\,dt' \fallingdotseq \frac{2l_1}{c} + \frac{1}{2}\int_{t-2l_1/c}^{t} h(t')\,dt'. \tag{1.37}$$

Here, τ_1 is the time the light takes for the round trip. In the last expression, τ_1 is approximated by $2l_1/c$ because $h \ll 1$. Therefore, the phase change during the round trip is

$$\phi_1 = \Omega\tau_1 = \frac{2l_1\Omega}{c} + \frac{\Omega}{2}\int_{t-2l_1/c}^{t} h\left(t'\right)dt'. \tag{1.38}$$

Similarly for the light traveling along the y axis,

$$\phi_2 = \frac{2l_2\Omega}{c} - \frac{\Omega}{2}\int_{t-2l_2/c}^{t} h\left(t'\right)dt'. \tag{1.39}$$

Using $l_1 \simeq l_2 \simeq l$, $l_- = l_1 - l_2$,

$$\phi_1 - \phi_2 = \frac{2l_-\Omega}{c} + \delta\phi_{\mathrm{GW}}, \tag{1.40}$$

$$\delta\phi_{\mathrm{GW}} = \Omega\int_{t-2l/c}^{t} h\left(t'\right)dt'. \tag{1.41}$$

(1.41) represents the variation of the phase difference induced by the gravitational wave. This phase change is observed as the change of the interference pattern on the BS. This is the principle of the interferometric gravitational wave detection.

Frequency Response

Now the frequency response of a Michelson interferometer is considered. The Fourier transformation of $h\left(t\right)$ is

$$h\left(t\right) = \int_{-\infty}^{\infty} h\left(\omega\right)e^{i\omega t}dt. \tag{1.42}$$

Then from (1.41),

$$\begin{aligned}\delta\phi_{\mathrm{GW}} &= \Omega\int_{t-2l/c}^{t}\int_{-\infty}^{\infty} h\left(\omega\right)e^{i\omega t'}d\omega dt' \\ &= \int_{-\infty}^{\infty}\frac{2\Omega}{\omega}\sin\left(\frac{l\omega}{c}\right)e^{-il\omega/c}h\left(\omega\right)e^{i\omega t}d\omega \\ &= \int_{-\infty}^{\infty} H_{\mathrm{MI}}\left(\omega\right)h\left(\omega\right)e^{i\omega t}d\omega\end{aligned} \tag{1.43}$$

H_{MI} is the frequency response of the Michelson interferometer to a gravitational wave

$$H_{\mathrm{MI}}\left(\omega\right) = \frac{2\Omega}{\omega}\sin\left(\frac{l\omega}{c}\right)e^{-il\omega/c}. \tag{1.44}$$

$|H_{\mathrm{MI}}|$ is maximum at

$$\frac{l\omega}{c} = \frac{\pi}{2}. \tag{1.45}$$

This means that the interferometer is most sensitive when the phase of the gravitational wave changes by π during the round trip of the light. From this condition, the optimum base line length l for a given frequency can be determined. For a gravitational wave of 1 kHz, the optimum length is about 75 km. An interferometer of this scale is impractical to construct on the Earth. Use of Fabry-Perot cavities in the arms of a Michelson interferometer is a way to circumvent this difficulty. By the Fabry-Perot cavities, the effective length of the arms can be stretched to be way larger than the real length. This configuration is called the Fabry-Perot-Michelson interferometer (Fig. 1.3).

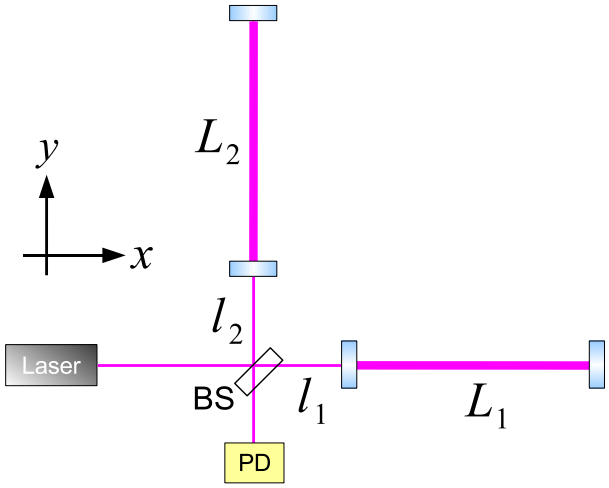

Fig. 1.3: A Fabry-Perot-Michelson interferometer.

1.3.3 Fabry-Perot Interferometer

A Fabry-Perot interferometer or cavity is composed of two mirrors facing each other as shown in Fig. 1.4. The mirrors are partially reflective and the light entered into the cavity is reflected back and forth many times between the mirrors. A fraction of the stored light inside the cavity is reflected back to the incident direction and a fraction is transmitted through the end mirror.

The amplitude of the reflected light is

$$\begin{aligned} E_{\mathrm{r}} &= E_{\mathrm{i}} r_1 + E_{\mathrm{i}} t_1^2 \left(-r_2\right) e^{-2i\delta} + E_{\mathrm{i}} t_1^2 \left(-r_2\right) \left(-r_1\right) \left(-r_2\right) \left(e^{-2i\delta}\right)^2 + \cdots \\ &= E_{\mathrm{i}} r_1 + E_{\mathrm{i}} t_1^2 \left(-r_2\right) e^{-2i\delta} \sum_{n=0}^{\infty} \left(r_1 r_2 e^{-2i\delta}\right)^n \\ &= E_{\mathrm{i}} \left(r_1 - \frac{t_1^2 r_2 e^{-2i\delta}}{1 - r_1 r_2 e^{-2i\delta}} \right), \end{aligned} \tag{1.46}$$

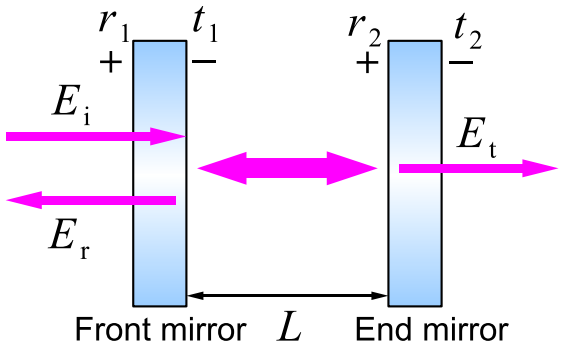

Fig. 1.4: A Fabry-Perot interferometer. Signs on the surfaces of the mirrors represent the sign of the reflectivities.

where $\delta = L\Omega/c$ is the phase change of the light while traveling the distance L. r_1 and r_2 are the amplitudes reflectivity, and t_1, t_2 are the amplitudes transmittance of the front and the end mirrors.

The amplitude of the transmitted light is

$$\begin{aligned} E_{\rm t} &= E_{\rm i} t_1 t_2 e^{-i\delta} + E_{\rm i} t_1 \left(-r_2\right)\left(-r_1\right) t_2 e^{-3i\delta} + E_{\rm i} t_1 \left(-r_2\right)^2 \left(-r_1\right)^2 t_2 e^{-5i\delta} + \cdots \\ &= E_{\rm i} t_1 t_2 e^{-i\delta} \sum_{n=0}^{\infty} \left(r_1 r_2 e^{-2i\delta}\right)^n \\ &= E_{\rm i} \frac{t_1 t_2 e^{i\delta}}{1 - r_1 r_2 e^{-2i\delta}}. \end{aligned} \tag{1.47}$$

Therefore, the reflectivity $r_{\rm cav}$ and the transmittance $t_{\rm cav}$ of the cavity are

$$r_{\rm cav}\left(\delta\right) = r_1 - \frac{t_1^2 r_2 e^{-2i\delta}}{1 - r_1 r_2 e^{-2i\delta}}, \tag{1.48}$$

$$t_{\rm cav}\left(\delta\right) = \frac{t_1 t_2 e^{i\delta}}{1 - r_1 r_2 e^{-2i\delta}}. \tag{1.49}$$

Calculating the power $P_{\rm r}$ and $P_{\rm t}$ of the reflected and transmitted light, one obtains

$$P_{\rm r} = \left|E_{\rm r}\right|^2 = \frac{\left\{\left(t_1^2 + r_1^2\right) r_2 - r_1\right\}^2 + 4 r_1 r_2 \left(r_1^2 + t_1^2\right) \sin^2\delta}{\left(1 - r_1 r_2\right)^2 \left\{1 + F \sin^2\delta\right\}} \left|E_{\rm i}\right|^2, \tag{1.50}$$

$$P_{\rm t} = \left|E_{\rm t}\right|^2 = \frac{t_1^2 t_2^2}{\left(1 - r_1 r_2\right)^2} \frac{1}{1 + F \sin^2\delta} \left|E_{\rm i}\right|^2, \tag{1.51}$$

where

$$F \equiv \frac{4 r_1 r_2}{\left(1 - r_1 r_2\right)^2}. \tag{1.52}$$

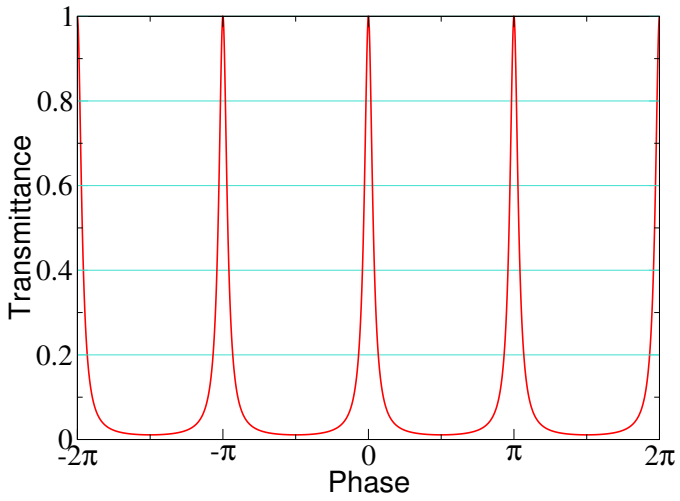

Fig. 1.5: The transmittance of a Fabry-Perot interferometer.

Fig. 1.5 shows the transmittance of the cavity as a function of δ. The transmittance has sharp peaks at $\delta = n\pi$ (n is an integer). The cavity is said to be in resonance when the transmittance is at a maximum.

The resonant frequencies of the laser to the cavity is given by

$$\begin{aligned} \delta &= \frac{L\Omega}{c} = n\pi \\ \therefore \Omega &= \frac{n\pi c}{L}. \end{aligned} \tag{1.53}$$

The difference between neighboring resonant frequencies is called "free spectral range (FSR) " and it is given by

$$f_{\mathrm{FSR}} = \frac{c}{2L}. \tag{1.54}$$

The full-width half-maximum (FWHM) f_{FWHM} of the resonant peaks satisfies the following relation:

$$\frac{1}{1 + F\sin^2\left(\pi L f_{\mathrm{FWHM}}/c\right)} = \frac{1}{2}, \tag{1.55}$$

where $r_1 \simeq r_2$ is assumed. Now, assuming that $f_{\mathrm{FWHM}} \ll f_{\mathrm{FSR}}$,

$$f_{\mathrm{FWHM}} = \frac{c}{\pi\sqrt{F}L} = \frac{(1 - r_1 r_2)\, c}{2\pi L\sqrt{r_1 r_2}}. \tag{1.56}$$

An index of the sharpness of the resonances, called "finesse", is introduced as the ratio between f_{FSR} and f_{FWHM},

$$\mathcal{F} = \frac{f_{\mathrm{FWHM}}}{f_{\mathrm{FSR}}} = \frac{\pi\sqrt{r_1 r_2}}{1 - r_1 r_2}. \tag{1.57}$$

Fig. 1.6 shows the phase change of the reflected light around a resonance as a function of the one-way phase change δ. The phase of the reflected light changes drastically around resonance. This is because small phase changes are accumulated while the light is reflected back and forth in the cavity. Since an interferometric gravitational wave detector makes use of this phase change to enhance the gravitational wave signal, the Fabry-Perot cavities in the arms have to be kept in resonance during the operation.

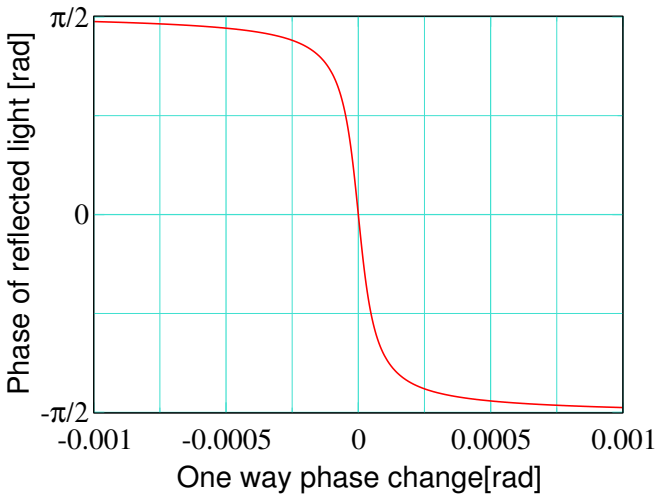

Fig. 1.6: The phase of the reflected light from a Fabry-Perot interferometer. The horizontal axis is δ.

Response of a Fabry-Perot Interferometer to Gravitational Waves

The response of a Fabry-Perot interferometer to a gravitational wave is calculated as follows. Suppose that the interferometer is placed along x axis, and light takes the time τ_n to make n round trips in the cavity. As in the case of a Michelson interferometer, integrating over the path of n round-trips,

$$\int_{t-\tau_n}^{t} \left\{1 - \frac{1}{2}h\left(t'\right)\right\} dt' \simeq \frac{2Ln}{c}. \tag{1.58}$$

Therefore,

$$\tau_n \simeq \frac{2Ln}{c} + \frac{1}{2}\int_{t-2Ln/c}^{t} h\left(t'\right) dt'. \tag{1.59}$$

Substituting it with (1.42), one obtains

$$\tau_n \simeq \frac{2Ln}{c} + \frac{1}{2}\int_{-\infty}^{\infty} h\left(\omega\right) \frac{1 - e^{-2iL\omega n/c}}{i\omega} e^{i\omega t} d\omega. \tag{1.60}$$

From (1.46),

$$E_{\mathrm{r}} = E_{\mathrm{i}} \left(r_1 - t_1^2 r_2 \sum_{n=1}^{\infty} r_1^{n-1} r_2^{n-1} \right) e^{-2i\delta n}. \tag{1.61}$$

Substituting it with $2\delta n = \Omega \tau_n$, and discarding the terms higher than the first order of h,

$$\frac{E_{\mathrm{r}}}{E_{\mathrm{i}}} \simeq r_1 - \frac{t_1^2 r_2 e^{-2i\delta}}{1 - r_1 r_2 e^{-2i\delta}} + \frac{t_1^2 r_2 e^{-2i\delta}}{1 - r_1 r_2 e^{-2i\delta}} \int_{-\infty}^{\infty} \frac{\Omega}{2\omega} h(\omega) \frac{1 - e^{-2iL\omega/c}}{1 - r_1 r_2 e^{-2i\delta} e^{-2iL\omega/c}} e^{i\omega t} d\omega. \tag{1.62}$$

If the cavity is in resonance, where $\delta = n\pi$,

$$\frac{E_{\mathrm{r}}}{E_{\mathrm{i}}} \simeq \frac{r_1 - (r_1^2 + t_1^2) r_2}{1 - r_1 r_2} \left\{ 1 - i \int_{-\infty}^{\infty} H_{\mathrm{FP}}(\omega) h(\omega) e^{i\omega t} d\omega \right\}, \tag{1.63}$$

$$H_{\mathrm{FP}}(\omega) = \frac{\alpha_{\mathrm{c}} \Omega}{\omega} \frac{\sin(\omega L/c)}{1 - r_1 r_2 e^{-2i\omega L/c}} e^{-iL\omega/c}, \tag{1.64}$$

$$\alpha_{\mathrm{c}} = \frac{t_1^2 r_2}{r_1 - (r_1^2 + t_1^2) r_2}. \tag{1.65}$$

H_{FP} is the frequency response of a Fabry-Perot interferometer to gravitational waves. Now the magnitude of H_{FP} is

$$|H_{\mathrm{FP}}| = \frac{\alpha_{\mathrm{c}} \Omega}{\omega (1 - r_1 r_2)} \frac{|\sin(\omega L/c)|}{\sqrt{1 + F \sin^2(\omega L/c)}}. \tag{1.66}$$

In the case of low-frequency gravitational waves, $\omega L/c \ll 1$,

$$\begin{aligned} |H_{\mathrm{FP}}| &\simeq \frac{\alpha_{\mathrm{c}} \Omega}{\omega (1 - r_1 r_2)} \frac{\omega L}{c \sqrt{1 + \left(\sqrt{F} L \omega / c \right)^2}} \\ &= \frac{\alpha_{\mathrm{c}} \Omega L}{c (1 - r_1 r_2)} \frac{1}{\sqrt{1 + (\tau\omega)^2}}, \end{aligned} \tag{1.67}$$

$$\tau = \frac{\sqrt{F} L}{c} = \frac{2L}{\pi c} \mathcal{F}. \tag{1.68}$$

Therefore the frequency response of a Fabry-Perot interferometer is a first order low-pass filter with the cut-off frequency $1/\tau$, called the "cavity pole". τ corresponds to the mean time a photon stays in the cavity. From (1.68), $\mathcal{F}$ can be regarded as the mean number of times a photon makes round-trips.

1.3.4 Noise Sources

The sensitivity of an interferometer is limited by various noises. Here fundamental noises of an interferometer are briefly explained.

Shot Noise

The quantum fluctuation of number of photons in a light beam is called shot noise. If the photo current on a photo detector is $I_{\rm P}$, the power spectrum of the shot noise is given by

$$\left\langle {i_{\rm N}}^2 \right\rangle = 2eI_{\rm P}, \tag{1.69}$$

$$\therefore \quad i_{\rm N} = \sqrt{2eI_{\rm P}}, \tag{1.70}$$

where e is the elementary charge. Now consider the case of a Michelson interferometer. By writing the phase difference on the beam splitter as

$$\phi_1 - \phi_2 = \Phi_0 + \delta\phi, \tag{1.71}$$

the variation of the photo current on the photo detector is, from (1.31),

$$\delta I_{\rm P} = -\frac{I_{\rm max} - I_{\rm min}}{2} \sin\left(\Phi_0\right) \delta\phi. \tag{1.72}$$

Here $I_{\rm max}$ and $I_{\rm min}$ are the photo currents corresponding to $P_{\rm max}$ and $P_{\rm min}$. By equating it with the shot noise (1.70), the minimum detectable phase $\delta\phi_{\rm min}$ is obtained as

$$\delta\phi_{\rm min} = \frac{2\sqrt{2eI_{\rm dc}}}{I_{\rm max} - I_{\rm min}} \frac{1}{\sin\Phi_0}, \tag{1.73}$$

where

$$I_{\rm dc} = \frac{I_{\rm max} + I_{\rm min}}{2} + \frac{I_{\rm max} - I_{\rm min}}{2} \cos\Phi_0. \tag{1.74}$$

In the case of the ideal visibility, where $I_{\rm min} = 0$,

$$\delta\phi_{\rm min} = \sqrt{\frac{2e}{I_{\rm max}}} \frac{1}{\sin\left(\Phi_0/2\right)}. \tag{1.75}$$

$\delta\phi_{\rm min}$ is minimum when $\Phi_0 = \pi$. In this case, $I_{\rm dc}$ is also minimum; the beam splitter is at a dark fringe. In order to minimize the shot noise, the interferometer's detection port is always kept in a dark fringe. As is seen from (1.75), the shot noise is inversely proportional to the square-root of $I_{\rm max}$. It is expressed by the quantum efficiency of the photo detector η and the incident laser power P as

$$I_{\rm max} = e\frac{\eta P}{\hbar\Omega}, \tag{1.76}$$

where $\hbar$ is the Plank constant divided by 2π. Therefore, the shot noise at a dark fringe is,

$$\delta\phi_{\rm min} = \sqrt{\frac{2\hbar\Omega}{\eta P}}. \tag{1.77}$$

Consequently, the shot noise can be reduced by increasing the power of the laser. In order to increase the effective power of the laser, a technique called "power recycling" [11] is used in large scale interferometers; an additional mirror is placed between the laser and the beam splitter to reflect the light going back from the beam splitter and send it again to the interferometer.

Radiation Pressure Noise

When a photon is reflected by a mirror, a back action force is exerted to the mirror by the momentum transfer from the photon to the mirror. This back action force fluctuates as the number of photons fluctuates because of the quantum nature of light. This noise is called "radiation pressure" noise.

The spectral density of the radiation pressure noise for a Fabry-Perot-Michelson interferometer is [18]

$$h_{\mathrm{rp}}(\omega) = \frac{4\mathcal{F}}{Lm\omega^2\pi}\sqrt{\frac{16\pi\hbar P_0}{c\lambda}}\frac{1}{\sqrt{1+(\omega/\omega_{\mathrm{c}})^2}}, \tag{1.78}$$

$$\omega_{\mathrm{c}} = \frac{\pi c}{2L\mathcal{F}}. \tag{1.79}$$

Here, $\mathcal{F}$ is the finesse of the arm cavities, L is the length of the arms, m is the mass of the mirrors, λ is the wavelength of the laser, P_0 is the laser power, ω_{c} is the angular cut-off frequency of the arm cavities.

The radiation pressure noise is proportional to the square-root of the laser power, $h_{\mathrm{rp}} \propto \sqrt{P_0}$. Since the shot noise is inversely proportional to $\sqrt{P_0}$, there is a trade-off between the shot noise and the radiation pressure noise as to the laser power. Resulting from the trade-off, there is a limit on the sensitivity of an interferometer called the standard quantum limit (SQL) [12],

$$h_{\mathrm{SQL}} = \frac{1}{L\omega}\sqrt{\frac{8\hbar}{m}}. \tag{1.80}$$

This limit corresponds to the quantum mechanical limit of the measurement from the uncertainty principle. Currently various methods to beat this limit are proposed [13].

Thermal Noise

The mirrors and the suspension systems of an interferometer fluctuate thermally because they are at a finite temperature. Those thermal fluctuations induce unwanted variations of the arm lengths of the interferometer, called thermal noise.

The amount of thermal fluctuation is related to the loss of a system by the fluctuation-dissipation theorem (FDT) [14]. It states that the thermal fluctuation force is proportional to the real part of the mechanical impedance of a system. An intuitive interpretation of the FDT can be made as follows. When a system loses its energy by dissipation, the dissipated energy is absorbed by the heat bath around the system. Therefore, a large loss corresponds to a broad connection between the system and the heat bath. Then energy fluctuations can be easily introduced to the system from the heat bath through the broad connection. Thus, the thermal fluctuation of a system is large when the loss of the system is large.

The thermal noise of mirrors or suspension systems can be analyzed by expanding a system into a sum of harmonic oscillators. From the FDT, the power spectrum of the

thermal noise of a harmonic oscillator is,

$$\left\langle x\left(\omega\right)^2\right\rangle = \frac{4k_{\mathrm{B}}T}{mQ}\frac{\omega_0}{\left(\omega^2-\omega_0^2\right)^2+\omega_0^2\omega^2/Q^2}, \tag{1.81}$$

where k_{B} is the Boltzmann constant, T is the temperature, m is the mass, ω_0 is the angular resonant frequency of the system. Q is the quality factor of the system and it is connected to the loss angle ϕ of the system by

$$\phi(\omega) = \frac{\omega}{\omega_0 Q} \quad : \text{Viscous damping model,} \tag{1.82}$$

$$\phi = \frac{1}{Q} \quad : \text{Structure damping model.} \tag{1.83}$$

The loss angle ϕ is related to the argument of the mechanical admittance Y of the system by

$$\arg\left(Y\left(\omega\right)\right) = \arctan\left(\phi\left(\omega\right)\right). \tag{1.84}$$

From this, it is obvious that the thermal noise of a system can be reduced either by cooling down the system or increasing the quality factor of the system.

As to the quality factor, currently there are intense efforts to find low-loss materials and various designs of low-loss suspension systems are proposed. The LCGT project is planning to construct cryogenic interferometers to reduce the thermal noise using low temperatures.

Seismic Noise

Concerning an interferometer constructed on Earth, one cannot escape from the seismic vibration. If this vibration is transmitted to the mirrors of an interferometer, the induced motion on the mirrors is indistinguishable from gravitational wave signals. This is called the seismic noise.

It is empirically known that the shape of the seismic spectrum is roughly proportional to $1/f^2$ and its magnitude varies by one or two orders of magnitude from location to location. Therefore, it is essential to find a quiet site for the construction of an interferometer. A seismic vibration model of the Kamioka site, where LCGT interferometers will be built, is,

$$x_{\mathrm{seis}} = \begin{cases} \left(\frac{10^{-8}}{f^2}\right)\mathrm{m}/\sqrt{\mathrm{Hz}} & f \geq 0.1\mathrm{Hz} \\ 10^{-6}\mathrm{m}/\sqrt{\mathrm{Hz}} & f < 0.1\mathrm{Hz} \end{cases}. \tag{1.85}$$

The seismic noise causes mainly two problems to an interferometer. First, at low frequencies the large seismic vibration makes the interferometer unstable. Second, in the observation frequencies of the interferometer, the seismic noise may limit the sensitivity of the interferometer if it is poorly attenuated.

In order to reduce the seismic noise, various vibration attenuation mechanisms are installed in the mirror suspensions of an interferometer. The attenuation of the seismic noise is the main issue of this thesis. General discussions on the vibration isolation systems of an interferometer are given in section 2.1.

Laser Noises

Since a laser interferometric gravitational wave detector measures the length between the mirrors using the wavelength of the laser as a reference, the noises of the laser contaminates its sensitivity.

The fluctuation of the laser frequency is in principle cancelled at the beam splitter when the response of the two arms are identical. In reality, the frequency noise is not completely cancelled because of a small asymmetry of the arms. Therefore, the stabilization of the laser frequency is necessary. Usually, the frequency is pre-stabilized by mode cleaners (external stable cavities). Then ultimately stabilized using the common mode signal of the arm lengths.

The intensity fluctuation of the laser also introduces a noise into the output of the interferometer. As in the case of the frequency noise, the intensity noise is cancelled at the beam splitter in principle. However, the intensity noise appears to the output of the interferometer coupled with the asymmetry of the arms and the residual motions of the mirrors. Therefore, the stabilization of the laser intensity is also important to achieve good sensitivity.

Residual Gas Noise

The random motions of air molecules cause fluctuation of the index of refraction in the optical paths of an interferometer. This fluctuation produces the fluctuation of the effective lengths of the arms.

In order to reduce the effect of air fluctuation, interferometers are operated in an ultrahigh vacuum. The required vacuum for LCGT is 2×10^{-9} Torr [19].

Control System Noise

During the operation of an interferometer, the optical components (the mirrors and the beam splitter) of the interferometer have to be controlled to keep the Fabry-Perot arms in resonance and the detection port at a dark fringe. The noise of the electric circuits for the control system may contaminate the sensitivity of the interferometer; this is called control system noise.

The simplest way to reduce the control noise is to use low-noise circuits. However, the required noise level for the electric circuits is close to or beyond the noise level achievable with the state-of-the-art electric components.

Another way to avoid the control noise problem is to reduce the coupling between the electric noise and the output of the interferometer by using weak actuators for the control. In order to use weak actuators, the residual motions of the optical components have to be enough small so that the motions can be suppressed with the weak actuators. The reduction of the residual motions can be achieved by the introduction of the suspension point interferometer as discussed in section 2.5.3.

1.3.5 Current Projects

Here, the large scale interferometric gravitational wave detectors currently operated or planned are briefly reviewed.

TAMA

TAMA is an interferometric gravitational wave detector constructed in Mitaka campus of National Astronomy Observatory Japan (NAOJ) [15]. It is a recycled Fabry-Perot Michelson interferometer with the arm length of 300 m.

TAMA started the observational operation in 1999. It was the first scientific observation by a large scale interferometric gravitational wave detector in the world. The current sensitivity is $2 \times 10^{-21}\, 1/\sqrt{\mathrm{Hz}}$ at 1 kHz.

LCGT

LCGT (Large scale Cryogenic Gravitational wave Telescope) is the next generation interferometer currently in the design process by the Japanese gravitational wave group [17, 19]. It features the use of cryogenic mirrors to reduce the thermal noise. The optical configuration of LCGT is a RSE (Resonant Sideband Extraction) [16] interferometer with the arm length of 3 km. The current plan is to construct two interferometers in a vacuum system. LCGT interferometers will be constructed underground in Kamioka mine, Gifu prefecture, Japan.

LCGT interferometers will be equipped with suspension point interferometers to attenuate the vibrations introduced from heat link wires, which are necessary to cool down the mirrors.

The design sensitivity of LCGT is $4 \times 10^{-24}\, 1/\sqrt{\mathrm{Hz}}$ around 100 Hz.

LIGO

LIGO (Laser Interferometer Gravitational wave Observatory) is the American project for the interferometric detection of gravitational waves [20]. Three interferometers have been constructed, two in Hanford, Washington, and one in Livingston, Louisiana. The arm length of the interferometers are 4 km for one of the Hanford interferometers and the Livingston interferometer. The other Hanford interferometer has 2 km arms and it shares the same vacuum tube with the 4 km one.

LIGO started the scientific observations in 2002. The current sensitivity is $4 \times 10^{-23}\, 1/\sqrt{\mathrm{Hz}}$ around 100 Hz.

LIGO project plans to upgrade the interferometers to include advanced technologies such as the RSE configuration and the DC readout scheme. The upgraded interferometer will be called LIGO II. The target sensitivity of LIGO II is similar to that of LCGT.

GEO

GEO is the joint effort of British and German groups to construct an interferometric gravitational wave detector. A 600 m interferometer, GEO600, has been built near Hannover, Germany [21]. Unlike the other large scale interferometers, GEO600 is a dual-recycled delay-line Michelson interferometer. With this configuration, the shot noise shape of the interferometer can be changed and optimized to a specific target.

The typical sensitivity of GEO600 at present (December 2005) is $4 \times 10^{-22}\,1/\sqrt{\mathrm{Hz}}$ around 600 Hz.

VIRGO

VIRGO is a 3 km long interferometric gravitational wave detector built by the collaboration of French and Italian research teams [22]. It is located near Pisa, Italy. VIRGO features ultra low frequency vibration isolation systems for the mirrors, called Super Attenuators [23] and the designed sensitivity at 10 Hz is $3 \times 10^{-21}\,1/\sqrt{\mathrm{Hz}}$.

The current sensitivity (September 2005) is about $5 \times 10^{-22}\,1/\sqrt{\mathrm{Hz}}$ around 300 Hz.

LISA

LISA (Laser Interferometer Space Antenna) [24] is not a ground based interferometer, but it is an interferometer formed by spacecrafts. LISA is a joint project of NASA and ESA. Three spacecrafts are arranged in an equilateral triangle of 5 million kilometers. The distances between the spacecrafts are monitored by laser interferometry.

The targets of LISA are very low frequency gravitational waves below 1 mHz. This class of gravitational wave sources include galactic binary stars, collisions of super massive black holes, cosmological back ground gravitational radiations, and so on.

LISA spacecrafts are planned to be launched in 2015.

Chapter 2

Suspension Point Interferometer

Suspension point interferometer (SPI) is an active vibration isolation scheme for interferometric gravitational wave detectors. It was proposed by Drever about 20 years ago [3]. The SPI makes use of an auxiliary interferometer to monitor the seismic vibration transmitted through the suspension wires. The seismic vibration is actively suppressed by an appropriate feedback control using the signal from the auxiliary interferometer. The name "suspension point interferometer" is used because the auxiliary interferometer is usually placed at the suspension points of the mirrors of the main interferometer.

Only a few experimental studies have been done on this technique since it was proposed [4, 26, 27]. This is mainly because (1) the SPI requires additional cost for making an auxiliary interferometer, and (2) the requirements for the vibration attenuation of the first generation detectors [15, 20, 21, 22] are not so severe that the SPI is needed. However in the next generation interferometers like LCGT [19], the SPI is considered to be a possible solution to expand the observation band toward lower frequencies and to improve the stability of the interferometers. The stability improvement will also reduce requirements for various technical noises such as coil driver noise.

In this chapter, the common configuration of suspension systems for interferometric gravitational wave detectors is described first. Then a general discussion on active vibration isolation system is given. Next the basic configuration and working principle of the SPI followed by simple model based calculations of its performance are explained. Finally, the advantages of the SPI and its applications to large scale detectors are discussed in section 2.5.

2.1 Suspension System of Interferometric Gravitational Wave Detectors

There are two major requirements for the mirror support mechanism of an interferometer. Firstly, a mirror should be supported so softly that one can regard it as a free masses in the observation frequency band. Secondly, the mirror should be well isolated from external

disturbances, especially from seismic vibrations. In order to meet those requirements, pendulum suspension systems are widely used in interferometric gravitational wave detectors.

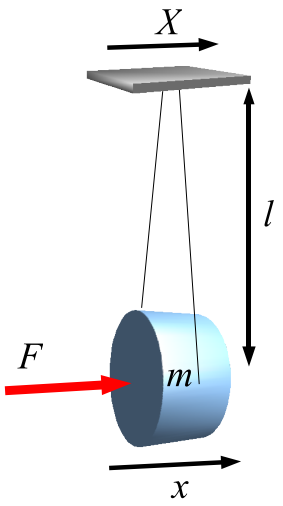

Fig. 2.1: A simple pendulum

2.1.1 Simple Pendulum Suspension

The equation of motion for a suspended mirror with mass m and the wire length l (Fig. 2.1) is

$$m\ddot{x}(t) = F(t) - mg\frac{(x(t) - X(t))}{l}. \tag{2.1}$$

Here g is the Earth's gravitational acceleration, F is an external force exerted on the mirror, x and X are the horizontal displacement of the mirror and that of its suspension point, respectively. Since the discussion here is on the detection of gravitational "waves", which have non-zero frequencies, DC displacement is not taken into account; x and X are deviations from their mean or equilibrium positions. Performing Fourier-transformations on both sides of (2.1), one obtains

$$-\omega^2 m\tilde{x}(\omega) = \tilde{F}(\omega) - mg\frac{\left(\tilde{x}(\omega) - \tilde{X}(\omega)\right)}{l}, \tag{2.2}$$

where variables with "˜" are Fourier transformations of corresponding variables in (2.2). From this equation the following relation is deduced,

$$\tilde{x}(\omega) = \frac{1}{\omega_0^2 - \omega^2}\left(\tilde{X}(\omega) + \frac{\tilde{F}(\omega)}{m}\right), \qquad \omega_0 = \sqrt{\frac{g}{l}}. \tag{2.3}$$

Now the transfer function from the applied force $\tilde{F}(\omega)$ to the resultant motion $\tilde{x}(\omega)$ is,

$$\frac{\tilde{x}(\omega)}{\tilde{F}(\omega)} = \frac{1}{m(\omega_0^2 - \omega^2)}. \tag{2.4}$$

At frequencies well above the resonant frequency ω_0 of the pendulum,

$$\frac{\tilde{x}(\omega)}{\tilde{F}(\omega)} \simeq \frac{1}{-m\omega^2}. \tag{2.5}$$

For the purposes of comparison, consider the one dimensional equation of motion for a free mass with mass m under an external force F,

$$m\ddot{x}(t) = F(t). \tag{2.6}$$

Similar calculations as above lead to

$$\frac{\tilde{x}(\omega)}{\tilde{F}(\omega)} = \frac{1}{-m\omega^2}. \tag{2.7}$$

By comparing (2.5) and (2.7), one can see that a suspended mirror responds to an external force just like a free mass at frequencies above ω_0.

Another transfer function derived from (2.3) is

$$\frac{\tilde{x}(\omega)}{\tilde{X}(\omega)} = \frac{\omega_0^2}{\omega_0^2 - \omega^2}. \tag{2.8}$$

This transfer function approaches ω_0^2/ω^2 at frequencies above ω_0 and becomes smaller as the frequency goes up. This means that the motion of the suspension point (X) is attenuated by the pendulum at frequencies above its resonance and the magnitude of the attenuation increases as frequency goes up. Besides, at a fixed frequency, greater attenuation is achieved with a smaller ω_0.

The above calculations show that a pendulum suspension offers both free mass like behavior and vibration isolation to a mirror. In large scale interferometers, multi-stage pendulums are often used because vibration attenuation provided by a single pendulum is usually not sufficient to satisfy the requirements (Fig. 2.2).

2.1.2 Other Degrees of Freedom

In the above consideration, we confined ourselves to a horizontal degree of freedom parallel to the laser beam, which is called "in-line" direction here after. In reality, a mirror has 5 other degrees of freedom for its motion[1]. Since an interferometer is designed to be sensitive only to the in-line motion, the other degrees of freedom are relatively less important. However, there are always some couplings from motions in those non in-line degrees of

[1]The naming conventions of the mirror's degrees of freedom and their corresponding notations are shown in Fig. 2.3.

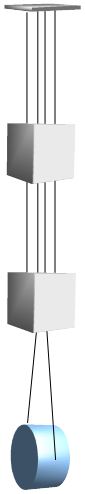

Fig. 2.2: A multi-stage pendulum suspension

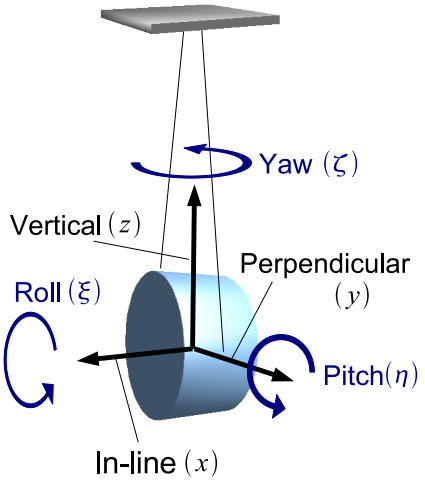

Fig. 2.3: Mirror's degrees of freedom

freedom to the output of the interferometer. There are two classes of such couplings. The first class is the conversion from the motion of a suspension stage in a certain direction to the motion of the next stage in other degree of freedom. For example a fraction of the pitch motion of the suspension stage above the mirror is converted to the in-line motion of the mirror if the wire clamp points on the mirror are not at the same level as the mirror's center of gravity (see Fig. 2.11). The second class of the couplings is the interferometer's sensing error. In this case, non in-line motions of a mirror are erroneously sensed by the interferometer through the mis-alignment of the mirrors to the incident laser beam. To avoid the contamination to the interferometer's sensitivity by those couplings, the vibration isolation of all the degrees of freedom is needed.

The discussion of the vibration isolation for the in-line motion given above is generally applicable to mechanical systems with a linear restoring force, which is always the case when treating tiny deviations from equilibrium points with linear approximation; relations similar to (2.8) hold true for other degrees of freedom. Therefore the vibration attenuation performance of a mechanical system in a certain degree of freedom can be appraised by how low its resonant frequency in that degree of freedom is.

Now each degree of freedom shown in Fig. 2.3 is examined. In the perpendicular direction, the pendulum has the same resonant frequency as the in-line direction. The yaw and pitch resonant frequencies depend on the locations of the wire clamp points at the mirror and the suspension point. Usually it is not difficult to make those resonant frequencies equal to or lower than the in-line one. The key to achieve low resonant frequencies is to concentrate the clamp points to the point which coincides with the rotational axes of the mirror. In the case of yaw, the suspension wires should converge at the suspension point. For pitch, the wire clamp points at the mirror should be as close as possible to the mirror's

center of gravity in the z-x plane.

Since mirrors are usually made axisymmetric around x axis, the roll motion does not cause a serious coupling to the in-line motion. Therefore the requirement for the vibration isolation in roll degree of freedom is usually not severe. If needed, the coupling from the tilt of the suspension point to the roll motion, which is the normal path to induce the roll motion, can be dramatically reduced by making the suspension wires converge to one point at the suspension point.

Vertical motion is usually the most tough nut to crack among all the degrees of freedom. To see this, suppose a linear spring with a spring constant k. It is used to support a mirror with mass m. Then the vertical resonant frequency ω_{0v} is,

$$\omega_{0v} = \sqrt{\frac{k}{m}}. \tag{2.9}$$

If the spring is stretched by a certain length l from its natural length,

$$l = \frac{mg}{k}. \tag{2.10}$$

Combining this with (2.9),

$$l = \frac{g}{\omega_{0v}^2}. \tag{2.11}$$

Therefore, once the resonant frequency ω_{0v} is given, l is determined automatically. For example, if a vertical resonant frequency $\omega_{0v} = 2\pi\,[\mathrm{rad/sec}] = 1\,\mathrm{Hz}$ is needed, l should be about 25 cm. To stretch a linear spring by this amount without making it plastic, the natural length of the spring should be several times longer than l. Hence the total length would be of the order of 1 m. This is not impossible but impractical size for one stage of vibration isolation stacks since several layers of similar stages are used in a whole suspension system. One solution is to use non-linear springs such as a Monolithic Geometric Anti-Spring (MGAS) filter, which is described in detail in section 3.2.3. Using an MGAS filter, one can realize a very low vertical resonant frequency with a moderate size spring; for example in the experiment described in chapter 3, ω_{0v}=0.2 Hz was achieved using an MGAS filter with the diameter of 50 cm and the height of 15 cm.

2.2 Active Vibration Isolation

The suspension system analyzed in the previous section is a passive vibration isolation device; no external energy supply is needed to operate it. Active vibration isolation systems, on the other hand, make use of artificial external forces to nullify the vibration.

In Fig. 2.4, a conceptual block diagram of an active vibration isolation system is shown. First, the motion of the mirror is measured by a sensor. To do so we need a reference relative to which the motion of the mirror is measured. Then, the sensed motion is negatively fed back to the mirror using an actuator through an appropriate feedback filter. The filter is

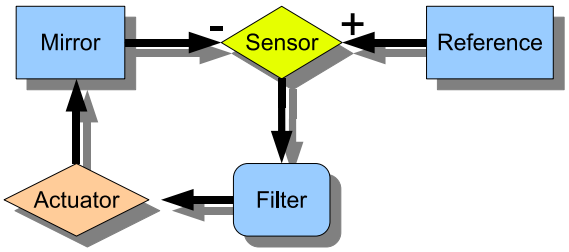

Fig. 2.4: A conceptual block diagram of an active vibration system.

designed to meet the stability conditions for the feedback loop. In this way, the mirror is forced to follow the motion of the reference within the bandwidth of the control loop.

Choice of the reference is very important in designing an active vibration isolation system. When it comes to gravitational wave detectors, the mirrors should be at rest in the interferometer's local inertial frame[2]. Therefore, it is a natural choice to use this local inertial frame as a reference.

2.2.1 Accelerometer

Accelerometer can be considered as a sensor to monitor the motion of a mirror with respect to the local inertial frame. Therefore accelerometers are widely used in various active vibration isolation systems.

Fig. 2.5 shows the basic structure of a proof-mass type accelerometer with feedback control. It is actually quite similar to that of an active vibrations isolation system. The proof mass is softly supported from the housing of the accelerometer; in the example of Fig. 2.5, it is suspended as a pendulum. Owing to the soft support, the proof mass is isolated from the motion X of the housing at high frequencies. Therefore, the proof mass can be used as an inertial reference. The relative displacement between the proof mass and the housing of the accelerometer is measured by a certain sensor, such as a capacitive sensor or a laser interferometer. Usually the measured displacement is negatively fed back to the proof mass by an actuator, in order to improve the dynamic range and the linearity of the sensor.

Now the working principle of the accelerometer is explained using the block diagram in Fig. 2.6. The transfer function from the motion of the housing X to the motion of the proof mass x is denoted by $H(\omega)$. $F(\omega)$ is the transfer function of the feedback filter. $A(\omega)$ is the transfer function from the feedback voltage $V_{\rm fb}$ to the displacement of the proof mass.

Starting from

$$x = HX - AF(x - X), \tag{2.12}$$

[2]Among infinite numbers of local inertial frames with various velocities, the interferometer's rest frame is chosen.

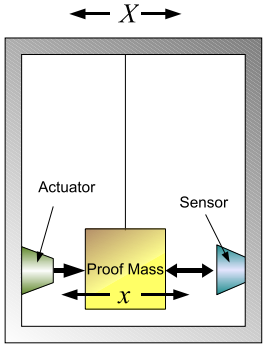

Fig. 2.5: A schematic structure of a proof-mass type accelerometer.

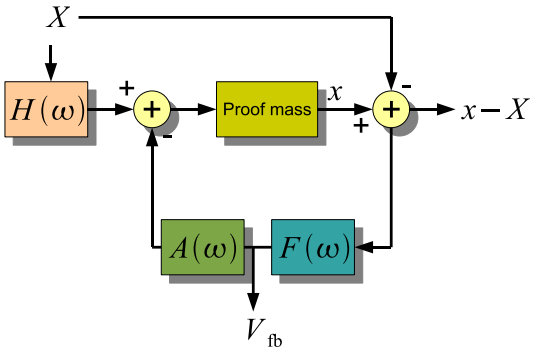

Fig. 2.6: The block diagram of the accelerometer illustrated in the left figure.

one obtains,

$$x = \frac{H + AF}{1 + AF} X. \tag{2.13}$$

Then,

$$V_{\rm fb} = F(x - X) = \left(\frac{H - 1}{A + 1/F} \right) X \simeq -\frac{1 - H}{A} X. \tag{2.14}$$

At frequencies above the resonance of the $H(\omega)$, $H \ll 1$ and $A \propto 1/\omega^2$ can be usually assumed. Therefore,

$$V_{\rm fb} \propto \omega^2 X. \tag{2.15}$$

$\omega^2 X$ is the Fourier transformation of the acceleration d^2X/dt^2. Therefore, the acceleration is obtained from the feedback signal $V_{\rm fb}$.

Although accelerometers are widely and successfully used in various applications, there is a fundamental week point; the sensitivity of an accelerometer becomes poor at low frequencies. This is because in frequency domain, $a(\omega) = \omega^2 x(\omega)$, where $a(\omega)$ is the acceleration spectrum and $x(\omega)$ is the displacement spectrum. This means that even for a constant displacement spectrum $x(\omega)$, the acceleration $a(\omega)$ becomes quadratically smaller as frequency goes down. Therefore the signal-to-noise ratio decreases at low frequencies. As far as one measures "acceleration", it is inevitable that the sensitivity to the corresponding displacement becomes also poor at low frequencies. In the SPI scheme, the measured quantity is not "acceleration"; instead, "length" is measured directly. Therefore the SPI is immune from this low-frequency difficulty. Details of the configuration and the principle of the SPI is described in the following section.

2.3 Working Principle of the SPI

Fig. 2.7 shows a basic configuration of a Fabry-Perot-Michelson interferometer equipped with a suspension point interferometer. The lower interferometer, which is composed of

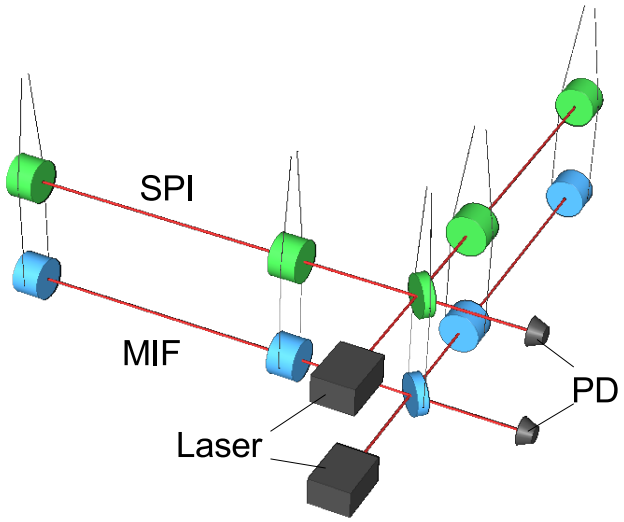

Fig. 2.7: A conceptual configuration of suspension-point interferometers installed to a Fabry-Perot Michelson interferometer

blue optical components in the figure, is called "main interferometer (MIF)" and used to detect gravitational waves. The upper interferometer (colored green in the figure) is called "suspension point interferometer (SPI)". The vibration transmitted through the wires is monitored by the SPI. Then forces to nullify the vibration are applied to the mirrors of the SPI. Through this, the mirrors of the MIF are isolated from external vibrations.

When this system is regarded as an active vibration isolation system, the SPI corresponds to the sensor in Fig. 2.4. In this scheme the reference is not the local inertial frame; instead, the SPI measures the same degree of freedom as the MIF, i.e. the distance between the front and end mirrors. Each mirror serves as a reference for its companion mirror. Since the sensor is a position sensor, the SPI scheme does not suffer from the poor low frequency performance of accelerometers. Actuators on the mirrors of the SPI correspond to the actuator in Fig. 2.4. The feedback filter to maintain the SPI in resonance also works as the filter for the active vibration isolation system.

In Fig. 2.7, the SPI is illustrated as a recombined Fabry-Perot-Michelson interferometer. This configuration is necessary if the stabilization of the Michelson part (differential motion of the front mirrors of the arm cavities) is needed. However, in most applications, this configuration is not necessary because, compared to the Fabry-Perot arms, the contribution from the motions in the Michelson part to the interferometer's sensitivity is negligibly small. Therefore, the recombination of the reflected light from the arms is not necessarily required for the SPI; hence, only the Fabry-Perot part of the SPI is considered in this thesis.

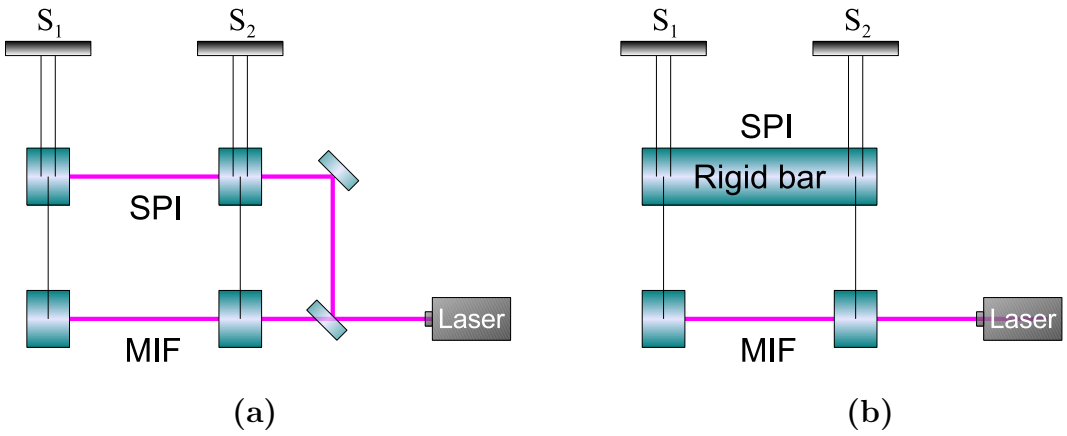

Fig. 2.8: A Fabry-Perot arm with an SPI.

2.3.1 Rigid Bar Picture

Fig. 2.8(a) shows one arm of a Fabry-Perot-Michelson interferometer with an SPI. When the SPI is locked to the laser by the Pound-Drever-Hall (PDH) scheme [25][3], the distance between the mirrors of the SPI is fixed within the accuracy of the control servo. Therefore those mirrors behave together as a virtual rigid bar. Fig. 2.8(b) illustrates this situation schematically. This rigid bar picture is helpful to analyze and understand the behavior of the SPI.

Suppose the suspension points, S_1, S_2, of the mirrors move differentially. In this case the motion is transmitted to the SPI as a force to change its length. Since the SPI behaves as a rigid bar, the force does not actually change its length. Therefore, the differential motion is well suppressed by the SPI. If the common motion of S_1 and S_2 is excited, the transmitted vibrations from each point exert the same force to the virtual rigid bar. Accordingly, the virtual rigid bar is moved by this common force. If the pendulums suspending the mirrors of the MIF are identical, the motion of the rigid bar is transmitted to the MIF as a common motion of its mirrors. Since the MIF is measuring the differential motion of its mirrors, the transmitted common motion produces no noise in the output of the MIF. However in reality, the pendulums are not perfectly identical. This asymmetry converts some portion of the rigid bar's motion into the differential motion of the MIF's mirrors. This conversion sets a limit on the vibration isolation performance of the SPI. Quantitative analysis of this effect is given in section 2.4.

2.3.2 Response to Gravitational Waves

When gravitational waves arrive, the SPI is of course affected by them. Since the SPI is just like an ordinary interferometric gravitational wave detector, its response to gravitational waves is the same as an ordinary interferometer.

[3]See appendix B

Here the discussion is confined to Fabry-Perot interferometers as shown in Fig. 2.8(a). When a gravitational wave exerts a force to expand the length of the SPI, the servo system tries to push the mirrors back to keep the length. Therefore, the effect of the gravitational wave to the SPI is canceled by the SPI itself. One might suspect that the gravitational wave signal in the MIF is also canceled. However, this is not the case because the effect of gravitational waves is directly introduced to the MIF, not through the suspension wires.

To see it clearly, it is helpful to analyze the effect of the restoring force applied by the SPI's servo system. The restoring force is exactly the same as the force exerted by the gravitational wave in magnitude but opposite in the sign. Therefore, the total force exerted to the mirrors of the SPI is zero, causing no motion in the SPI. This means the MIF does not sense anything happening above.

This can be also explained by the rigid-bar picture. When the SPI is controlled, the mirrors of the MIF behave as single pendulums suspended from a rigid-bar. Therefore, the effect of gravitational waves to the MIF mirrors is equivalent to that of single pendulums; there is no cancellation of gravitational wave signals.

2.4 Theoretical Performance

The SPI is capable of suppressing differential in-line vibrations transmitted through wires of the suspension. Since this is the main transmission path of external vibrations to the MIF, the SPI can effectively reduce the noise of the MIF. However, vibrations in the other degrees of freedom are not suppressed by the SPI. Although those motions are ideally orthogonal to the in-line motion, in practice, couplings from the other degrees of freedom set a limit on the performance of the SPI.

Any noise directly introduced to the MIF is also not suppressed. This kind of noises includes, various laser noises (frequency, intensity, beam jitter), actuator noise of the MIF, and more fundamental noises such as shot noise, radiation pressure noise, and mirror's thermal noise. In this section the theoretical performance of the SPI is considered by the analysis of those effects.

2.4.1 Asymmetry of the Suspension

As mentioned in the previous section, the common motion of the suspension points ideally does not induce any noise in the MIF. However, if there is asymmetry in the pendulums suspending the mirrors of the MIF, the common motion is converted into a differential motion in the MIF. Here a quantitative analysis is done using a simple model shown in Fig. 2.9.

From now on, each of the pendulum suspending the mirrors of the MIF is called "main pendulum". Fig. 2.9 shows the parameters of the main pendulums. Here l is the length, m is the mass and γ is the viscous damping factor of the pendulum. Values with Δ represent difference of the corresponding parameter between the two pendulums. Using

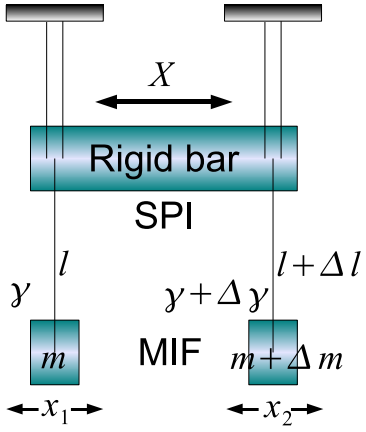

Fig. 2.9: Asymmetries of the main pendulums

those parameters, the equations of motion of the main pendulums are

$$m\ddot{x}_1(t) = -mg\frac{x_1(t)}{l} - \gamma\dot{x}_1(t), \tag{2.16}$$

$$(m+\Delta m)\ddot{x}_2(t) = -(m+\Delta m)g\frac{x_2(t)}{l+\Delta l} - (\gamma+\Delta\gamma)\dot{x}_2(t). \tag{2.17}$$

Then the transfer functions of the main pendulums in frequency domain can be written as

$$H_1(\omega) \equiv \frac{x_1(\omega)}{X(\omega)} = \frac{1}{1 + i\frac{l\gamma}{mg}\omega - \frac{l}{g}\omega^2}, \tag{2.18}$$

and

$$H_2(\omega) \equiv \frac{x_2(\omega)}{X(\omega)} = \frac{1}{1 + i\frac{(l+\Delta l)(\gamma+\Delta\gamma)}{(m+\Delta m)g}\omega - \frac{l+\Delta l}{g}\omega^2}. \tag{2.19}$$

Using H_1 and H_2, Common Mode Rejection Ratio (CMRR) is defined as

$$\mathrm{CMRR} \equiv 2\left|\frac{H_1(\omega) - H_2(\omega)}{H_1(\omega) + H_2(\omega)}\right|. \tag{2.20}$$

This quantity represents the ratio of differential motion induced by the common motion X to the common motion of the MIF. Therefore, assuming that the seismic vibration has the same magnitude in common and differential motion, CMRR gives the maximum limit of the vibration isolation ratio achievable with an SPI.

For small values of Δl, Δm and $\Delta\gamma$,

$$\mathrm{CMRR} \simeq |H_1(\omega)|\sqrt{\left(\frac{\Delta l}{g}\right)^2\omega^4 + \left(\frac{l\gamma}{mg}\right)^2\left(\frac{\Delta l}{l} + \frac{\Delta\gamma}{\gamma} - \frac{\Delta m}{m}\right)^2\omega^2}. \tag{2.21}$$

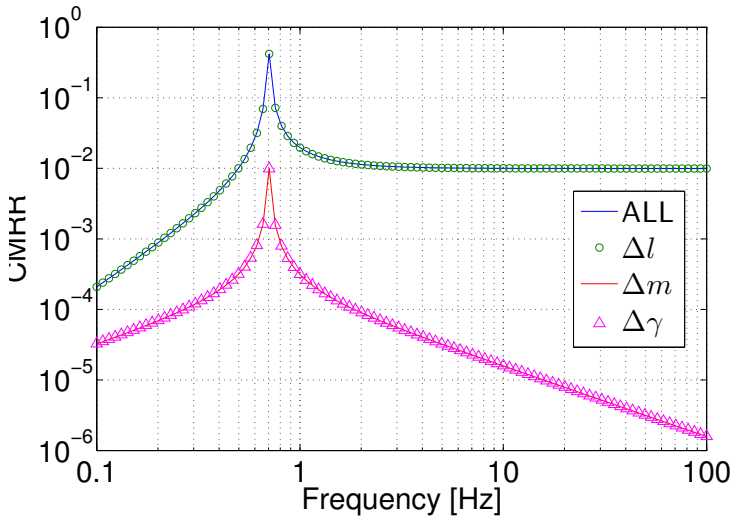

Fig. 2.10: Frequency dependence of CMRR: The blue line shows the CMRR with all asymmetries included. The green circles show the CMRR with only Δl. The red line is the CMRR with only Δm. The pink triangles show the CMRR with only $\Delta\gamma$. All asymmetries are 1%.

Frequency dependences of CMRR with different asymmetry parameters are plotted in Fig. 2.10. Here, $l = 0.5$ m, $m = 1$ kg, $\gamma = 0.1$ are used, and the magnitudes of asymmetry are all 1%. The blue curve shows the CMRR with all asymmetries included at the same time. The green circles show the CMRR with only Δl is included. The red curve is the CMRR with only Δm. The pink triangles show the CMRR with only $\Delta\gamma$.

At frequencies lower than the resonant frequency $\omega_0 = \sqrt{g/l}$ of the main pendulum, the CMRRs generally get better as frequency goes down. This is because at low frequencies the mirrors of the MIF tend to exactly follow the motion X of the suspension point. From (2.19) it is obvious that contributions from the Δ variables to H_2 decreases as ω decreases; hence, H_2 approaches to H_1 at low frequencies.

At frequencies above the resonance, the contributions of Δm and $\Delta\gamma$ to the CMRR rapidly decrease and the CMRR approaches to $\Delta l/l$. Therefore at those frequencies, the CMRR is determined by the asymmetry of the pendulum length.

2.4.2 Couplings from Other Degrees of Freedom

Since the SPI can only suppress the differential in-line motion of its mirrors, couplings from other degrees of freedom set a limit on its performance. The CMRR discussed above is one example of coupling from an SPI's non-sensitive degree of freedom, i.e. the common motion of suspension points. Here, couplings from other degrees of freedom, such as vertical or rotational motions, are discussed.

There are several types of coupling mechanisms. The first type is the sensing error of the interferometer. In principle a Fabry-Perot interferometer should be insensitive to

the motions of its mirrors in non in-line directions. However those motions are erroneously sensed if there is mis-alignment of the mirrors to the incident laser beam. The most serious mis-alignment is the offset of the beam spot on a mirror from the mirror's rotational center. If the beam spot is offset by a distance r from the center, the rotation of the mirror by an angle θ is converted to the in-line displacement of $r\theta$. Therefore, beam-centering is essential to reduce this kind of couplings.

A simple way to measure the amount of beam offset is to intentionally excite the mirror's rotational motion at a certain frequency. Then a peak with the amplitude proportional to the offset will appear in the interferometer's output at the excitation frequency. The offset can be removed by adjusting the mirror's position in y-z plane so that the peak disappears. The careful beam centering is not only needed for the MIF, but also for the SPI because the servo loop of the SPI tries to compensate the pseudo in-line signal coupled from other degrees of freedom by really moving the mirrors in the in-line direction, resulting in the introduction of additional noise.

The second type is mechanical couplings. In this case, mechanical imperfection in a suspension system converts non in-line motions in a certain stage of the suspension stack to an in-line motion in the next stage. An example of this coupling is shown in Fig. 2.11, where the pitch to in-line coupling is illustrated. Pitch rotation of the upper mass by an angle θ is converted to the translation of the lower mass by $d \sin\theta$ because of the offset d of the upper clamp points from the rotation center. To avoid this kind of couplings, precision of the machinery should be improved. However, it is empirically known that there always exist couplings of order 1% in a suspension system, even if it is manufactured with the state-of-the-art technologies.

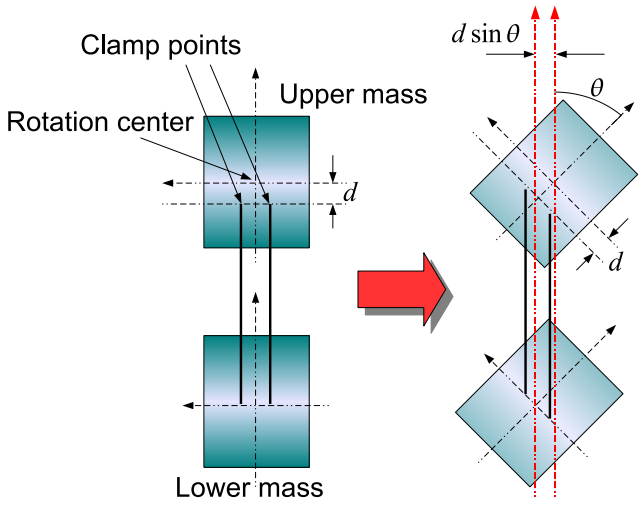

Fig. 2.11: Pitch to in-line mechanical coupling.

Since mechanical couplings occur at every stage of a suspension chain, the effect of the couplings is accumulated over the suspension stages. The SPI can suppress this accumu-

lated noise because, once converted to the in-line motion, it behaves as a normal in-line vibration at the SPI. However, the mechanical couplings which occur at the SPI stage cannot be suppressed by the SPI itself because it is at the MIF where non in-line motions appear as an in-line motion. Therefore careful design and precision manufacturing are necessary to make the main pendulums.

More fundamental type of mechanical coupling is caused from the non-parallelism of local verticality at front and end mirrors, which are kilometers apart, because of the Earth's curvature. As shown in Fig. 2.12, local vertical motions of the mirrors at each end can be decomposed to the components in the global vertical and horizontal axes. For an interferometer with arm lengths L, the angle θ between a local vertical axis and the interferometer's global verticality is $L/2R_{\rm earth}$, where $R_{\rm earth}$ is the Earth's radius of curvature. In the case of LCGT, whose L is 3 km, $\theta = 2.3 \times 10^{-4}$ rad. Therefore, the vertical to horizontal coupling is $\sin\theta \simeq 2.3 \times 10^{-4}$. This is an inevitable coupling as far as we construct interferometers on the Earth and the ultimate reason why good vertical vibration isolation is required.

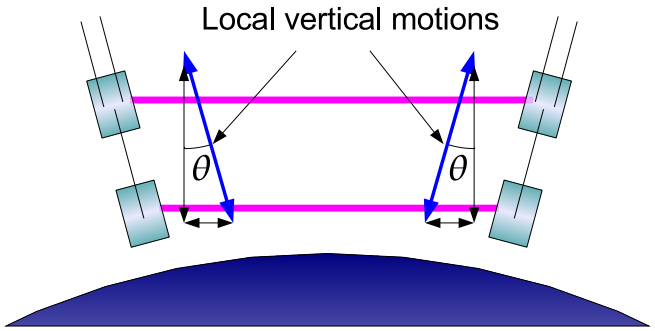

Fig. 2.12: The effect of the Earth's curvature.

2.4.3 Laser frequency noise

Laser frequency noise is not suppressed by an SPI when different lasers are used for the MIF and the SPI because the noise is directly introduced to the MIF and there is no correlation between the frequency noise of the both interferometers. On the other hand, in a configuration where the interferometers share one laser, like in Fig. 2.8, the laser frequency noise can be reduced by the SPI at frequencies lower than the resonance of the main pendulums. This is because (1) the effect of the frequency noise is coherent to both of the interferometers in this configuration and (2) at those frequencies, the motions of the SPI's mirrors are exactly followed by the mirrors of the MIF. To see this mechanism more in detail, suppose that the laser frequency is slightly shifted lower, i.e. the wavelength elongates. Since the interferometers are measuring their length using the wavelength as the unit, their lengths appear to be shorter. The servo system of the SPI applies a force

to expand its length to compensate this change. Then the main interferometer's length is also expanded accordingly, because the mirrors of the MIF follows the motion of the SPI's mirrors at low frequencies. In this way, the effective length change of the MIF caused by the frequency noise is automatically compensated by the SPI. However, at frequencies higher than the resonance, this mechanism does not work because at those frequencies the mirrors of the MIF do not follow the motion of the SPI's mirrors because of the vibration attenuation by the main pendulums.

As seen in the above, regardless of whether one laser is shared by the two interferometers or not, the laser frequency noise is not suppressed by the SPI in the observation band, which is well above the resonance of the main pendulums. Therefore, the frequency of the laser for the MIF should be well stabilized. Additionally, the laser for the SPI cannot be too noisy. If one uses the light picked up from the MIF laser for the SPI, there is no big problem because it is already stabilized. In the case of using another laser for the SPI, its frequency should be also stabilized, though the requirement of the frequency stability for the SPI is somehow relaxed from that of the MIF. The noise requirement for the SPI is discussed later in section 2.4.5.

2.4.4 Suspension Thermal Noise

Suspension thermal noise is one of the fundamental noises limiting the sensitivity of an interferometer at low frequencies. This thermal fluctuation is produced in wires at every stage of a suspension chain. To reduce this noise, the mechanical loss of the suspension system should be kept very small. However a low-loss suspension system has large resonant peaks. Especially large pendulum motions at low frequencies could make the interferometer unstable. Therefore, there is a trade-off between the suspension thermal noise and the stability of the interferometer. The SPI can be used to break this situation.

Since thermal vibrations behave just like seismic vibrations, an SPI can suppress in-line thermal vibrations produced above it. Therefore, suspension stages above the SPI can be lossy; strong damping can be applied to the upper stages to suppress the resonant peaks without increasing the suspension thermal noise in the MIF.

In our experiment, for example, the suspension system is a triple pendulum with strong eddy current damping [30] applied to the first stage. Usually, in such a configuration, the quality factor of the main pendulums are significantly reduced by the strong damping because the motions of the MIF's mirrors recoil to the damping stage and the energy is dissipated. However, once the control of the SPI is engaged, the differential motion of those mirrors is isolated from the upper stages by the virtual rigid bar formed by the SPI (Fig. 2.8(b)). Therefore, the quality factor of the differential motion of the main pendulums is kept high; consequently, the suspension thermal noise is also small. One might suspect that the high quality factor of the differential pendulum motion spoils the stability of the interferometer. However, this is not true because (1) the differential motion is rarely excited as it is well isolated from the above and (2) at the resonant frequency of the differential motion, the high quality factor also provides the actuators of the MIF with enough actuation efficiency to suppress the resonance. More rigorous explanation of the

second point can be given as follows.

A mirror with a mass m, is suspended as a single pendulum with a length l and viscous damping factor γ. Then the equation of motion is

$$m\ddot{x}(t) = -\frac{mg}{l}\left(x(t) - X(t)\right) - \gamma\dot{x}(t) + F(t), \tag{2.22}$$

where F is the force applied to the mirror (see Fig. 2.1). The transfer function from the motion X of the suspension point to the mirror's motion x is

$$H_X(\omega) \equiv \left|\frac{\tilde{x}(\omega)}{\tilde{X}(\omega)}\right| = \left|\frac{\omega_0^2}{\omega_0^2 + i\frac{\gamma}{m}\omega - \omega^2}\right| = \frac{\omega_0^2}{\sqrt{(\omega^2 - \alpha\omega_0^2)^2 + \alpha\frac{\omega_0^4}{Q^2}}}, \tag{2.23}$$

where

$$\omega_0 \equiv \sqrt{\frac{g}{l}}, \quad Q \equiv \frac{m}{\gamma\omega_0}, \quad \alpha \equiv 1 - \frac{1}{2Q^2}. \tag{2.24}$$

Since the discussion here is focused on high Q pendulums, $\alpha \simeq 1$ can be assumed. H_X has a peak at $\omega = \omega_0$ and the height of the peak is Q.

Another transfer function derived from (2.22) is,

$$H_F(\omega) \equiv \left|\frac{\tilde{x}(\omega)}{\tilde{F}(\omega)}\right| = \left|\frac{1}{m\left(\omega_0^2 + i\frac{\gamma}{m}\omega - \omega^2\right)}\right| = \frac{1}{m\sqrt{(\omega^2 - \alpha\omega_0^2)^2 + \alpha\frac{\omega_0^4}{Q^2}}}. \tag{2.25}$$

This is the response of the mirror to the force F. H_F also has a peak at exactly the same frequency as H_X with a peak height of $Q/m\omega_0^2$, which is Q times larger than the inertial response $1/m\omega^2$ of a free mass m. Although the vibration X at the suspension point is enhanced by a factor of Q, the force exerted by the servo system to suppress this motion is also enhanced by the same factor. Hence, the high quality factor of the main pendulums is not a threat to the stability of the interferometer.

2.4.5 Noise of the SPI

Any noise of the SPI, other than the differential in-line vibrations transmitted through the wires could limit the vibration isolation performance of the SPI. Those noises include laser frequency and intensity noise, electric noise of the servo system, couplings from non in-line vibrations, mirror's thermal noise, shot noise, radiation pressure noise, and so forth. They are converted to the real motion of the mirrors of the SPI by its servo system and this converted motion is transmitted to the MIF through the main pendulums. In this way the noise of the SPI is introduced to the MIF.

Various sophisticated techniques are used in the MIF to reduce the noises listed above and the same techniques can be applied to the SPI. However the requirement on the noises to the SPI is actually relaxed from that to the MIF. This is because there is one stage of passive vibration attenuation by the main pendulums between the SPI and the MIF.

Typically the main pendulums have resonant frequencies of less than 1 Hz. Then the vibration attenuation factor at 10 Hz, from which the observation band of a typical ground based interferometer starts, is over 100. Therefore, the noise of the SPI can be 100 times larger than the MIF at 10 Hz. At higher frequencies, as the isolation factor increases, the requirement is further relaxed. Therefore, the same noise reduction technology as the MIF, which is often expensive, is not necessarily needed for the SPI; it opens the possibility of reducing the cost for the construction of the SPI.

2.5 Applications to Advanced Detectors

In this section, advantages of the SPI when it is used in next generation detectors are discussed.

2.5.1 Seismic noise

Since the SPI is a vibration isolation scheme, its most important virtue is the the reduction of seismic noise. This will help expand the observation band toward lower frequencies. If the sensitivity of an interferometer is determined by the seismic noise at a certain frequency range and the vibration isolation ratio by the SPI is 20dB, the sensitivity will be improved by a factor of 10. Then the rate of the gravitational wave event detection is increased[4] by a factor of 1000 because the detectable distance is proportional to the sensitivity and the detectable volume is its cube. Detection of low frequency (1-10Hz) gravitational waves from a binary system in its early stage of inspiral can be used as an alarm for its forthcoming merger.

2.5.2 Vibration from Heat links

In cryogenic interferometers like LCGT, heat link wires have to be attached to somewhere close to the MIF's mirrors in the suspension system. The heat links are used to extract the heat produced in the mirrors by optical absorption. In the current design of the LCGT cryogenic system [19], the heat link wires are attached at only one stage above the MIF's mirrors to ensure sufficient heat conduction. However, since the heat link wires are connected to a cold stage, which is firmly fixed to the ground, extra vibration from the cold stage is introduced to the suspension system through the heat links. More over, the cold stage is connected to refrigerators which may generate larger vibrations than the ground[5].

Using an SPI, the extra vibration introduced by the heat links can be suppressed. In this case, the heat link wires are attached to the mirrors of the SPI. Even though the wires transmit vibrations to the mirrors, the servo system of the SPI suppress them. The

[4]This number is a very coarse estimation, because the event rate also depends on the shape of the noise curve of the interferometer.

[5]Efforts to develop a quiet refrigerator whose vibration is comparable to the seismic motion of Kamioka site is currently going on.

low-noise nature of the SPI is essential in this application because it is necessary to place the SPI only one stage above the main interferometer while the vibration isolation between them is not very good; whatever noise generated in the SPI is transmitted to the MIF only with the poor vibration attenuation provided by the main pendulum. Therefore, we cannot use noisy sensors for this purpose.

2.5.3 RMS reduction

Unlike other vibration isolation schemes, such as pendulums or active vibration isolation systems using accelerometers, the SPI has a good vibration isolation performance from DC. In fact, as shown in Fig. 2.10, the performance of an SPI tends to improve at low frequencies, though it is limited by vertical vibration at some point (see the section 4.3.1). The good low-frequency performance is helpful to reduce the large motion of the MIF's mirrors at low frequencies mainly due to the resonances of the multiple pendulum suspension; in other words, the root-mean-square (RMS) of the mirror's motion is suppressed. This immediately means that the stability of the interferometer can be improved by the SPI.

The stability improvement is not the only profit of the RMS reduction. Various technical noises, such as laser intensity noise, appear to the interferometer's output through coupling with the RMS motion of the MIF. Therefore, the reduction of RMS motion also helps attain the designed sensitivity of an interferometer, i.e. the sensitivity limited only by fundamental noises such as thermal noises, shot noise and radiation pressure noise.

2.5.4 Actuator noise

Actuator noise is one of the technical noises strongly associated with the RMS motion of an interferometer. It is the electric noise of driving circuits of actuators. If the input equivalent noise of the driver is V_n, and the coupling coefficient of the actuator from the driver's input voltage to the mirror's motion is α, the actuator noise is given by αV_n. To estimate the practical level of this noise, the seismic noise spectrum is assumed to be

$$x_{\mathrm{seis}} = \begin{cases} \left(\frac{10^{-8}}{f^2}\right) \mathrm{m}/\sqrt{\mathrm{Hz}} & f \geq 0.1\mathrm{Hz} \\ 10^{-6}\mathrm{m}/\sqrt{\mathrm{Hz}} & f < 0.1\mathrm{Hz} \end{cases}. \tag{2.26}$$

Then the RMS of x_{seis} is about $2 \times 10^{-7}\,\mathrm{m}$. Taking a safety factor of 10 into account, a 10 times lager actuation range is required for the actuators at low frequencies. Then $\alpha(0)V_{\mathrm{max}} = 2 \times 10^{-6}\,\mathrm{m}$, where $\alpha(0)$ is the actuation coupling at DC and V_{max} is the maximum input voltage to the actuator driver. Since op-amps with $V_{\mathrm{max}} = \pm 15\,\mathrm{V}$ are commonly used, $\alpha(0) = 7 \times 10^{-8}\,\mathrm{m/V}$. Then α is assumed to have a pendulum like response; it is constant ($\alpha = \alpha(0)$) from DC to 1 Hz and falls down as $\alpha = \alpha(0)/f^2$ above 1 Hz. Using $V_n = 1\mathrm{nV}/\sqrt{\mathrm{Hz}}$, which is the thermal noise level of a $100\,\Omega$ resistor, the actuator noise at 100 Hz is $10^{-20}\,\mathrm{m}/\sqrt{\mathrm{Hz}}$. This is comparable to the target sensitivity of LCGT, $9 \times 10^{-21}\,\mathrm{m}/\sqrt{\mathrm{Hz}}$ at 100 Hz. This is not good because in order to achieve the sensitivity limited only by fundamental noises, it is desirable that technical noises are well below the

fundamental noises, for example, by a factor of 10 or so. The RMS reduction by the SPI is helpful to reduce the actuator noise because weaker actuators (smaller α) can be used.

2.5.5 Lock Acquisition

Most of the next generation interferometers employ the optical configuration of the resonant side-band extraction (RSE) interferometer [16]. The RSE is used, in the first place, to cope with the large heat generation inside the optical components due to the absorption of transmitted high power laser energy. This difficulty can be circumvented by the use of very high finesse arm cavities at the expense of narrower observation bandwidth. In the case of the RSE interferometers, the high finesse arm cavities are made compatible with a wide bandwidth by the addition of a signal extraction mirror at the dark port. In addition, the RSE configuration allows one to change the shape of the quantum noises and optimize them to a particular source of gravitational waves. Ultimately this flexibility leads to quantum non-demolition measurements.

The high finesse cavities used in an RSE interferometer have very narrow working range. Therefore, it is generally difficult to draw the interferometer into its working point, compared to interferometers with lower finesse cavities. The RMS reduction by the SPI will help the lock acquisition process.

A rough estimation of the difficulty of the lock acquisition can be made in the following way. Suppose that the working range of an interferometer, inside which the interferometer outputs proper signal, for the mirror position is d, and the average speed of the mirror is v. Once the mirror passes by the working range, the servo system exerts a feedback force F. In order to stop the mirror within the working range, the work done by the force F should be greater than or equal to the mirror's energy of motion

$$Fd \geq \frac{1}{2}mv^2, \tag{2.27}$$

where m is the mirror's inertial mass. Therefore, the minimum force required to draw the interferometer into its working point is

$$F = \frac{mv^2}{2d}. \tag{2.28}$$

The average speed v can be calculated by integrating $2\pi f P(f)$, where $P(f)$ is the power spectrum density of the mirror motion. Roughly speaking, v is proportional to the RMS of the mirror motion[6]. Since v enters quadratically to (2.28), the reduction of the RMS by a factor of 10 will make the lock acquisition 100 times easier.

[6]This is only approximately true, because the RMS speed also depends on the shape of the displacement spectrum.

Chapter 3

1.5 m Prototype Fabry-Perot Interferometer

A 1.5 m prototype Fabry-Perot interferometer was built in the Hongo campus of the university of Tokyo to demonstrate active vibration isolation with an SPI. The purposes of this interferometer are to study practically achievable performance of an SPI and to acquire experience to better design SPIs for next generation interferometers, in particular for LCGT.

Previously, the author had built a smaller Fabry-Perot interferometer (15 cm long), equipped with an SPI [26, 27]. With this interferometer, a good vibration isolation of maximum 40dB was achieved below the resonance of the main pendulums (2Hz). However, above the pendulum frequency, where the seismic noise spectrum drops rapidly, no vibration isolation enhancement by the SPI was observed. This is because the noise at those frequencies was dominated by couplings from other degrees of freedom, most probably from vertical vibration. Therefore, during the design of the 1.5 m interferometer, special attention was paid to avoid those unwanted couplings.

The experimental apparatus for this experiment consists of a rigid-cavity mode cleaner (MC) and two 1.5 m-long Fabry-Perot interferometers (Fig. 3.1). The laser frequency is locked to the MC by the Pound-Drever-Hall (PDH) scheme[1]; the mode-cleaner serves both as a laser frequency reference and a spatial mode filter for the laser. The transmitted light from the MC is divided into two beams by a beam splitter. Then the beams are introduced to the interferometers. The main interferometer is suspended from the upper interferometer (SPI). Using the SPI, the active vibration isolation of the MIF is realized.

In this chapter, the optical configuration of the interferometers is described first. Then the details of the suspension system are described. Finally, the control scheme and the operation procedure are explained.

[1] see Appendix B

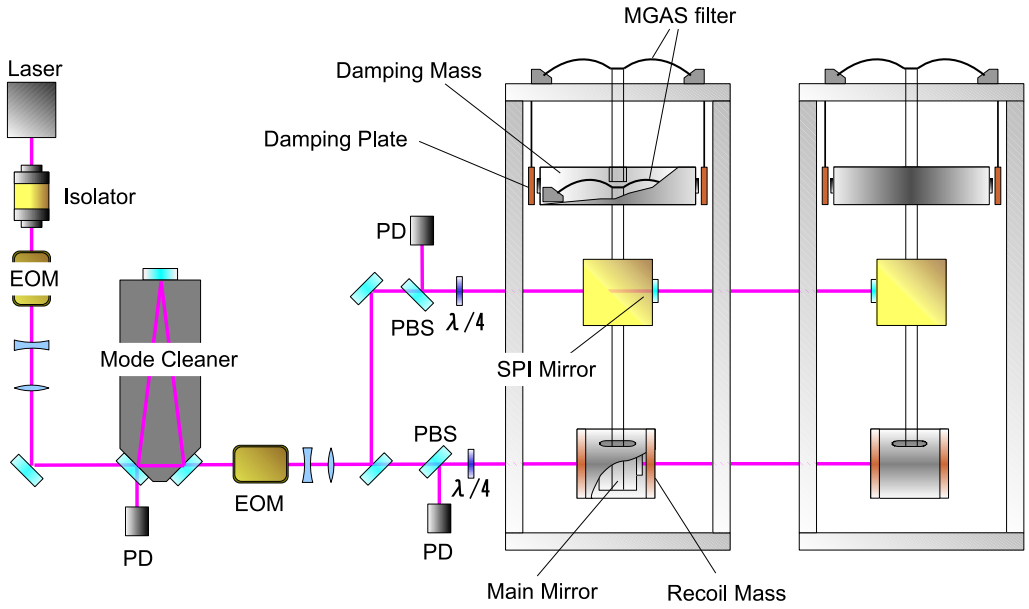

Fig. 3.1: An overview of the experimental setup.

3.1 Optics

3.1.1 Laser and mode cleaner

Laser Bench

Laser A 200 mW Nd:YAG laser (InnoLight Mephisto OEM 200NE, wavelength=1064 nm) is used in this experiment. The laser is capable of changing its output frequency in two ways. Fine and fast adjustment can be made through a piezoelectric (PZT) actuator attached on the laser crystal; a small deformation of the crystal caused by the PZT actuator changes the resonant frequency of the crystal. Wider range, but slow, tuning of the frequency can be performed by changing the temperature of the crystal using Peltier devices on it. The output power of the laser can also be varied by changing the amount of current supplied to the laser diode. The bandwidth of the diode current control is limited to about 5kHz. The laser is internally equipped with the laser diode's temperature and current stabilization system. However, during this experiment the current stabilization was turned off because it interferes with the external intensity stabilization system described in section 3.4.1.

Attenuator, modulator and isolators Fig. 3.2 shows the optical configuration of the laser and the mode cleaner. The output light from the laser first enters a power attenuator

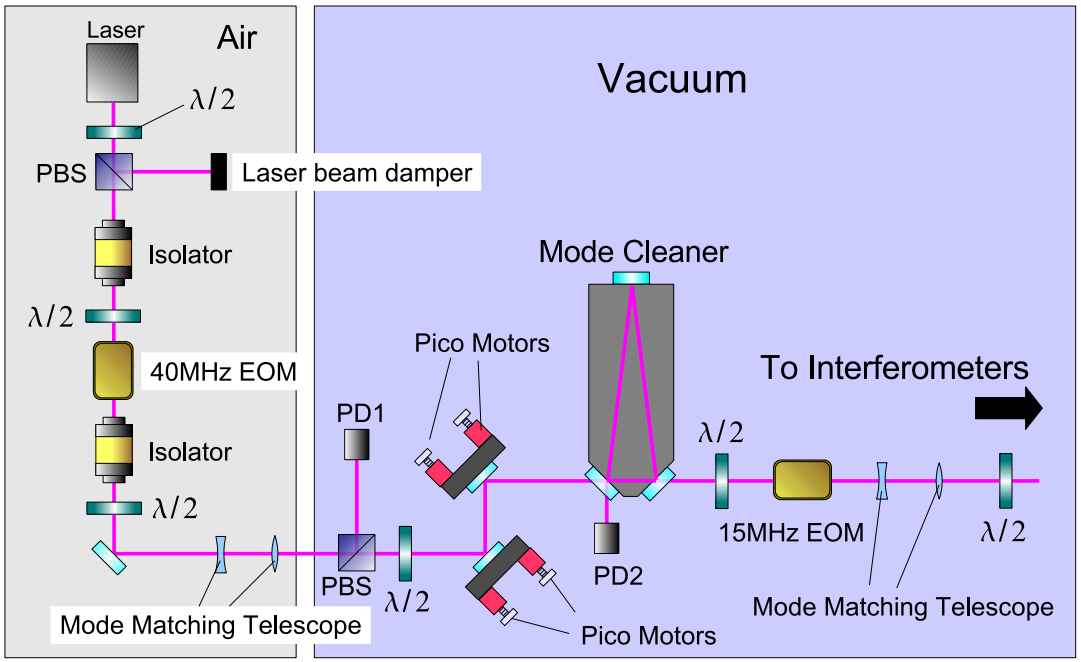

Fig. 3.2: The optical configuration of the laser and the mode cleaner

formed by a half-wave plate (HWP) and a polarizing beam splitter (PBS). The attenuation ratio can be changed by rotating the polarization axis using the HWP. The light reflected by the PBS is absorbed by a beam damper, which is made of dozens of razor blades tightly bound together. After the attenuator, the laser power is about 80 mW. This power is chosen to prevent the saturation of photo detectors (PDs) used at the detection ports of the interferometers.

The attenuated light goes through two Faraday-isolators (OFR IO-2-YAG and IO-5-1064-HP) to avoid the light reflected by optical components of the interferometers from going back to the laser; otherwise it would cause instability of the laser, which is called optical feedback. An electro-opto modulator (EOM) is inserted between the isolators to phase-modulate the laser at 40 MHz. A NewFocus model 4004 IR broadband EOM is used here. Since the EOM behaves like a large capacitor, an RF capacitance-driver is used to drive the large capacitive load. An HWP is placed just before the EOM to adjust the polarization axis to coincide with the modulation axis of the EOM. This is because improper alignment of the input light polarization causes amplitude modulation in the transmitted light at the phase modulation frequency, which introduces a DC offset to the PDH signal of the MC.

Mode matching for the mode cleaner A combination of concave and convex cylindrical lenses is used as a telescope for shaping the spatial profile of the laser beam to match the mode of the MC. The focal lengths of the concave and convex lenses are −200 mm and

200 mm, respectively. The waist radius of the MC's fundamental proper mode is 0.2 mm located 2.6 m away from the laser. In order to achieve the maximum coupling of the beam with the MC, optimal positions of the lenses are first calculated by a Mathematica program written by the author. It calculates the beam waist parameters (position and size) given a set of the lens positions. Then the optimal set of lens positions is searched by minimizing the difference between the calculated waist parameters and the desired ones using two-dimensional Newton-Rapson method. In reality, the focal lengths of the lenses are not exactly the values specified in the catalogue. Therefore fine adjustment of the lens positions were done by cut-and-try; the beam profile around the MC was measured by a beam profiler (Data Ray BeamScope-P7) and the lens positions were adjusted so that the desired waist size and position were achieved.

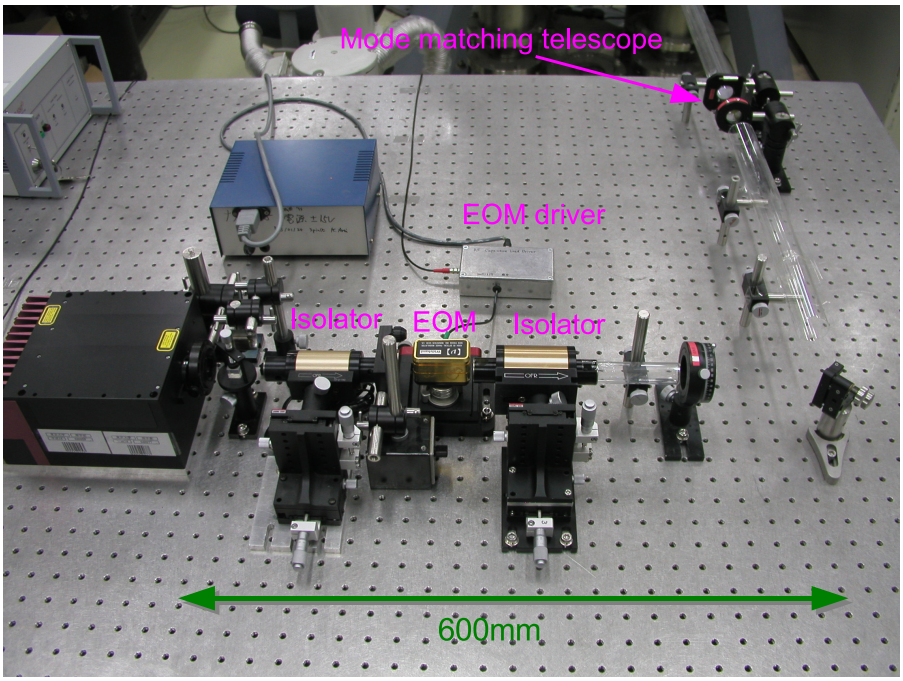

Fig. 3.3: The optical components on the laser table. During the operation of the interferometers, those components are covered by cardboard boxes to shield them from the air flow in the laboratory.

Intensity monitor

All the components described so far are placed in the air. After the telescope, the light is introduced to a vacuum chamber through an anti-reflection coated optical window manufactured by CVI.

Inside the chamber, the light is divided by a PBS to pick up the light used for the intensity stabilization. The ratio between the powers of the transmitted and reflected light

can be changed by rotating the HWP placed after the second isolator. About 5 mW is picked up here and received by a DC photo detector (PD1) for the intensity stabilization.

The transmitted light from the PBS goes through an HWP for the fine adjustment of the polarization angle to optimum for the mode cleaner.

The details of the intensity stabilization servo is described in section 3.4.1.

Mode Cleaner

The mode cleaner is a 20 cm long triangular cavity (Fig. 3.4). The input and output mirrors (M1 and M2 in Fig. 3.4, respectively) are flat mirrors with power reflectivities of 99.9%. The end mirror (M3) is a concave mirror with a radius of curvature 300 mm, and its power reflectivity is more than 99.99%. The mirrors are manufactured by Japan Aviation Electronics Industry, Ltd. with the ion-beam spattering technique. The input and output mirrors are optimized for the incident angle of 43.6° and S polarization. The finesse calculated from the specifications of the mirrors is 3140.

The spacer of the MC is made of Super Invar, a very low thermal-expansion alloy of iron, nickel, and cobalt. Its typical thermal expansion coefficient is 6×10^{-7}/K. The MC is held rigidly from the optical table in the vacuum chamber.

In order to align the incident beam to the proper mode of the MC, the light is reflected twice by mirrors with Picomotors$^{\mathrm{TM}}$, small linear electric actuators, before introduced to the MC. Picomotors are used to change the orientations of the mirrors. With Picomotors, the alignment of the beam can be remotely adjusted. The reflected light from the input mirror is received by a resonant photo-detector tuned to 40 MHz (PD2 in Fig. 3.2) to obtain the PDH signal.

Optical performance The finesse of the MC was measured by sweeping the laser frequency with the temperature control. A slowly and uniformly increasing voltage (60 mV/sec) was applied to the temperature control terminal of the laser. The transmitted light power of the MC was monitored by a photo-detector. Fig. 3.5 shows a time series of the photo-detector's output. As the laser frequency is swept, the transmitted light power exhibits a peak when the frequency passes by the resonant condition. The interval of the peaks (4.7 sec) corresponds to the FSR of the cavity (720 MHz) calculated from the cavity length. Therefore, the frequency sweep rate is determined as 150 MHz/sec. A zoomed plot of a peak is shown in the lower part of Fig. 3.5. The FWHM (Full Width Half Maximum) of the peak is 1.96 msec = 290 kHz. Since the finesse $\mathcal{F}$ = FSR/FWHM, the measured finesse of the MC is 2400. The power transmissivity of the MC was 50%.

If the low finesse and transmissivity are only due to the loss of the mirrors, the amount of the loss can be estimated as follows. Suppose that R_0 and T_0 are the power reflectivity and the transmissivity of the mirrors without loss. Then, $R_0 + T_0 = 1$ is satisfied. In reality there is some loss in a mirror. Assuming that L_R is loss to the reflectivity and L_T to the transmissivity,

$$(R + L_R) + (T + L_T) = 1, \qquad R \equiv R_0 - L_R, \quad T \equiv T_0 - L_T. \tag{3.1}$$

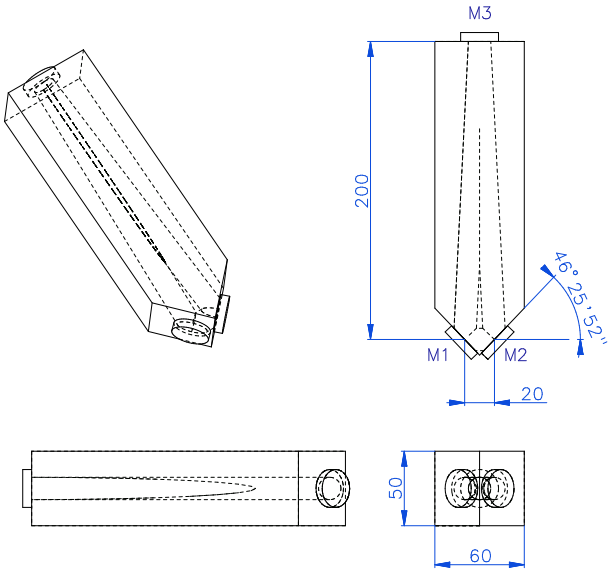

Fig. 3.4: CAD drawings of the mode cleaner. The input and output mirrors (M1,M2) are flat mirrors with power reflectivities of 99.9%. M3 is the end mirror with more than 99.99% power reflectivity, and its radius of curvature is 300 mm.

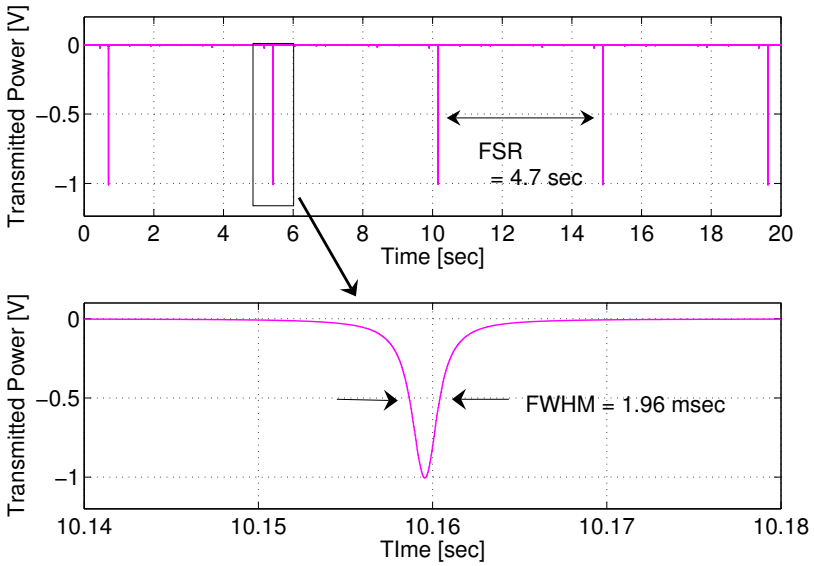

Fig. 3.5: A finesse measurement. The vertical axes are the output voltage of a photo-detector placed at the transmission port of the MC. The laser frequency was swept by changing the temperature of the laser crystal. The sweep speed is 150 MHz/sec. The lower graph shows the magnified plot of a peak.

Using R and assuming that the reflectivities of the input and output mirrors are the same,

$$\mathcal{F} = \frac{\pi\sqrt{R}}{1-R} = \frac{\pi\sqrt{R_0 - L_R}}{1 - R_0 + L_R}. \tag{3.2}$$

Using $R_0 = 0.999$ and $\mathcal{F} = 2400$, L_R is deduced to be 300 ppm. Similarly, the transmissivity $T_{\rm MC}$ of the MC is

$$T_{\rm MC} = \frac{T\ 2}{(1-R)^2} = \left(\frac{1 - L_T - R_0}{1 + L_R - R_0}\right)^2. \tag{3.3}$$

Then, L_T=80 ppm is concluded from $R_0 = 0.999$, L_R=300 ppm, and $T_{\rm MC} = 0.5$.

The losses estimated above are fairly large. This might be caused from the contamination of the mirrors' surfaces by coal tar smoke, which was accidentally introduced to our laboratory because of the wrong placement of an exhaust vent in the construction site next to our building during the assembly of the interferometer. However, there are still other possible explanations to the low finesse and transmissivity.

As to the finesse, the reflectivities of the mirrors may be really lower than the specification. This happens when the incident angle of the beam is different from the optimal one.

The lower transmissivity can be caused from (1) poor mode matching of the incident laser beam, and (2) asymmetry in the reflectivities of the input and output mirrors. Indeed, the incident light has somehow distorted profile. The distortion is caused by the 40MHz EOM as the beam diameter there (1.2 mm) is comparable to the aperture of the EOM (2 mm), whereas the beam diameter recommended by the manufacturer is less than 1/3 of the aperture. The beam profiles before and after the MC are shown in Fig. 3.6. In order to account for the 50% transmissivity only by the asymmetry of the reflectivities, the amount of the asymmetry should be about 0.1%.

Probably, all of those imperfections contribute somehow to the degradation of the finesse and the transmissivity.

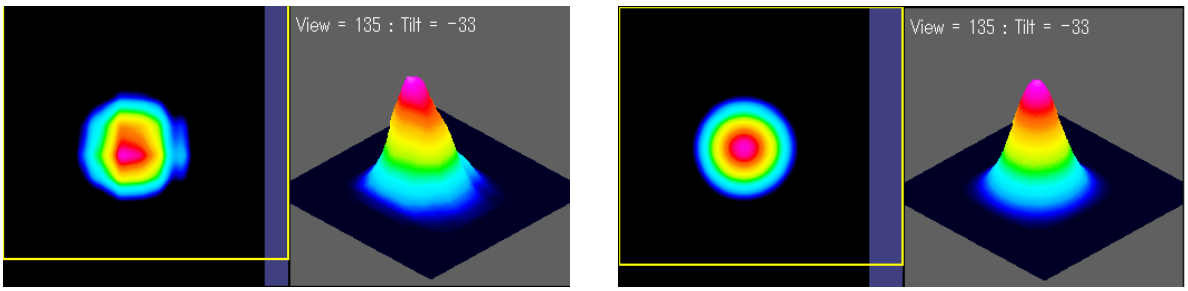

Before MC After MC

Fig. 3.6: Beam profiles of the laser before and after the mode cleaner.

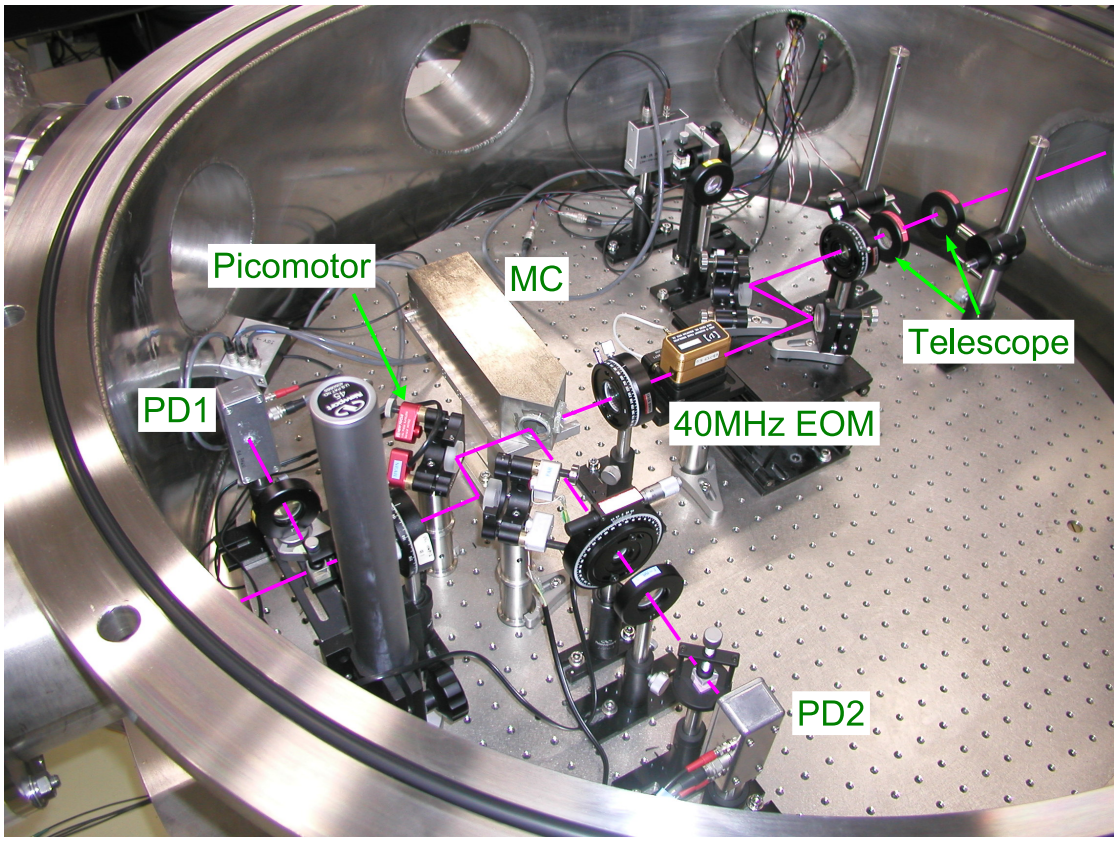

Fig. 3.7: Inside the MC tank.

3.1.2 Main and Suspension Point Interferometers

The transmitted light from the MC is phase modulated again by an EOM, this time at 15 MHz this time. This modulation is used for the control signal extraction of both the main and the suspension-point interferometers. A NewFocus model 4005 IR resonant-EOM is used here. A HWP is inserted before the EOM to adjust the polarization to match the modulation axis of the EOM. After the EOM, the profile of the laser is converted again by a set of lenses to match the main and the suspension point interferometers. The first lens is concave with a focal length $f = -200$ mm, and the second one is a convex lens with $f = 200$ mm.

The MIF and the SPI are optically identical interferometers with the length of 1.5 m. The front mirrors are flat and the power reflectivity is 99%. The radius of curvature of the end mirrors is 2 m and the reflectivity is 99.5%. The finesse of the interferometers calculated from the specifications is 420. The mirrors are 1 inch in diameter, 6 mm thick and manufactured by CVI.

Table 3.1: Parameters of the MIF and the SPI.

Length	1.5 m
Front mirror reflectivity	99%
End mirror reflectivity	99.5%
Front mirror curvature	flat
End mirror curvature	2 m
Designed finesse	420
Beam waist position	On the surface of the front mirror
Beam waist size ($1/e^2$ radius)	0.54 mm

The optical configuration of the main and suspension point interferometers is schematically shown in Fig. 3.8. The laser is split into two beams by a beam splitter after the mode matching lenses. Each beam is transmitted through a circulator formed by a polarizing beam splitter (PBS) and a quarter wave plate (QWP). The polarization of the light is adjusted by the HWP after the telescope so that the transmission of the PBS is maximized. Then the beams are introduced to the interferometers after reflected twice by mirrors with Picomotors. Those mirrors are used to align the beams to the axes of the interferometers. The reflected light beams from the interferometers are picked up by the circulators and received by photo detectors (PD3, PD4). PD3 and PD4 are resonant photo detectors tuned to 15 MHz and their outputs are used to obtain the PDH error signals of the interferometers.

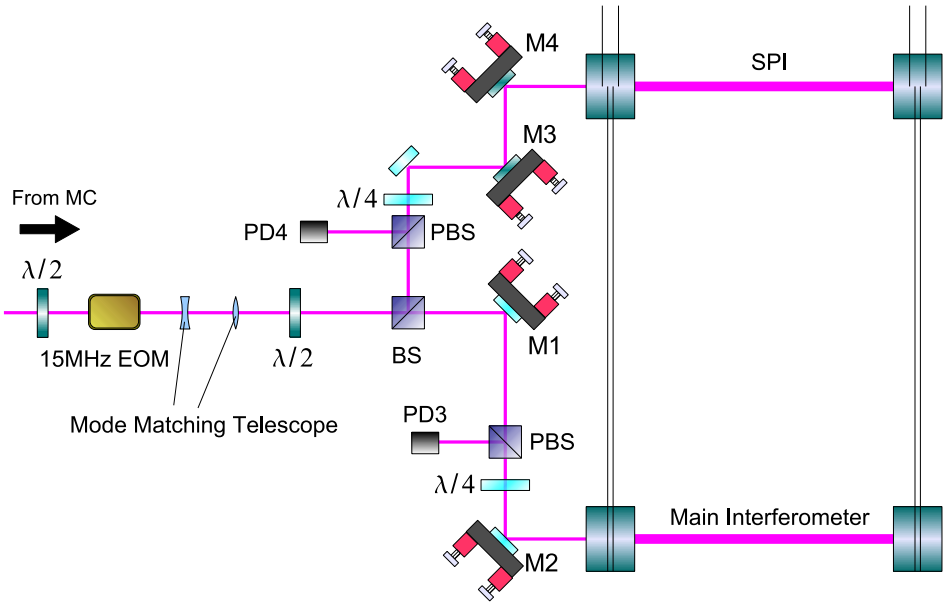

Fig. 3.8: The optical configuration of the MIF and the SPI

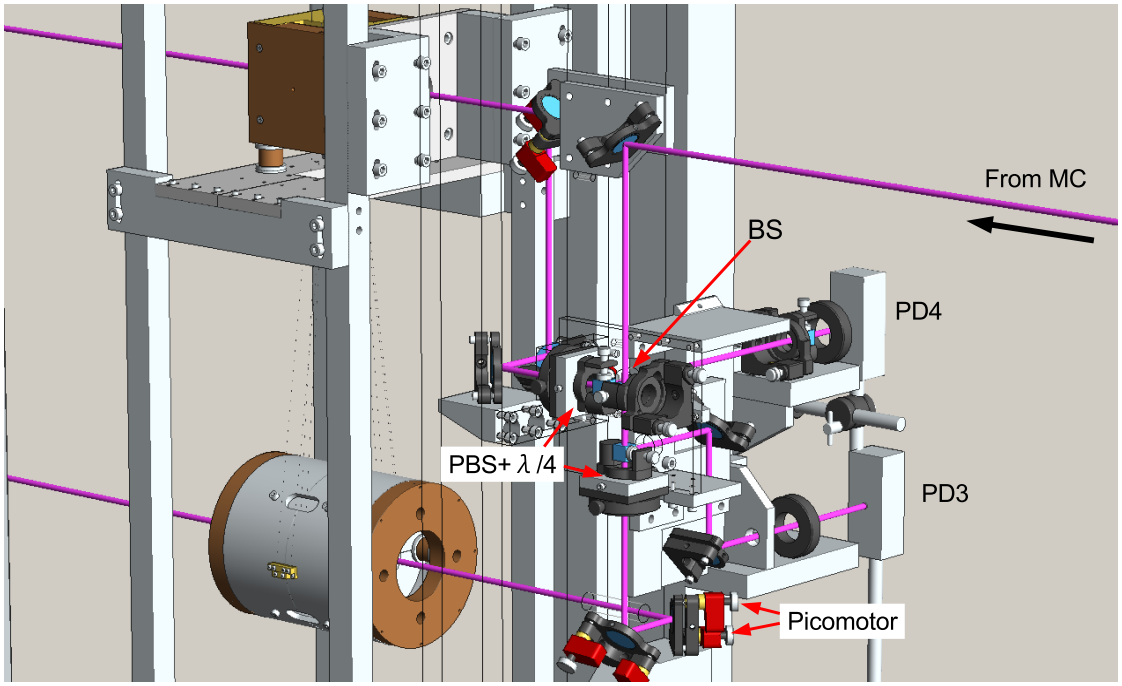

Fig. 3.9: A 3-dimensional illustration of the optics in the front tower chamber.

3.2 Suspension system

3.2.1 Overview

The overview of a suspension tower for the mirrors of the main and the suspension point interferometers is shown in Fig. 3.10. It is basically a triple pendulum with two stages of low-frequency vertical springs, called Monolithic Geometric Anti-Spring (MGAS) filters (see section 3.2.3). Both MGAS filters are tuned to have the resonant frequencies around 0.2 Hz.

On the top plate of the suspension, an MGAS filter is installed. From the center of the filter, the first stage of the suspension, called the damping mass, is suspended. Strong eddy-current damping [30] is applied to this stage using attached neodymium magnets and a copper plate (damping plate) surrounding the stage. Another MGAS filter is held inside the damping mass and the second stage is suspended from it. The second stages of the suspensions form the suspension point interferometer, while the final stages form the main interferometer. Each mirror of the MIF is surrounded by a recoil mass, which is suspended from the same stage as the MIF mirror.

Each stage of the suspension is equipped with several coil-magnet actuators to control the position and the orientation of the stage. Vertical actuators are installed to the damping stage and the second stage, in order to compensate the slow drift of the vertical working points of the MGAS filters. The MIF mirrors are actuated from the recoil masses.

The overall height of the suspension system is 1 m. The length of the main pendulums is 40 cm and the distance between the first and the second stage is 20 cm. As to the length of the wires suspending the first stage, the front and the end suspension towers have different lengths; it is 25 cm for the front tower and 35 cm for the end tower. This asymmetry is intensionally introduced to avoid common-mode rejection for the following reason.

Since the two towers are only separated by 1.5 m, the seismic motion is mostly common to the both towers. If the transfer functions of the two towers are identical, the common motion is transmitted to the common motion of the mirrors, which is not sensed by the interferometers. Thus, the seismic noise is significantly reduced, especially at low frequencies. This common-mode rejection does not occur in large interferometers, because the seismic motions on locations kilometers apart are supposed to be uncorrelated. The asymmetry of the wire length is introduced to simulate the situation of large interferometers by making the transfer functions asymmetric.

In this section, the details of the suspension systems are described. First, the commonly used sensors and actuators in this experiment are described. Then the theory and the design procedure of MGAS filters are given. On the basis of those preliminary sections, each stage of the suspension system is then described in detail,

3.2.2 Sensors and Actuators

In many parts of the suspension system, photo-sensors (PSs) and coil-magnet actuators are used. Before going into the details of the suspension systems, brief descriptions of them

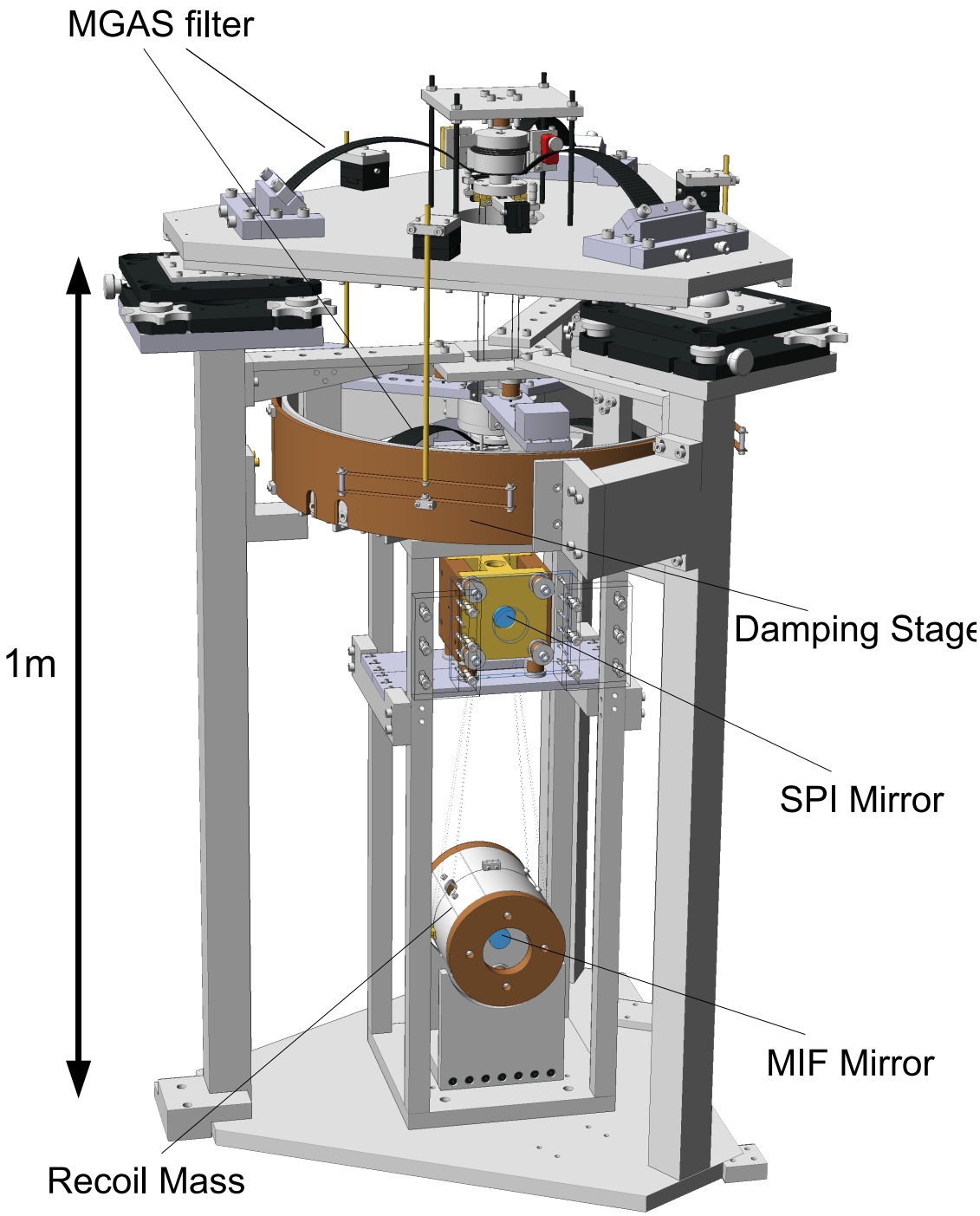

Fig. 3.10: An overview of the suspension system.

are given. Although not used during the operation of the interferometers, an optical lever sensor is described here because it is used for the characterization of the suspension.

Photo Sensor

Photo-sensor is a contact-free displacement sensor. In Fig. 3.11, the structure of a photo-sensor used in this experiment is shown schematically. It basically consists of a light emitting diode (LED) and two photo detectors. To measure a distance the photo-sensor is faced to the surface of an object to which one wants to measure the distance. The light emitted from the LED is reflected back to the PDs from the surface.

The amount of light power received by the PDs depends on the distance between the sensor and the surface. When the distance is large, the received light power is inversely proportional to the distance because the smaller the distance, the larger the solid angle occupied by the PDs is observed from the LED, i.e. larger portion of the emitted light is received. On the contrary, when the distance is small, the outputs of the PDs are proportional to the distance. This is because the light from the LED is shadowed by the edges of the PDs; only the light which goes through the small aperture (denoted by a in Fig. 3.11) can reach to the PDs. When a is small, the received light power is small.

As seen above, a photo-sensor has two working regions. The first (large distance) region is coarse but has wide range. In the second (small distance) region, the sensor is more sensitive but the working range is smaller. In this experiment, only the second region was used.

The LEDs used in this experiment are Hamamatsu Photonics L2656 infra-red LED and the photo detectors are S2386-18K, also from Hamamatsu Photonics. The ultimate sensitivity of a photo-sensor is limited by shot noise. A typical shot noise level of photo-sensors in this experiment is of the order of $10^{-10}\,\mathrm{m}/\sqrt{\mathrm{Hz}}$.

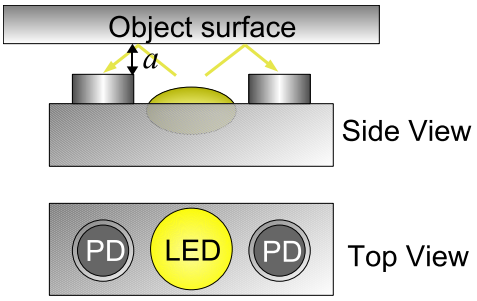

Fig. 3.11: Photo-sensor

Coil-Magnet actuator

A coil-magnet actuator is a non-contact device that exerts a force on a body. It consists of a coil and a bar-magnet (Fig. 3.12). Usually, the bar-magnet is attached to the body to

be actuated. The magnet is surrounded by a coil; the magnetic field produced by the coil exerts a force to the bar-magnet. The sign and the magnitude of the force can be changed by the sign and the amount of electric current on the coil.

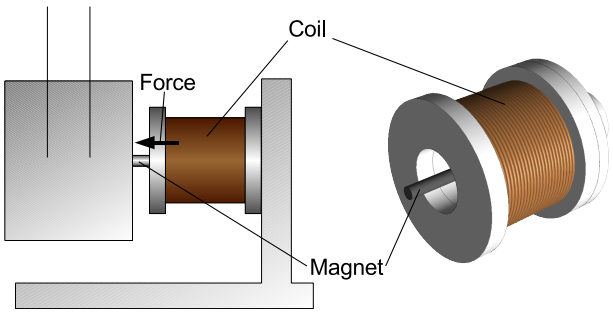

Fig. 3.12: Coil-magnet actuator

To make the coils used in the experiment, 0.2 mm thick enameled copper wires were coiled carefully using a semi-automatic coiling machine, developed by Koji Arai and Kenji Numata. The number of turns were changed according to the required force. The bar-magnets are neodymium magnets of various diameters.

Optical Lever

Optical lever is a sensor to measure the angular fluctuation of an object. This sensor was used to measure the rotational resonant frequencies of the suspension stages. It consists of a laser and a position sensitive detector (PSD). A typical setup is shown in Fig. 3.13. The laser light is reflected by a surface of the object to be measured, and received by the PSD. If the orientation of the surface changes, the beam spot on the PSD moves accordingly. The motion of the spot by a distance d on the PSD corresponds to the rotation angle $\theta = d/l$ of the surface, where l is the distance between the surface and the PSD.

Hamamatsu Photonics S5991-01 improved-surface-split type PSD was used in this experiment. The laser source is a visible light (red) laser diode equipped in a level gauge (Transverse Industries, Laser Leveler TI-328-4).

3.2.3 MGAS filter

As described in section 2.1, it is difficult to realize low resonant-frequency in the vertical direction because the stiffness required to hold a payload contradicts the softness required for the low resonant frequency. Monolithic Geometric Anti-Spring (MGAS) is a low-frequency vertical spring which can evade the above contradiction. The idea of geometric anti-spring (GAS) was first proposed by Blair et al. [31]. Then it was improved by DeSalvo and his colleagues[32][33]. Those GAS filters all had composite structure. The monolithic configuration of the GAS filter was then developed by DeSalvo group[34].

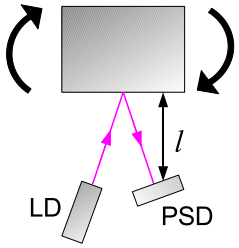

Fig. 3.13: Optical lever

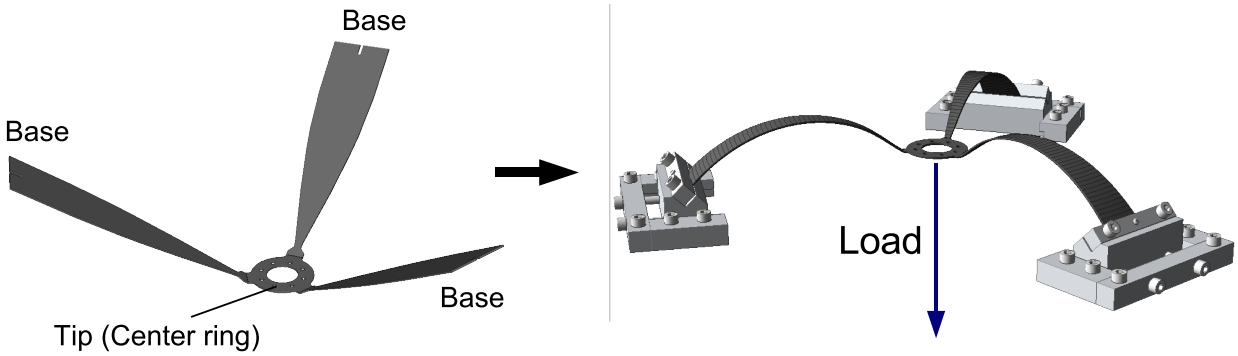

Fig. 3.14: MGAS filter. The blades are originally straight and bent by a load. The bases of the blades are clamped at a fixed angle.

An MGAS filter consists of a set of radially converging blades. The blades are straight when unloaded, and bent by a vertical load (Fig. 3.14). The bases of the blades are clamped by massive structures at a fixed angle θ_0.

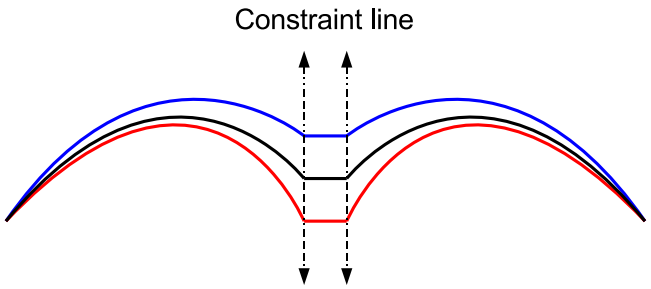

Fig. 3.15: The geometric constraint of the MGAS.

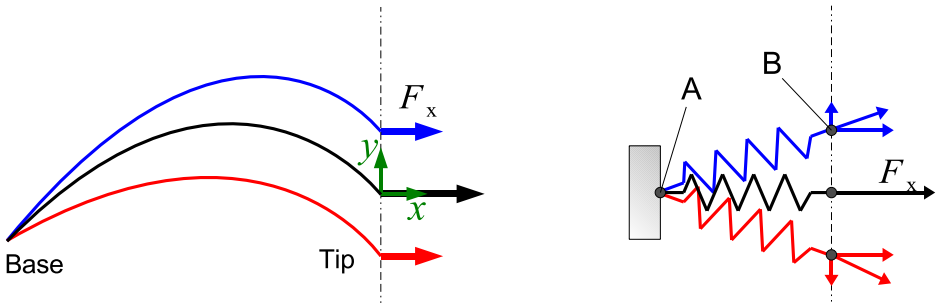

Fig. 3.16: An intuitive interpretation of the working principle of an MGAS filter.

Intuitive Interpretation of the Working Principle

Intuitive explanation of the working principle of the MGAS filter can be given as follows. The blades of an MGAS filter are compressed horizontally by pushing each other at the center. As a result of the symmetry of the filter around its center, the horizontal compression forces cancel out each other. Therefore, the center ring of the MGAS filter does not move horizontally; the motion of the tips of the blades are geometrically constrained to purely vertical direction (Fig. 3.15). It is this geometrical constraint that produces an anti-spring effect.

In Fig. 3.16 (a), side views of a blade at three different vertical positions are shown. The black blade represents the optimum vertical position, i.e. the optimum working point. It is chosen to be the position where the horizontal compression force F_x is largest. Now

it is useful to introduce an effective potential U_{h} which produces F_x as

$$F_x = -\frac{\partial U_{\mathrm{h}}}{\partial x}. \tag{3.4}$$

The origin of x and y axes is taken to be the tip position of the blade at the working point. The physical interpretation of U_{h} is the energy built up in the blade by the horizontal compression. Note that U_{h} is not the total elastic energy stored in the blade.

Since F_x has its maximum at the working point,

$$\frac{\partial F_x}{\partial y} = -\frac{\partial^2 U_{\mathrm{h}}}{\partial y \partial x} = 0, \quad \frac{\partial^2 F_x}{\partial y^2} = -\frac{\partial^3 U_{\mathrm{h}}}{\partial y^2 \partial x} < 0. \tag{3.5}$$

All partial derivatives are taken at $x = y = 0$ here and for the rest of this section. If the form of U_{h} is assumed to be $U_{\mathrm{h}}(x, y) = U_{\mathrm{hx}}(x)U_{\mathrm{hy}}(y)$,

$$\frac{\partial F_x}{\partial y} = -\frac{\partial U_{\mathrm{hx}}(x)}{\partial x}\frac{\partial U_{\mathrm{hy}}(y)}{\partial y} = \frac{F_x}{U_{\mathrm{hy}}}\frac{\partial U_{\mathrm{hy}}(y)}{\partial y} = 0, \tag{3.6}$$

and,

$$\frac{\partial^2 F_x}{\partial y^2} = -\frac{\partial U_{\mathrm{hx}}(x)}{\partial x}\frac{\partial^2 U_{\mathrm{hy}}(y)}{\partial y^2} = \frac{F_x}{U_{\mathrm{hy}}}\frac{\partial^2 U_{\mathrm{hy}}(y)}{\partial y^2} < 0, \tag{3.7}$$

Since $F_x/U_{\mathrm{hy}} > 0$,

$$\frac{\partial U_{\mathrm{hy}}(y)}{\partial y} = 0, \quad \frac{\partial^2 U_{\mathrm{hy}}(y)}{\partial y^2} < 0. \tag{3.8}$$

Therefore, U_{h} also has a maximum at the optimum working point. Then U_{h} can be written as,

$$U_{\mathrm{h}} = (U_0 - \alpha y^2 + \mathcal{O}(y^3))U_{\mathrm{hx}}, \tag{3.9}$$

where α is some positive constant. This potential produces an anti-spring force F_y in the vertical direction,

$$F_y = -\frac{\partial U_{\mathrm{h}}}{\partial y} = \left(2\alpha y + \mathcal{O}(y^2)\right) U_{\mathrm{x}}. \tag{3.10}$$

The magnitude of F_y increases as $|y|$ increases and its direction is outward from the working point. Therefore, this force acts as a spring with a negative spring constant $-2\alpha U_{\mathrm{x}}$.

An example of a system which has this kind of behavior is a spring under compression (Fig. 3.16(b)). The spring is fixed at one end (A in the figure) by a freely-revolving joint and the other end (B) is constrained to move only in the vertical direction. As end B goes up (down), the stored compression energy is released by pushing end B up (down) to escape from the equilibrium point. This is an analogical explanation of the MGAS filter's anti-spring effect.

The negative spring constant combined with the positive spring constant of the blade's restoring force gives a very small total spring constant around the optimum working point. Since the anti-spring effect is a local effect around the optimum working point, the ability to hold a heavy payload is maintained.

The maximum of U_{h} is produced by the geometric constraint shown in Fig. 3.15. Therefore the anti-spring described above is called "geometric anti-spring".

Theory of the MGAS filter

An extensive study on the theoretical analysis of MGAS filters was done in [34]. Here, the essential part necessary to design an MGAS filter of [34] is abstracted. Then, the practical design procedure of the filters used in this experiment is described in the next section.

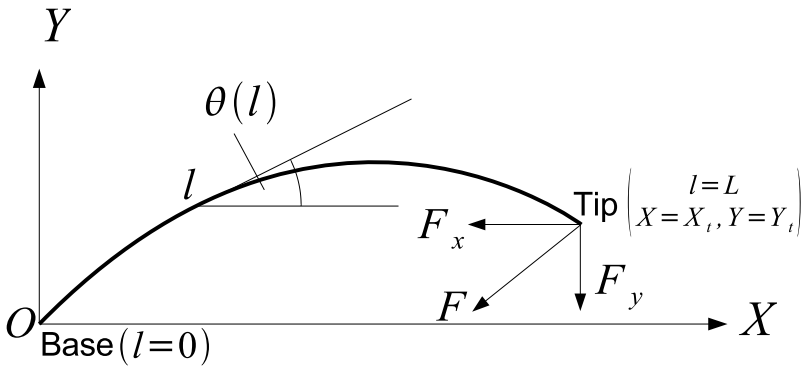

Fig. 3.17: Coordinate systems of an MGAS blade.

A quasi-static model of an MGAS blade can be constructed as follows. Fig. 3.17 shows a blade bent by an external load F at the tip. The origin of a Cartesian coordinate X-Y is taken at the base of the blade. Another coordinate, a curvilinear coordinate l along the blade length, is introduced to indicate a point on the blade; $l \in [0, L]$, where L is the length of the blade. The blade has a width profile $w(l)$ and an uniform thickness d. $\theta(l)$ is the angle between the tangent of the blade at l and X axis. The base of the blade is supported by a massive structure at a fixed angle $\theta(0) = \theta_0$. The tip of the blade also has a fixed inclination $\theta(L) = \theta_L$.

The potential energy of the blade is

$$U = \int_0^L \left\{ \frac{1}{2} EI\,(l) \left[\frac{d\theta\,(l)}{dl} \right]^2 - F_x \cos\theta\,(l) - F_y \sin\theta\,(l) \right\} dl. \tag{3.11}$$

F_x and F_y are the horizontal and vertical components of the load F, respectively. $I \equiv w\,(l)\,d^3/12$ is the moment of inertia of the blade cross-section at l. In order to make it a dimensionless equation, a dimensionless energy $\tilde{U}$ is introduced,

$$\tilde{U} = \frac{12L}{Ed^3 w\,(0)} U. \tag{3.12}$$

Then, (3.11) is rewritten as

$$\tilde{U} = \int_0^1 \left\{ \frac{1}{2\gamma\,(\xi)} \left[\frac{d\theta\,(\xi)}{d\xi} \right]^2 - G_x \cos\theta\,(\xi) - G_y \sin\theta\,(\xi) \right\} d\xi, \tag{3.13}$$

where $\xi = l/L$ and $\gamma(\xi) = w(0)/w(\xi L)$. G_x and G_y are dimensionless parameters which correspond to the horizontal and the vertical forces.

$$G_i = \frac{12L^2}{Ed^3 w(0)} F_i, \qquad i = x, y. \tag{3.14}$$

Given a certain blade profile $\gamma(\xi)$, this system is characterized by G_x and G_y.

In the equilibrium, the variation $\delta\tilde{U}$ with respect to $\theta(l)$ should be zero. From the Euler-Lagrange equation,

$$\frac{d}{d\xi}\left[\frac{1}{\gamma(\xi)}\frac{d\theta(\xi)}{d\xi}\right] - G_x \sin\theta(\xi) + G_y \cos\theta(\xi) = 0. \tag{3.15}$$

By introducing a new parameter $p(\xi)$,

$$p(\xi) = \frac{1}{\gamma(\xi)}\frac{d\theta(\xi)}{d\xi}, \tag{3.16}$$

a system of ordinary differential equations is obtained:

$$\frac{dp(\xi)}{d\xi} = G_x \sin\theta(\xi) - G_y \cos\theta(\xi), \tag{3.17}$$

$$\frac{d\theta(\xi)}{d\xi} = \gamma(\xi)\, p(\xi). \tag{3.18}$$

Since $\gamma(0) = 1$, $1/p(0)$ corresponds to the radius of curvature of the blade at $l = 0$.

The angular profile $\theta(\xi)$ of the blade is a solution of the above equations. Since the initial and the final values of θ are fixed to $\theta(0) = \theta_0$ and $\theta(L) = \theta_L$, this is a boundary value problem. To solve the problem numerically, the author implemented a Mathematica program which solves the boundary value problem by an algorithm called "shooting method". The details of the shooting method are described in Appendix C. Once $\theta(\xi)$ is determined, the position (x_t, y_t) of the blade's tip is obtained by computing the following integrals:

$$x_t = \int_0^1 \cos\theta(\xi) d\xi, \tag{3.19}$$

$$y_t = \int_0^1 \sin\theta(\xi) d\xi. \tag{3.20}$$

Here x_t and y_t are normalized by the blade length L,

$$x_t = \frac{X_t}{L}, \quad y_t = \frac{Y_t}{L}. \tag{3.21}$$

In this way, the equilibrium point (x_t, y_t) of the blade is completely determined by G_x and G_y, provided the blade shape $\gamma(\xi)$ and its initial and final angles, θ_0, θ_L, are fixed.

The next task is to find the optimum working point to realize a low resonant frequency. Since the blade's tip is constrained to move only in the y direction, it is interesting to draw a locus of the solutions in G_y-y plane with a constant x_t. This is equivalent to solving (3.17) (3.18) under an integral constraint

$$x_{\rm t}^{\rm fix} = \int_0^1 \cos\theta(\xi) d\xi, \tag{3.22}$$

by varying G_y. Here $x_{\rm t}^{\rm fix}$ is some constant, $x_{\rm t}^{\rm fix} \in [0, 1]$, and represents the horizontal position of the blade's tip. The horizontal compression G_x is adjusted to satisfy (3.22).

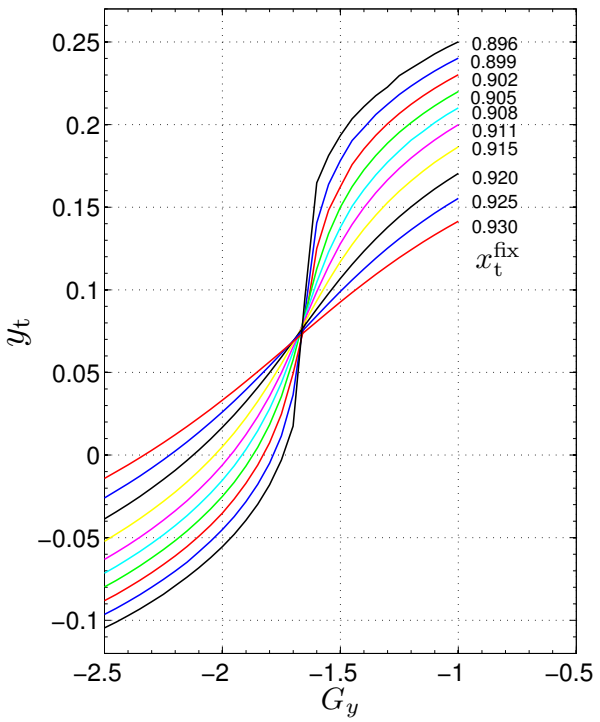

Fig. 3.18: Horizontal working points of an MGAS blade as a function of vertical force G_y. Several loci with different compression $x_{\rm t}^{\rm fix}$ are plotted.

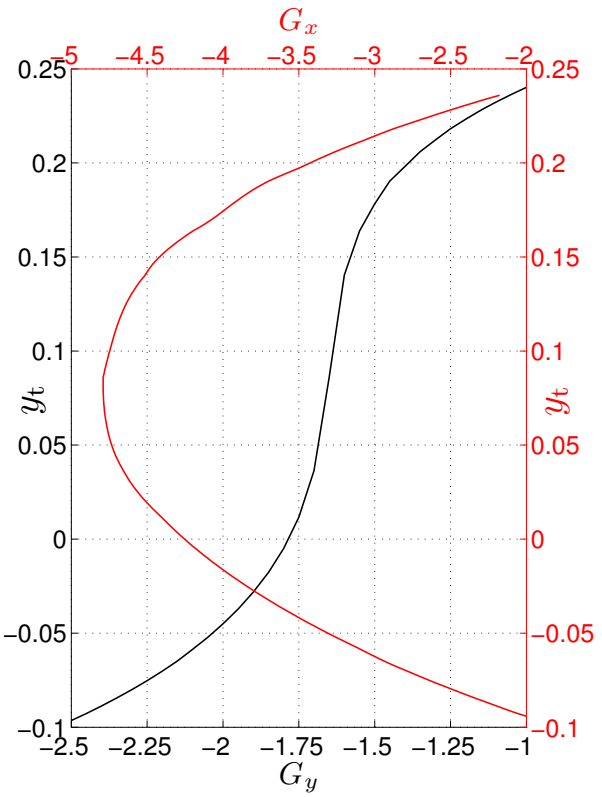

Fig. 3.19: The horizontal compression force G_x around the working point. The black curve shows the dependence of y_t on G_y when $x_t = 0.899$. The red curve shows the horizontal force G_x as a function of the working point y_t.

The result is shown in Fig. 3.18. Several loci with different $x_{\rm t}^{\rm fix}$ are drawn. In this calculation, the blade shape $\gamma(\xi)$ shown in Table 3.3 was used. The slopes of the loci

are steep around $G_y = -1.7$ and the steepness increases as $x_{\rm t}^{\rm fix}$ decreases. In this steep region, a small change of the vertical force G_y induces a large vertical movement of the equilibrium point. Therefore, the large gradient corresponds to a small vertical spring constant. Obviously, the optimum working point is the point where the gradient is largest. From the figure, it is $(G_y, x_{\rm t}^{\rm fix}) = (-1.67, 0.896)$. This is a little bit different from Fig. 5 in [34], probably because the $\gamma(\xi)$ used in [34] was different.

$x_{\rm t}^{\rm fix}$ and G_y are externally controllable parameters; $x_{\rm t}^{\rm fix}$ is determined by the distance between the base of the blade and the center of the filter. G_y is determined by the weight of the payload. Therefore, those parameters are used to tune the working point of the filter.

If the blade is further compressed beyond $x_{\rm t}^{\rm fix} < 0.896$, the locus exhibits "S" shaped folds as shown in Fig. 5 of [34]. This corresponds to the bistable state of the blade. It is difficult to draw the folded loci with the author's program for a numerical convergence problem. A more sophisticated numerical method, such as "continuation method" used in [34], is needed to follow the folded loci. However, non-folded loci are sufficient to find the optimum working point.

Fig. 3.19 shows the dependence of the horizontal force G_x on the vertical position y_t of the blade's tip when $x_t = 0.899$, along with the G_y-y_t locus. As assumed in section 3.2.3, the magnitude of G_x has a maximum at the optimum working point.

The profile (side view) of a blade under the optimum load is shown in 3.20.

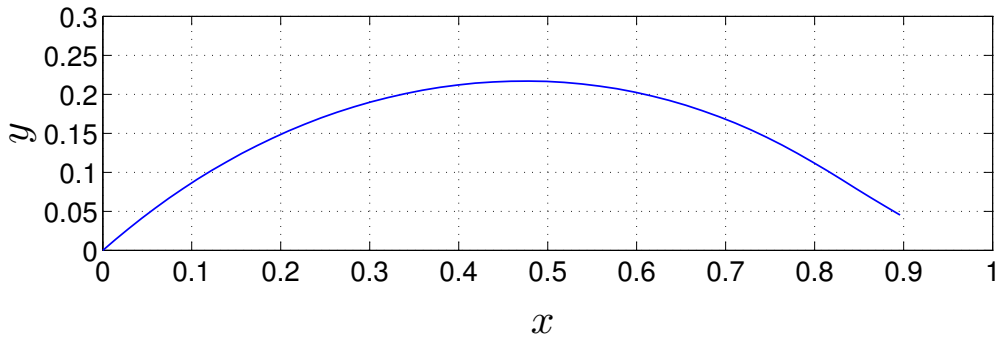

Fig. 3.20: Profile of an MGAS blade at the optimum working point.

Design Principle

As described in the previous section, the optimum working point of an MGAS filter is determined by $x_{\rm t}$ and G_y. Therefore the design goal of an MGAS filter is to adjust blade parameters and the geometry of the clamps to realize the optimum $x_{\rm t}$ and G_y. The optimum $x_{\rm t}$ is realized by setting the distance between the base and the tip of a blade to $Lx_{\rm t}$. In this way the geometry of the clamps (the distance between them) is determined.

G_y depends on several parameters,

$$G_y = \frac{12L^2}{Ed^3 w(0)} F_y. \tag{3.23}$$

Usually, the scale of the filter L and the load F_y are given as requirements for the filter. Young's modulus E is also determined once the material is chosen. Therefore, d and $w(0)$ are free parameters to be adjusted to produce the optimum value $G_y^{\rm opt} = -1.67$. In principle, any combination of d and $w(0)$ which satisfies,

$$d^3 w(0) = \frac{12L^2}{E} \frac{F_y}{G_y^{\rm opt}}, \tag{3.24}$$

can be chosen. However a practical limit on the thickness d exists regarding the maximum stress.

The dimensionless radius of curvature $r(\xi)$ of a blade can be calculated by,

$$r(\xi) = 1/\frac{d\theta(\xi)}{d\xi}. \tag{3.25}$$

The radius of curvature of a blade with a length L is given by $r(\xi)L$. The absolute value of $r(\xi)$ is plotted in Fig. 3.21 for the case of a blade under the optimum load. The minimum r is 0.54 at $\xi = 0.61$. The stress $\sigma(\xi)$ stored in a blade with a length L is then written as,

$$\sigma(\xi) = \frac{Ed}{2r(\xi)L}, \tag{3.26}$$

and the maximum stress $\sigma_{\rm max}$ is

$$\sigma_{\rm max} = \frac{Ed}{1.08L}. \tag{3.27}$$

Therefore d should be chosen to be small enough so that $\sigma_{\rm max}$ does not exceed the yielding stress of the blade material.

Practical Design Procedure

In a practical design process of an MGAS filter, it is often better to start from an existing blade rather than start from the theoretically obtained parameters, x_t and G_y. This is mainly because the catalogue value of Young's modulus has a large uncertainty, resulting in an inaccurate value of G_y. The approach using a reference blade does not explicitly use Young's modulus to calculate the parameters of a new blade. This method is only effective when the new blade is made of the same material as the reference. Also the same blade shape $\gamma(\xi)$ should be used in the new blade. If there is no existing blade made of the material to be used in the new blade, it is recommendable to make a prototype blade first, then use it as a reference.

The procedure is summarized as follows:

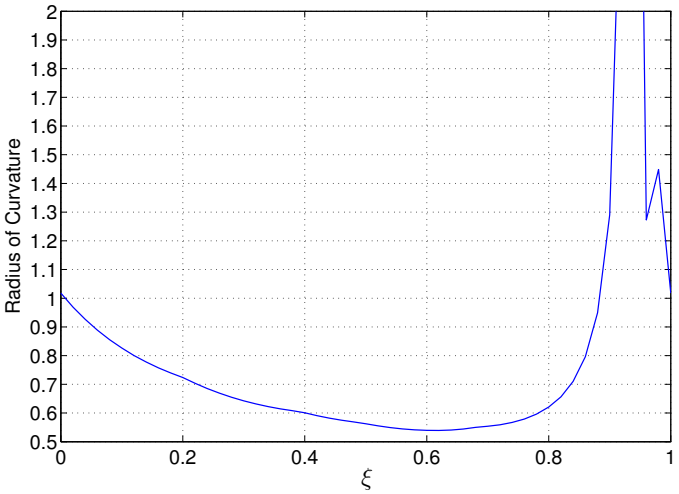

Fig. 3.21: Radius of curvature of a blade along its length.

1. Measure parameters of the reference blade. The optimum load F_y, thickness d, width $w(0)$ and length L are needed.

2. The parameters of the new blade should satisfy the following equation:

$$\frac{L_{\text{ref}}^2 F_y^{\text{ref}}}{d_{\text{ref}}^3 w_{\text{ref}}(0)} = \frac{L_{\text{new}}^2 F_y^{\text{new}}}{d_{\text{new}}^3 w_{\text{new}}(0)}. \tag{3.28}$$

   Here variables with the subscript $_{\text{ref}}$ represent the values of the reference blade and the ones with $_{\text{new}}$ are the values of the new blade.

3. Since L_{new} and F_y^{new} are given as requirements, the free parameters are d_{new} and $w_{\text{new}}(0)$ with a constraint

$$d_{\text{new}}^3 w_{\text{new}}(0) = \left(\frac{L_{\text{new}}}{L_{\text{ref}}}\right)^2 \left(\frac{F_y^{\text{new}}}{F_y^{\text{ref}}}\right) d_{\text{ref}}^3 w_{\text{ref}}(0). \tag{3.29}$$

4. Chose a set of d_{new} and $w_{\text{new}}(0)$ which satisfy the above relation.

5. Check that the maximum stress does not exceed the yielding stress using (3.27) for the chosen d_{new}.

The parameters of the reference blade used to design the blades for this experiment are listed in Table 3.2. The blade width profile $\gamma(\xi)$ is also listed in Table 3.3. The linear interpolation of the listed points is used as $\gamma(\xi)$. The blade shape is shown in Fig. 3.22. The initial angle θ_0 is 45° and the final angle θ_L is -33°. Finally, the parameters of the blades used in this experiment are listed in Table 3.4.

Length L	276 mm
Thickness d	2 mm
Width at base $w(0)$	69.2 mm
Optimum vertical load F_y	218.3 N
Material	Maraging steel

Table 3.2: Parameters of the reference blade.

ξ	$1/\gamma(\xi)$
0	1
0.198149	0.980911
0.393225	0.870803
0.490833	0.770757
0.685906	0.520354
0.929674	0.140294
0.948913	0.12017
0.956341	0.12017
0.968587	0.201242
0.979457	0.287489
0.996377	0.287489
1	0.287489

Table 3.3: Width profile of the blades used in this experiment.

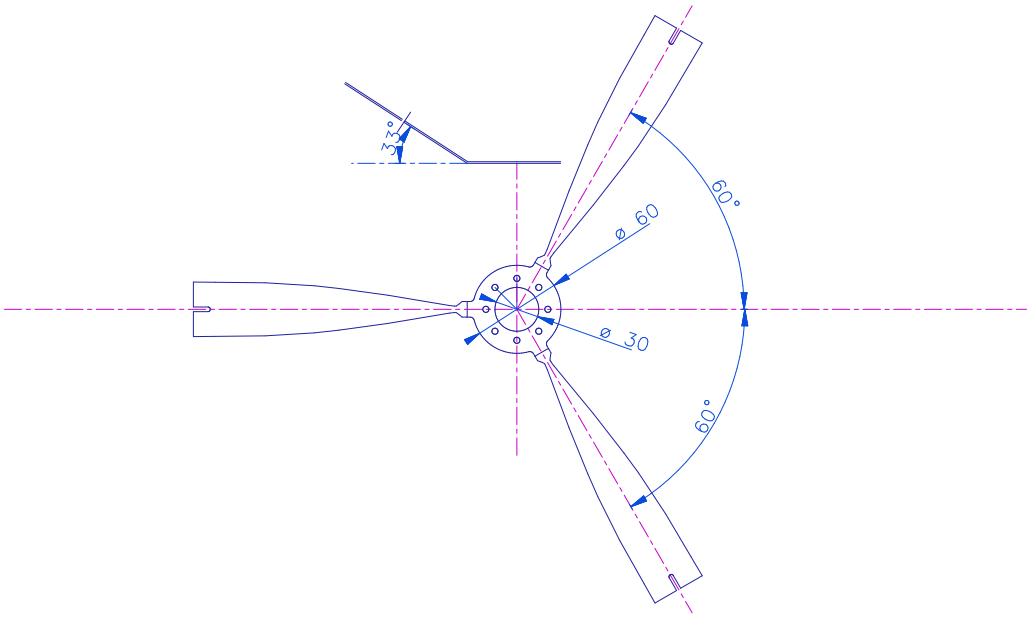

Fig. 3.22: Shape of an MGAS blade.

Parameter	Top stage MGAS filter	Damping stage MGAS filter
Blade length L	230 mm	172.5 mm
Base width $w(0)$	58 mm	37 mm
Thickness d	1.5 mm	1.1 mm
Material	Maraging steel	
Designed optimum payload	27 kg	12 kg
Actual optimum payload	29.8 kg	14.6 kg
Achieved resonant frequency f_0	$f_0 < 0.15$ Hz	$f_0 < 0.2$ Hz

Table 3.4: Parameters of the MGAS blades used in the experiment.

Tuning

Once an MGAS filter is installed to a real suspension system, it has to be tuned so that it has the desired resonant frequency. In order to tune an MGAS filter, one has to adjust the horizontal compression and the vertical load. The horizontal compression can be adjusted by changing the distance between the base and the tip of the blade (denoted by l_{BT} in Fig. 3.23). The vertical load is adjusted by adding or removing small weights to or from the suspended masses.

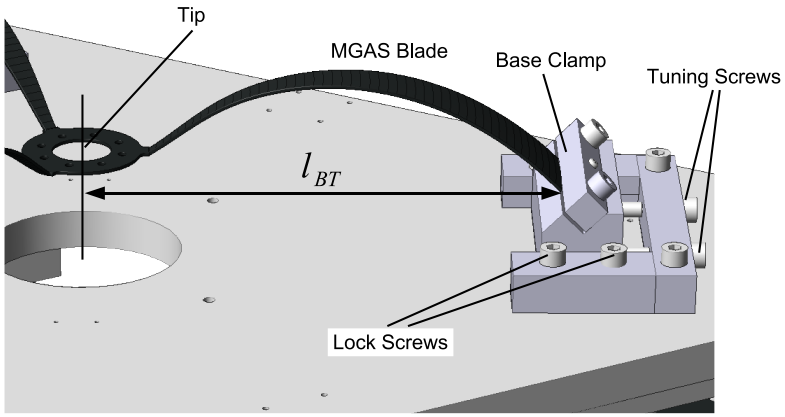

Fig. 3.23: The clamp and the tuning mechanism of an MGAS blade.

In this experiment, the MGAS blades are clamped as shown in Fig. 3.23. When the lock screws are loosed, the clamp can be moved by pushing it with the tuning screws. After the clamp is moved by a desired distance, the lock screws are fastened to fix the position of the clamp tightly.

A typical tuning procedure of an MGAS filter is summarized as follows.

1. The distance l_{BT} is set a little bit longer than the optimum distance obtained from the theoretical calculations.

2. Load the filter with a slightly lighter weight than the theoretically optimum load.
3. Measure the resonant frequency by exciting a vertical motion.
4. Slightly increase the load.
5. Iterate the step 3 and 4 until the minimum resonant frequency is found.
6. Slightly increase the horizontal compression by pushing the clamps with the tuning screws.
7. Iterate the steps from 2 to 6 until the minimum or the desired resonant frequency is achieved.

With proper tunings, vertical resonant frequencies of less than 0.2 Hz were achieved with the MGAS filters used in this experiment.

3.2.4 Top Stage

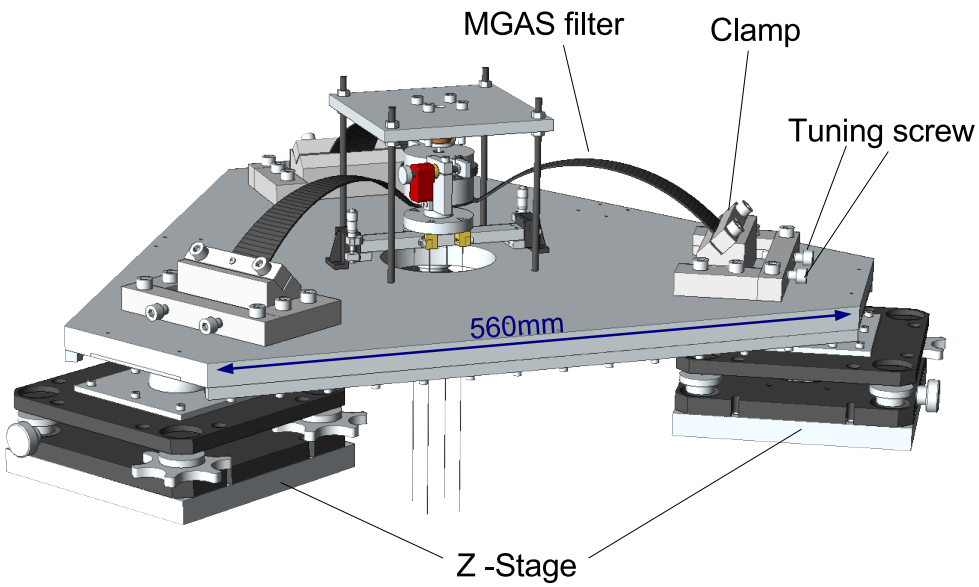

Fig. 3.24: Top stage of the suspension system.

The top stage is the starting point of the suspension chain. It is supported by three legs made of stainless steel. The top plate itself is a triangular shaped aluminum plate of thickness 20 mm. The level and tilt of the top plate can be adjusted by three z-stages supporting it. In order to make the tilt adjustment smooth, the z-stages support the top plate with spheric contacts (Fig. 3.25).

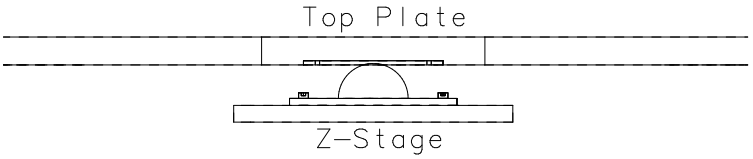

Fig. 3.25: A contact point between the z-stage and the top plate. The z-stage side is a half-sphere and the top plate side is a plate with a spheric hollow, both made of stainless steel.

On the top plate is an MGAS filter, from which the rest of the suspension stages are suspended. The bases of the blades are clamped at 45°. The horizontal compression can be adjusted by changing the distance between the clamps using the tuning screws. The filter is tuned to have a vertical resonant frequency of 0.2 Hz.

Somewhat complex structure is built on the center ring of the MGAS filter (Fig. 3.26). The stator is fixed to the blade's center ring and the wire clamps are attached to the rotator. As shown in Fig. 3.27, the stator and the rotator are connected by a thrust bearing. A Picomotor is held by the stator. The rotator is pressed to the Picomotor by a torsion coil spring. The rotator revolves as the Picomotor pushes it. In this way, the yaw orientation of the stages suspended from the rotator can be changed.

Another function of the center ring is to monitor the vertical working point of the filter. This is done by measuring the distance between the top plate and the bottom of the rotator by a photo-sensor. Since the elastic constant of the blade material changes with the temperature, the optimum load of the blades also changes, resulting in slow drift of the working point. In order to compensate the drift, the output of the photo-sensor is fed back to the coil-magnet actuator on the rotator's top at very low-frequencies (below 0.1 Hz). The feed back signal is also sent to the vertical coils of the damping mass to achieve a wider actuation range. This control is necessary to keep a low resonant frequency because it is only realized at the optimum working point[2].

The damping stage is suspended from the center ring of the top-stage MGAS filter by four 0.6 mm-thick tungsten wires. The wires are clamped between two brass blocks as illustrated in Fig. 3.28.

3.2.5 Damping Mass

The damping mass is a cylindrical structure of diameter 490 mm which contains another MGAS filter inside (Fig. 3.29). The clamps of the MGAS blades have a similar structure as the ones on the top plate. The tilt of this stage is adjusted by moving the balance weights. The total weight is adjusted so that the load to the top MGAS filter becomes optimum. The weight of the damping mass is about 15 kg. Neodymium magnets for the eddy current

[2]The optimum working point is determined only geometrically. Therefore, the change of the elastic constant with the temperature does not change the height of the optimum working point. This is the reason why keeping the height of the blade's tip is essential.

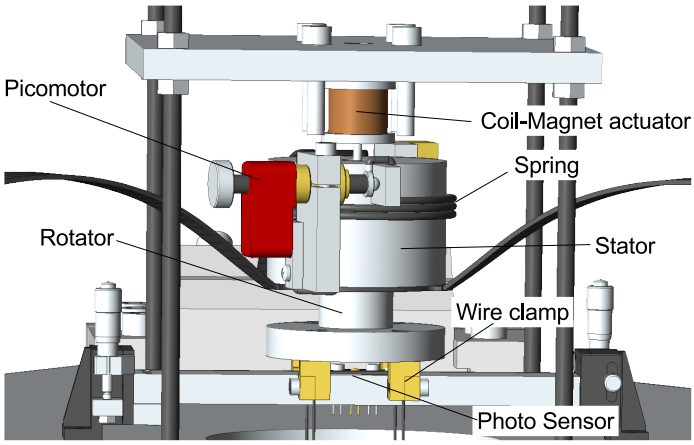

Fig. 3.26: The center ring of the top-stage MGAS filter. The yaw orientation of the payload can be changed by the Picomotor. The photo sensor monitors the vertical position of the center ring and the coil-magnet actuator is used to compensate the drift of the working point.

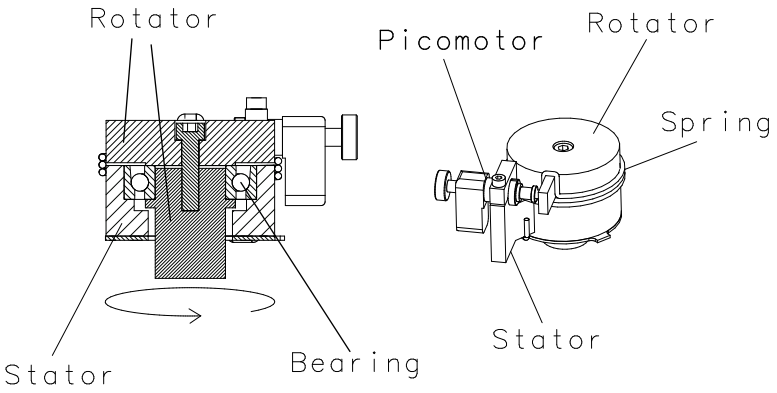

Fig. 3.27: The internal structure of the rotator and the stator. A thrust bearing is used to connect them.

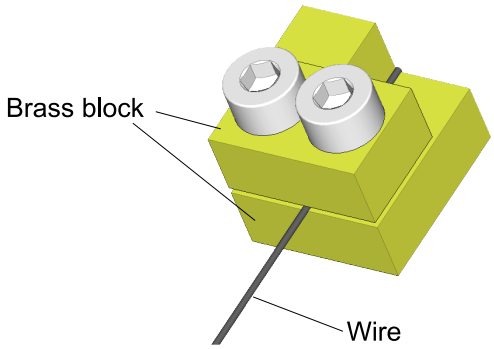

Fig. 3.28: A wire clamp on the top stage. Similar clamps are used in the other parts of the suspension.

damping are attached to the outer shell of the damping mass.

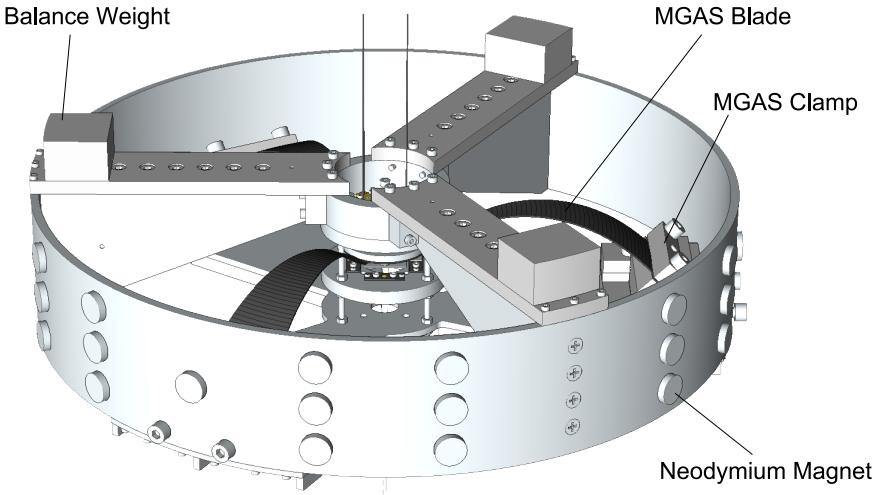

Fig. 3.29: Damping mass

Below the center ring of the MGAS filter, photo-sensors are installed to monitor the vertical working point of the blade (Fig. 3.30). Here four photo-sensors are placed around a hole in the center instead of having one sensor at the center. This is because the suspension system was originally designed to include a vertical suspension point interferometer (VSPI), an active "vertical" vibration isolation device. The hole is designed to be used to introduce a laser beam through it for the VSPI. However, the VSPI has not implemented in this experiment because sufficient vertical vibration isolation was provided by the two MGAS filters. Therefore, a center plate of the MGAS filter which has no hole at the center is used now. When the VSPI is installed, the center plate should be replaced by a plate with a

center hole. The idea and the results of a prototype experiment on VSPI are presented in Appendix D.

The four sensors are connected in parallel to work as a single vertical position sensor. The reflector plates are polished aluminum plates, which is used to reflect the light from the sensors effectively.

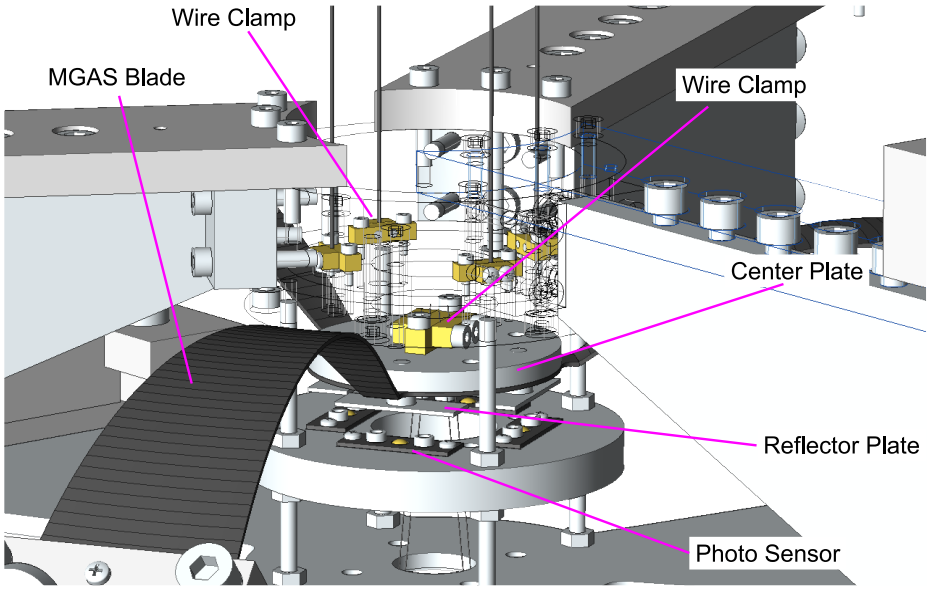

Fig. 3.30: Central part the damping mass.

When the damping mass is installed to the system, it is surrounded by a cylindrical copper plate, called damping plate. When the damping mass moves, eddy current is induced on the damping plate by the magnetic field of the neodymium magnets on the damping mass. This current is eventually dissipated as Joule heat. In this way the vibration of the damping mass is damped. The damping plate is supported from the top stage through three rods and blade springs made of phosphor bronze.

The damping mass is equipped with coil-magnet actuators in three degrees of freedom, vertical, horizontal and yaw actuators. As described in the previous section, the vertical coils are used to compensate the drift of the top-stage MGAS filter's working point. The other two actuators are used to measure the transfer functions of the suspension system for characterization.

3.2.6 SPI Mirror

Below the damping stage is a mirror for the SPI (Fig. 3.32). A cylindrical dielectric mirror of diameter 1 inch and the thickness 6 mm, manufactured by CVI, is used. The substrate of the mirror is BK7. The mirror is attached to an "H" shaped brass block with an adhesive, Araldite. The block is called "SPI mass" from now on.

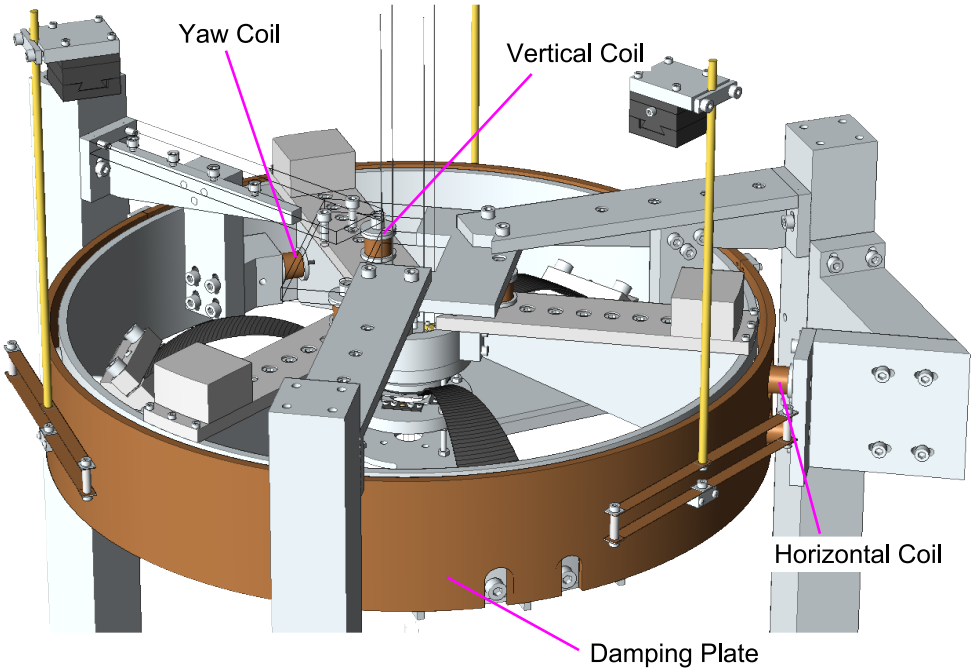

Fig. 3.31: Installed state of the damping stage. The damping mass is surrounded by a copper cylinder (damping plate) for eddy current consumption.

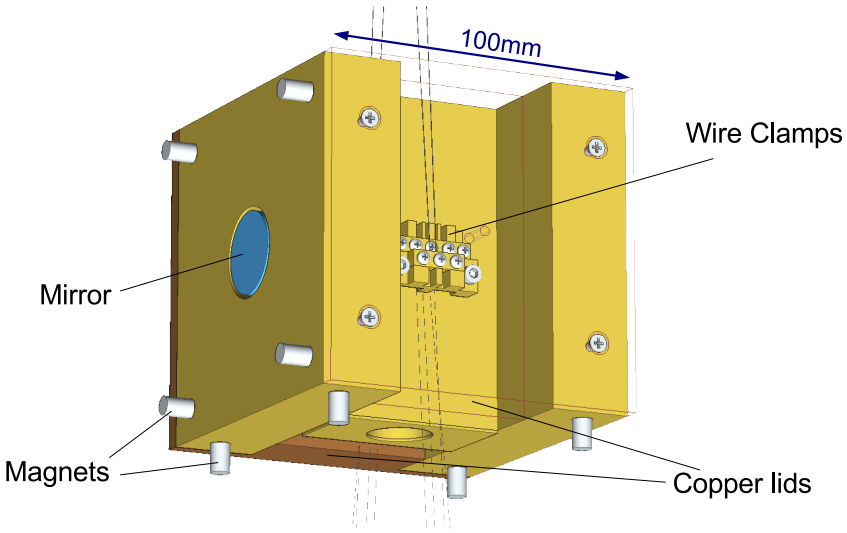

Fig. 3.32: The SPI mass.

To suspend the SPI mass, 0.4 mm thick tungsten wires are used. The wires are clamped at the same level as the center of gravity of the mass, in order to reduce the coupling between the horizontal and pitch motion. From the SPI mass, the mirror of the MIF and the recoil mass are suspended. The suspension wires for those masses are also clamped at the level of the center of gravity. The clamping mechanism is similar to the top-stage clamps shown in Fig. 3.28; the wire is sandwiched between the surfaces of brass blocks.

Copper lids are attached to the SPI mass to achieve low-frequency rotational resonances by increasing the moment of inertia. The lids are also used to adjust the weight of the SPI mass to achieve the optimum load for the damping-stage MGAS filter. The lids are made a little bit heavier than it should be and milled down afterwards to an appropriate weight. The total weight of the SPI mass is about 7.5 kg.

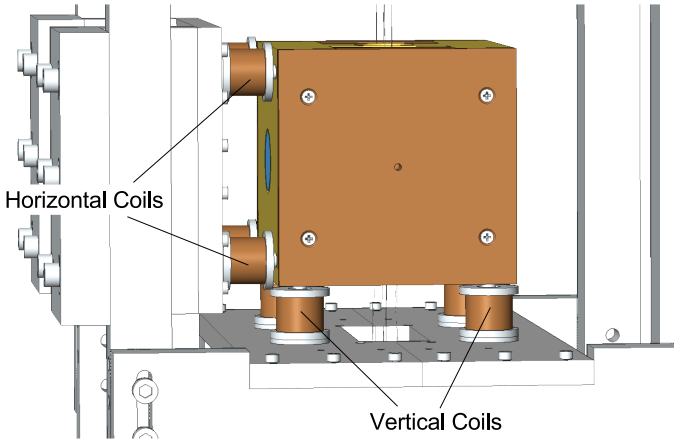

Fig. 3.33: Coil-magnet actuators of the SPI mass.

On the front and the bottom surface of the SPI mass, bar shaped neodymium-magnets are attached four on each surface (Fig. 3.33). Those magnets combined with coils form coil-magnet actuators. The horizontal actuators are used to control the length of the SPI. The vertical actuators are used to keep the working point of the damping-stage MGAS filter. By differentially exciting those actuators, the orientation of the SPI mirror can be also controlled.

3.2.7 Main Mirror and Recoil Mass

The last stage of the suspension system consists of a mirror for the MIF and a recoil mass surrounding it (Fig. 3.34). The mirrors of the MIF are of the same type as the SPI mirrors. It is attached to an cylindrical aluminum mass of the diameter 100 mm and the thickness 90 mm with Araldite. The cylinder, which is called "MIF mass" here after, is suspended by two loops of 0.15 mm thick tungsten wires. The wires are fit in two grooves to keep them in proper positions. Stand-offs are used to make sure that the wires come off the cylinder at the level of the center of gravity (Fig. 3.35).

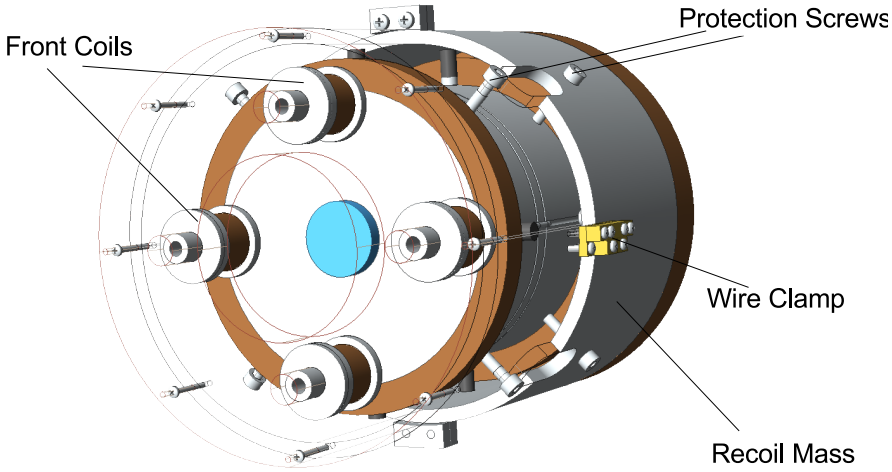

Fig. 3.34: The MIF mirror and the recoil mass.

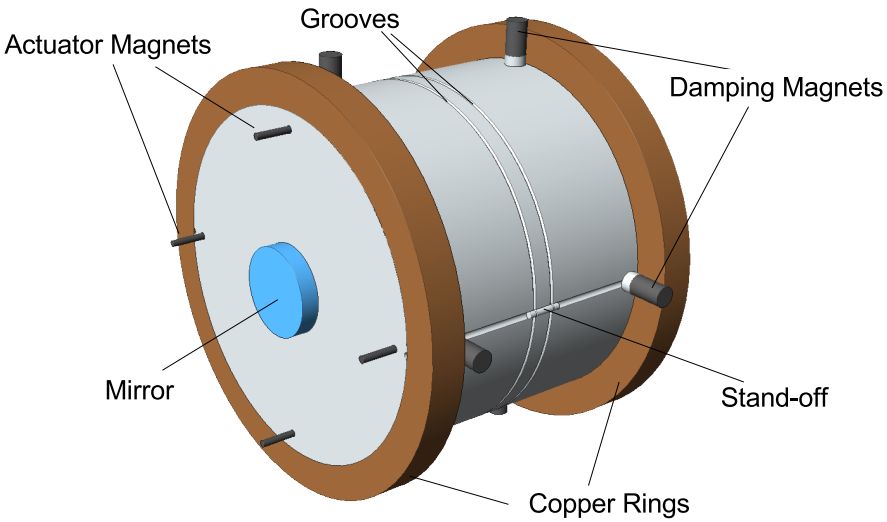

Fig. 3.35: MIF mass.

The copper rings are attached to increase the moment of inertia; those were added afterwards when the pitch resonant frequency of the MIF was found to be too high and the coupling from the pitch motion was identified as the dominant noise source of the interferometer.

The thick neodymium magnets are used to produce eddy current damping between the MIF mass and the recoil mass. This is effective to damp the differential motion of the two masses, which does not recoil to the damping mass so much and tends to have a high quality factor resonance. However, this scheme cannot be used in large interferometers because the eddy current damping introduces significant amount of thermal noise to the interferometer. Other schemes, such as an active damping system, should be used to tame the differential motion in the future interferometers.

The recoil mass is a hollow cylinder made of aluminum and copper. The purpose of the recoil mass is to serve as a quiet stage to hold the coils used for the actuation of the MIF mass. If a coil is rigidly supported from the ground, it vibrates as much as the ground vibrates. This vibration is transmitted to the MIF mass through small non-uniformity of the magnetic field inside the coil. This effect should be eliminated because any vibration directly introduced to the MIF cannot be suppressed by the SPI. Since the recoil mass receives the same vibration isolation as the MIF mass, it is an ideal platform for quietly holding the coils.

Coil magnet actuators are placed both on the front and back surfaces of the MIF mass. The front actuators are used to actuate the mass horizontally. The choice of the front actuators is made to achieve a wider bandwidth for the length control of the MIF. Usually, the bandwidth of this control loop is limited by the resonances of the mass itself. Therefore, higher resonant frequencies are preferable to achieve a wider control bandwidth. The resonances which cause problems to the control system are modes which have nodes between the actuation points and the beam spot on the mirror; the phase of the motion at the beam spot delays from that of the actuation points by more than 180° at frequencies above this kind of resonances. Therefore, the resonant frequencies of the problematic resonances can be made higher by making the distance between the actuation points and the beam spot shorter. This is why the front actuators are better than the back actuators.

In order to reduce the actuator noise, the front actuators are made so weak that they are just enough to lock the interferometer. In contrast, the back actuators are stronger than the front ones and used only to rotate the mirror. For this purpose, the back actuators are connected so that they can be excited only differentially (Fig. 3.36). If the actuators are perfectly balanced, the differential excitation of them does not cause any horizontal motion in principle. However, in reality some coupling from the differential actuation to the horizontal displacement exists. Assuming that the coupling is of the order of a few percent, the back actuators are made 8 times stronger than the front ones.

The protection screws are used to confine the motion of the MIF mass inside the recoil mass so that the actuator magnets do not touch the inner walls of the coils to avoid them from coming off (Fig. 3.34). Since we have many earthquakes in Japan, this precaution is absolutely necessary; otherwise, the magnets will not survive for a month.

The parameters of the suspension stages are summarized in Table 3.5. The pitch and

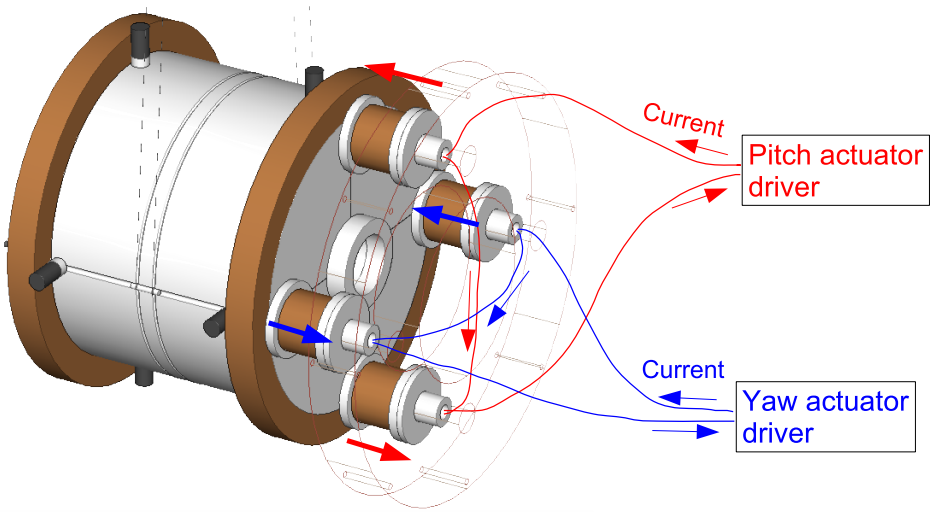

Fig. 3.36: Back actuators of the MIF mass. A pair of coils makes up a rotational actuator. Two coils are wired in series with opposite polarity so that they exert forces differentially. The forces are represented by thick arrows in the figure.

yaw resonant frequencies were measured by an optical-lever.

Parameter	Damping mass	SPI mass	MIF mass	Recoil mass
Weight [kg]	15	7.5	2.5	4.7
Pitch moment of inertia [kg · m^2]	0.3	1.4×10^{-2}	3.8×10^{-2}	9.0×10^{-3}
Yaw moment of inertia [kg · m^2]	0.6	1.9×10^{-2}	3.8×10^{-2}	9.0×10^{-3}
Horizontal resonances [Hz]	0.6	0.8	1.15	2.15
Pitch resonances [Hz]		1.3	1.9	2.5
Yaw resonances [Hz]		0.21	0.5	0.8

Table 3.5: Parameters of the suspension stages.

3.3 Vacuum System

The three interferometers, the MC, the MIF and the SPI, are all installed inside vacuum chambers. As shown in Fig. 3.38, three vacuum tanks connected in series are used. The first tank, which is used to house the MC, was originally built for a 3 m Fabry-Perot-Michelson interferometer [35]. The other two tanks are newly built for this experiment. Inner surfaces of the new tanks are polished with electrochemical buffing (ECB) technique by Ultra Finish Technology. ECB is a surface processing method that can reduce the surface roughness to sub-micron order. With this treatment, the out-gas from the surfaces of the chambers can

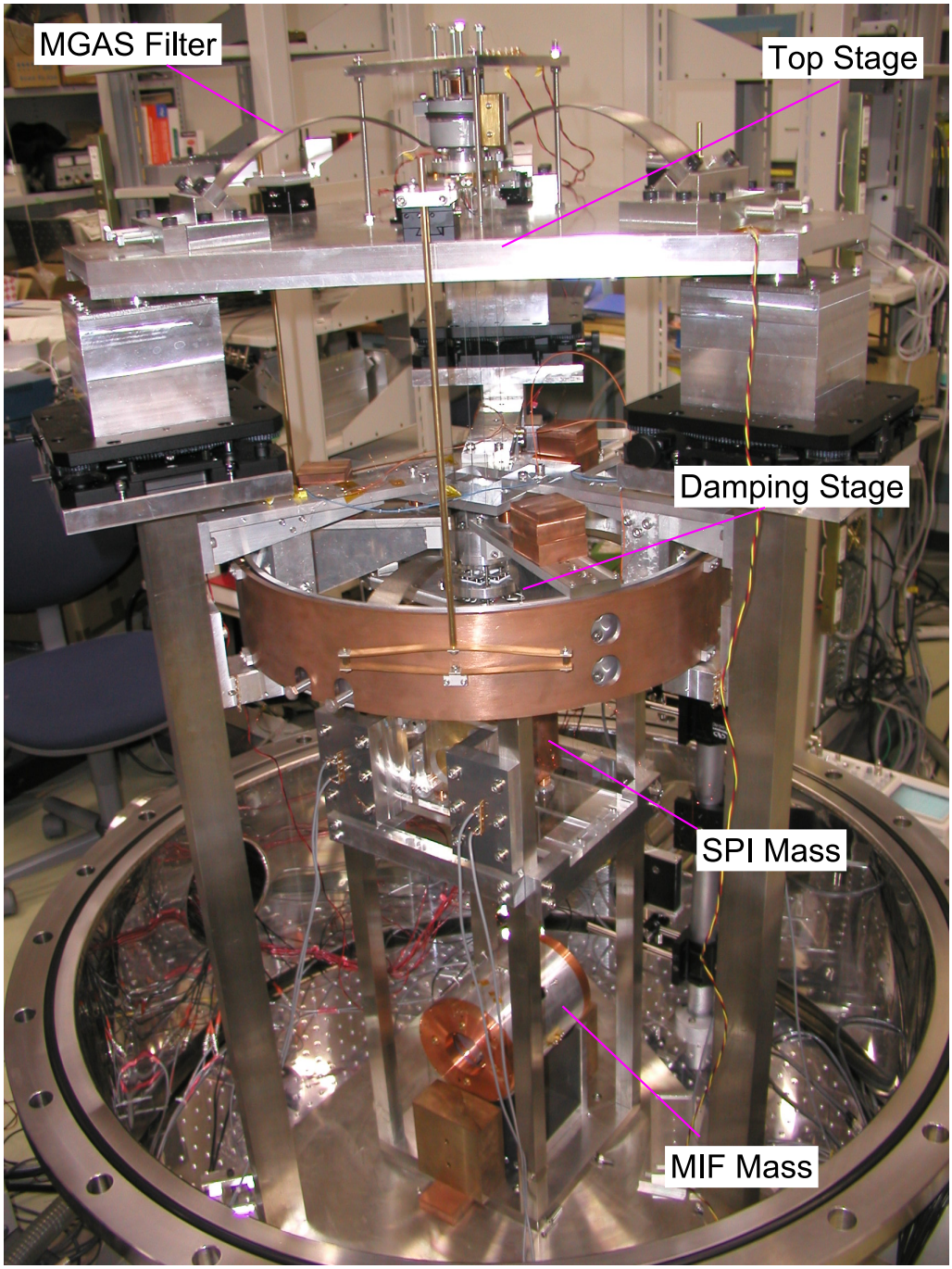

Fig. 3.37: A picture of the suspension system (End tower).

be significantly reduced [36].

A combination of a turbo-molecular pump and a scroll pump is used to draw a vacuum. The turbo-pump is Osaka Vacuum TG800FVAB-60 and the scroll pump is Mitsubishi Electronics VP-SW-A 620. Since not much attention was paid regarding the handling and the material selection of the objects installed to the chambers, the achieved vacuum was about 10^{-5} Torr, which is not particularly good considering the potential of the pumps and the polished chambers. However, this is sufficient to eliminate the air fluctuation and sound noise in this experiment.

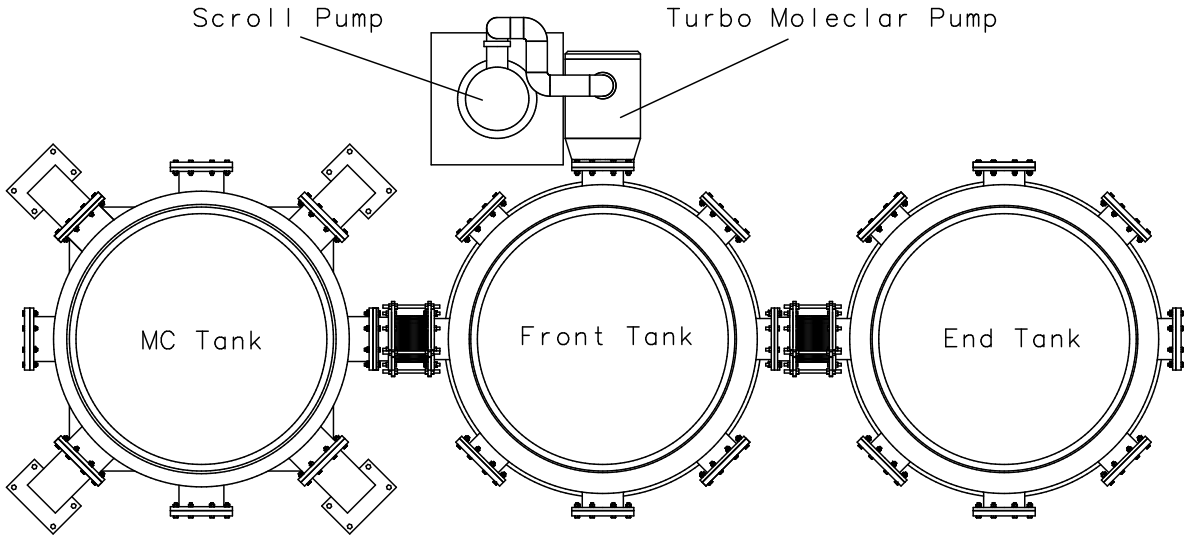

Fig. 3.38: The vacuum system.

3.4 Operation of the Interferometers

3.4.1 Control System

During the operation of the interferometers, there are 8 servo loops: laser intensity and frequency stabilization, 4 loops of MGAS filter's working point stabilization, and the length control loops of the MIF and the SPI (Fig. 3.39). In this section, those control loops are described in this order.

Intensity Stabilization

As described in section 3.1.1, a fraction of the laser light is picked up by a PBS before the mode cleaner. The picked-up power is about 5 mW. It is received by a photo detector and the output of the photo detector is compared with a reference voltage produced from an AD587, a precision 10V reference IC. The difference between them is fed back to the laser-diode's current driver through a feedback filter. Fig. 3.40 shows the frequency response of

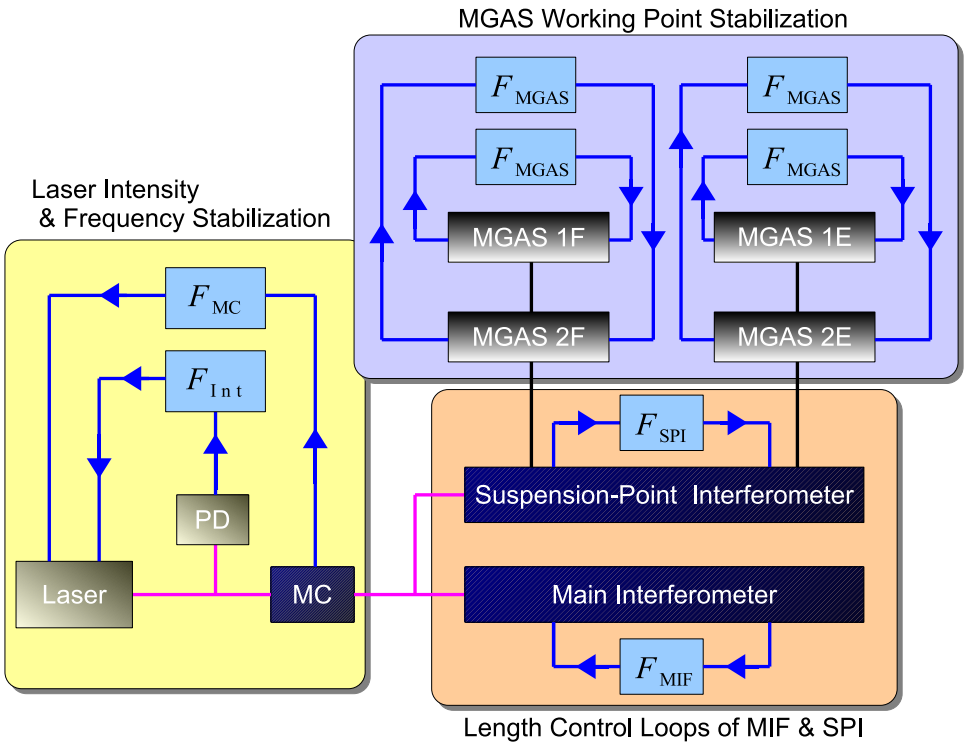

Fig. 3.39: Control loops in this experiment. The pink lines represent laser beams. The black lines represent suspension wires. The blue lines represent the signal flow of the control loops. F_{MC} is the frequency stabilization filter. F_{Int} is the intensity stabilization filter. F_{MGAS} is the servo filter for the working point stabilization of the MGAS filters. F_{MIF} and F_{SPI} are the length control filters for the MIF and the SPI, respectively.

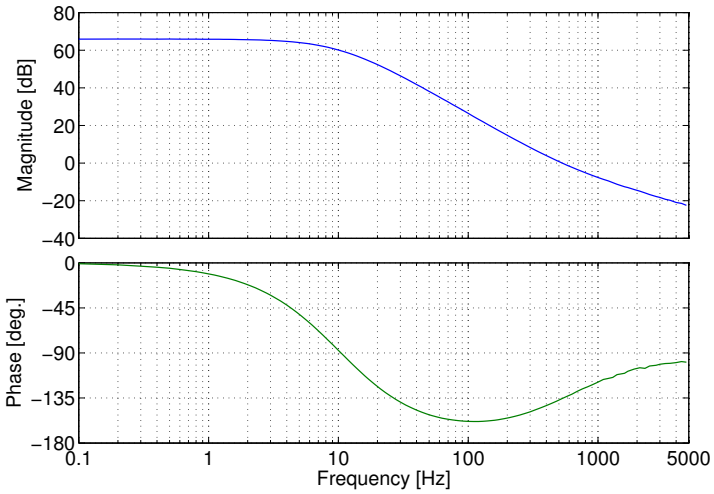

Fig. 3.40: Frequency response of the feedback filter for the intensity stabilization servo.

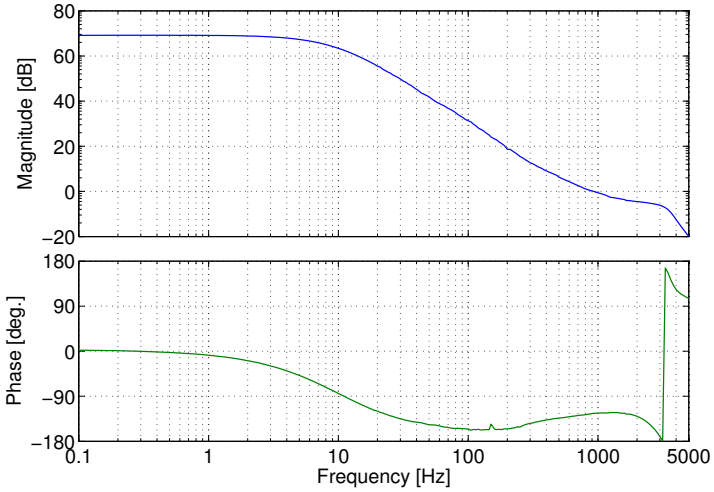

Fig. 3.41: Open-loop transfer function of the intensity stabilization servo.

the feedback filter, which is basically a 2nd order low-pass filter of 10 Hz. A 600 Hz high-pass filter is inserted to compensate the phase lag around 1 kHz. The open-loop transfer function of the intensity stabilization servo is shown in Fig. 3.41. The unity gain frequency of the servo is 1 kHz. It is mainly determined by the bandwidth of the diode current control, which is limited to 5 kHz inside the laser driver.

The relative intensity noise (RIN) of the reflected light from the MC, measured by PD2, is shown in Fig. 3.42. During this measurement, the laser is not resonated to the MC, i.e. the input mirror of the MC just works as a high reflectivity mirror. The intensity noise suppression of about a factor of 10 is achieved by the intensity stabilization servo. Between 20 and 60 Hz, there are several large peaks in the spectra. Though the origins of those peaks have not yet determined, those peaks are likely to be the mechanical resonances of the support structures of the MC, the steering mirrors or the PD. For reference, the spectra of the error signal, the output of PD1, are shown in Fig. 3.43.

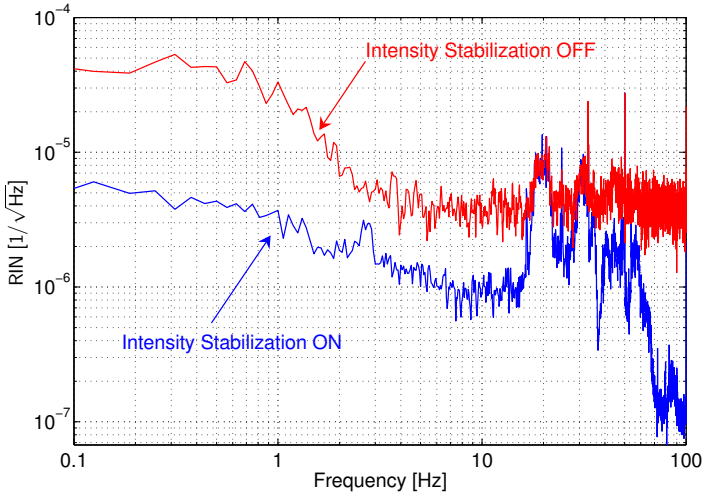

Fig. 3.42: Relative intensity noise spectra of the light reflected from the MC. The intensity noises with and without the intensity stabilization are compared. During the measurements, the laser was not resonated to the MC.

Frequency Stabilization

The laser frequency stabilization is realized by locking the frequency to the mode cleaner by the PDH scheme. The block diagram of the laser frequency stabilization loops is shown in Fig. 3.44. The servo system is a two-loop control system. The fast and fine control is performed by the PZT frequency tuning of the laser. In order to compensate for slow and large frequency drift of the laser, wider range frequency tuning through the temperature control of the laser crystal is used at low frequencies. In Fig. 3.44, M is the transfer function of the MC from the laser frequency variation to the output of the MC (PDH signal). F_{P} and

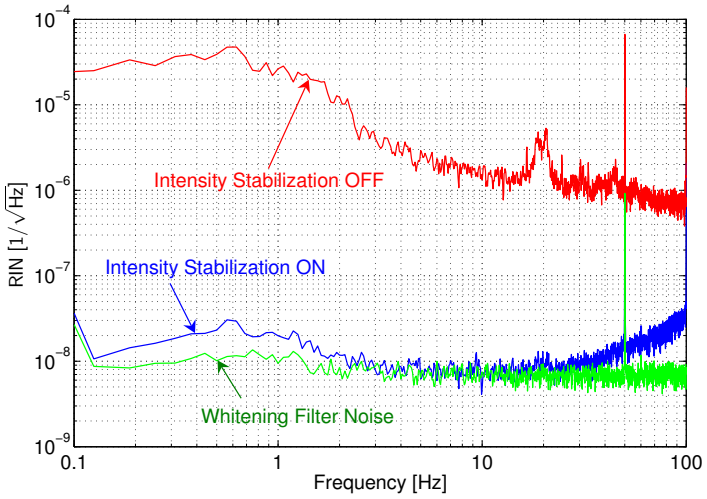

Fig. 3.43: Noise spectra of the error signal of the intensity stabilization servo.

F_{T} are the servo filters for the PZT and the temperature control. L_{P} and L_{T} represents the response of the laser to the PZT and temperature control signal, i.e. the transfer functions from the input voltage to those control terminals to the corresponding frequency changes. f_{noise} denotes the original frequency fluctuation of the laser to be suppressed.

The frequency response of the PZT filter (F_{P}) is plotted in Fig. 3.45. To analyze the stability of the PZT loop, the open-loop transfer function was measured by injecting signal p_{i} and observing p_2/p_1. This measurement gives,

$$\frac{p_2}{p_1} = -\frac{G_{\mathrm{P}}}{1+G_{\mathrm{T}}}, \tag{3.30}$$

where $G_{\mathrm{P}} \equiv ML_{\mathrm{P}}F_{\mathrm{P}}$ is the loop gain of the PZT control without the temperature control, and $G_{\mathrm{T}} \equiv ML_{\mathrm{T}}F_{\mathrm{T}}$ is the temperature control's loop gain without the PZT control. $G_{\mathrm{P}}/(1+G_{\mathrm{T}})$ is plotted in Fig. 3.46. This loop has two unity gain frequencies (UGFs) at 70 mHz and 23 kHz. The phase margin at the lower UGF is 70° and at the upper UGF it is 25°. The lower UGF corresponds to the frequency where $G_{\mathrm{P}} = G_{\mathrm{T}}$ and below this frequency the temperature control plays the dominant role.

The transfer function of the servo filter for the temperature control (F_{T}) is shown in Fig. 3.47. As in the case of the PZT loop, the open-loop transfer function was measured by injecting signal t_{i} and observing t_2/t_1. In this measurement

$$\frac{t_2}{t_1} = -\frac{G_{\mathrm{T}}}{1+G_{\mathrm{P}}}. \tag{3.31}$$

The result is plotted in Fig. 3.48. The UGF of the temperature control loop is 70 mHz, which is the same as the lower UGF of the PZT loop, and the phase margin there is 70°.

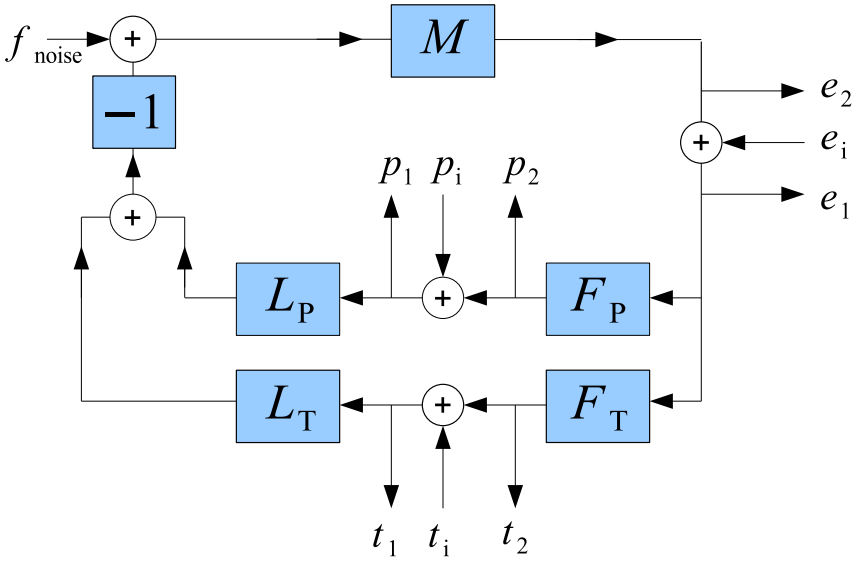

Fig. 3.44: The block diagram of the MC control loop. M is the transfer function from the laser frequency variation to the output of the MC. F_{P} and F_{T} are servo filters for the PZT loop and the temperature loop respectively. L_{P} and L_{T} are the laser's response to the PZT and temperature control.

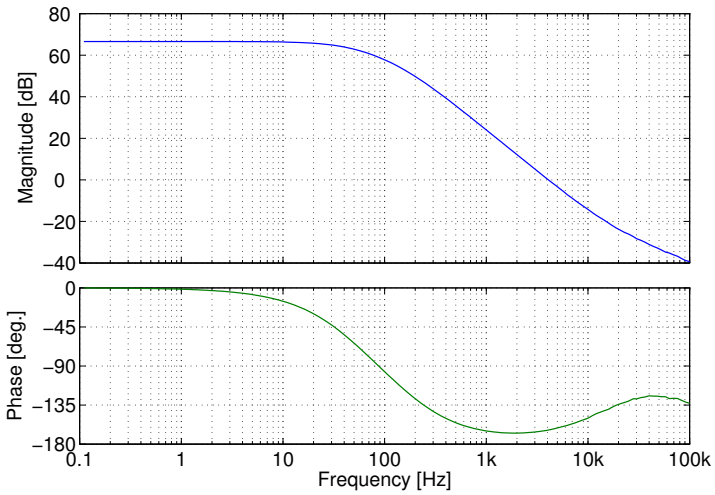

Fig. 3.45: Frequency response of the PZT loop filter

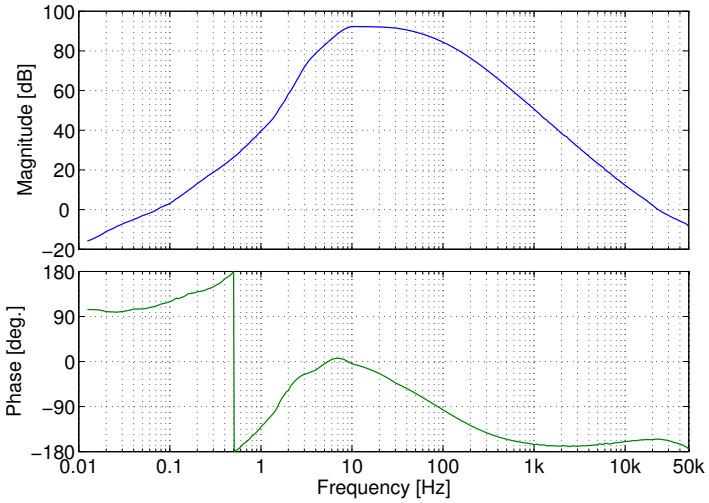

Fig. 3.46: Bode plot of the open-loop transfer function of the PZT control loop, $G_{\mathrm{P}}/(1+G_{\mathrm{T}})$.

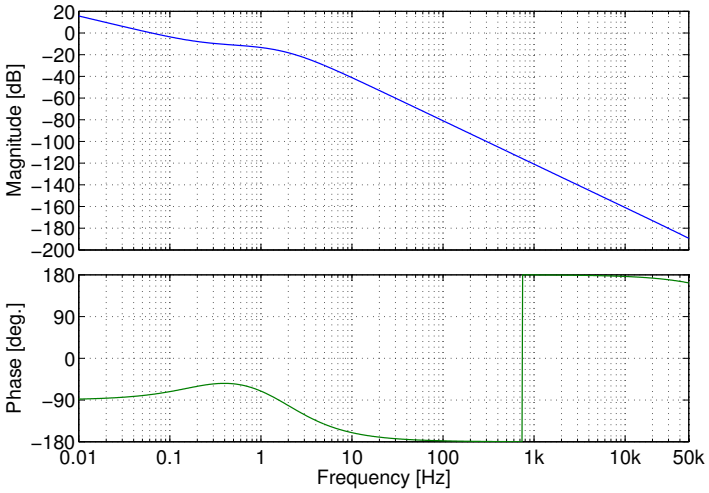

Fig. 3.47: Frequency response of F_{T}, the servo filter for the temperature control.

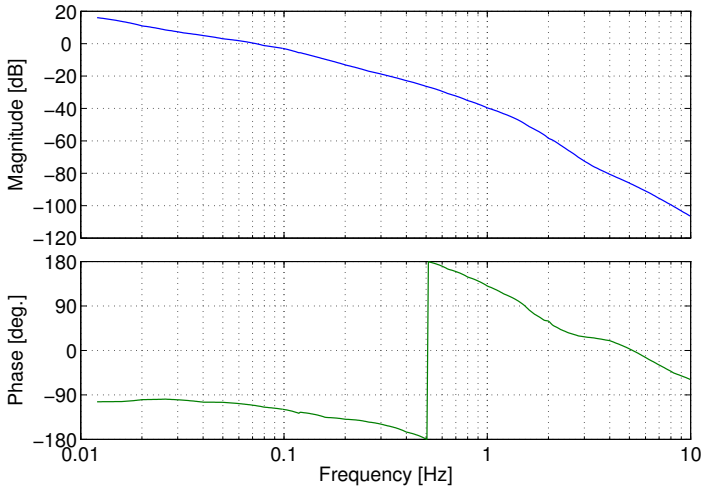

Fig. 3.48: Open-loop transfer function of the temperature loop, $G_{\mathrm{T}}/(1+G_{\mathrm{P}})$.

Finally, the overall loop gain of the frequency stabilization servo is given by $G_{\mathrm{P}}+G_{\mathrm{T}}$. It was obtained by injecting signal e_{i} and measuring e_2/e_1. Fig. 3.49 shows the result. The control bandwidth is 23 kHz and the gain at the frequencies of interest (0.1-10 Hz) is more than 90 dB.

Using the mode cleaner, the amount of the free-run laser frequency fluctuation was measured (the blue curve in Fig. 3.50). This spectrum was estimated from the feedback signal of the frequency stabilization servo. From the error signal, the stabilized frequency noise spectrum was obtained (the red curve). However, this is an error signal evaluation; it only states the minimum level of the frequency noise potentially achievable with the stabilization system. In reality the frequency noise may be larger than this.

The green curve in Fig. 3.50 shows the estimated detector noise of the MC. This was obtained by the following way. First, the noise of the photo detector was measured after the demodulator. During the measurement, the MC was not locked. Then the noise is multiplied with the gain of the feedback circuits, $(L_{\mathrm{P}}F_{\mathrm{P}}+L_{\mathrm{T}}F_{\mathrm{T}})$, and divided by the total loop gain $(G_{\mathrm{P}}+G_{\mathrm{T}})$ to estimate the contribution of the detector noise to the frequency noise. The shot noise is included in this noise.

Since the laser frequency is stabilized using the cavity length as a reference, the fluctuation of the MC cavity length induces the fluctuation of the "stabilized" frequency. The reported stability of a rigid cavity with a similar size is about $20/f$ Hz/$\sqrt{\mathrm{Hz}}$ [37]. The $20/f$ line is drawn as a brown curve in Fig. 3.50. Since the reference cavities used in [37] are suspended to isolate them from the seismic vibration, the MC cavity in this experiment, which is not suspended, may be noisier.

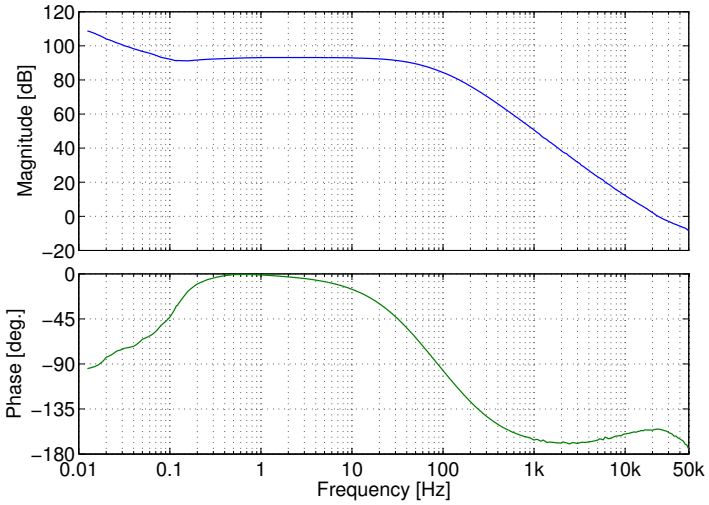

Fig. 3.49: Overall loop gain of the frequency stabilization servo, $G_{\mathrm{P}} + G_{\mathrm{T}}$.

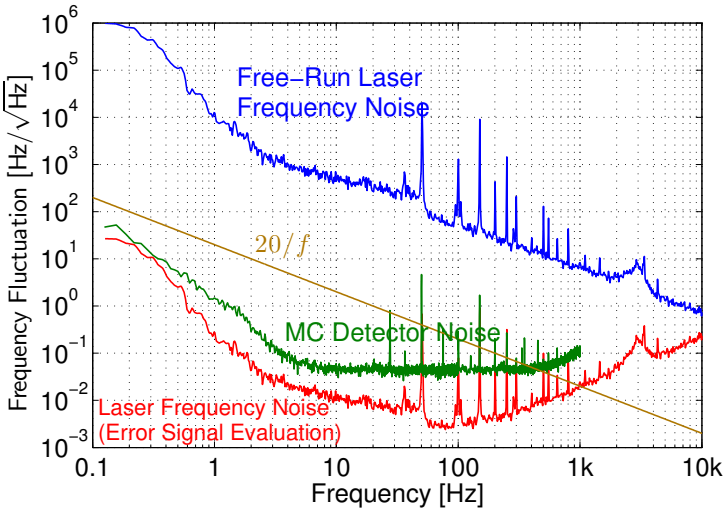

Fig. 3.50: Laser frequency noises.

MGAS Filter Working Point Stabilization

Temperature dependence of the elastic constant of the MGAS filter's material induces considerable amount of the drift of its working point, i.e. the vertical position of its tip is shifted. This drift causes both the detuning of the filter, which increases its vertical resonant frequency, and mis-alignment of the interferometers' mirrors to the incident beams. Therefore, the drift should be compensated in some way.

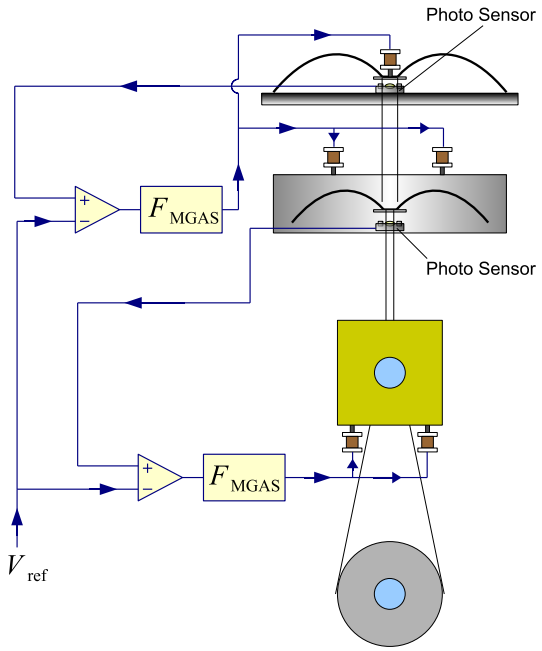

Fig. 3.51: Control loops of the MGAS filter working point stabilization.

In this experiment, the drift was cancelled by a feedback control. As described in section 3.2.4 and 3.2.5, the vertical positions of the tips of the MGAS blades are monitored by photo-sensors (Fig. 3.51). The output of a photo-sensor is compared with a reference voltage $V_{\rm ref}$ by a differential amplifier. The output of the differential amplifier is filtered by a complete integrator $F_{\rm MGAS}$ to extract only the near DC signal. Then the filtered signal is fed back to the vertical coils to keep the working point of the MGAS filter. The bandwidth of the control is limited well below 0.1 Hz.

Fig. 3.52 shows the variation of the MGAS filters' working point over 30 hours. For the purpose of comparison, the working point stabilization of the front tower was turned off, whereas that of the end tower was turned on. Obviously the working point of the front tower MGAS filters changed with the temperature drift. In the end tower, the temperature variation was compensated by the feedback voltages shown below.

The conversion coefficient from the output voltage of the sensors to the vertical position

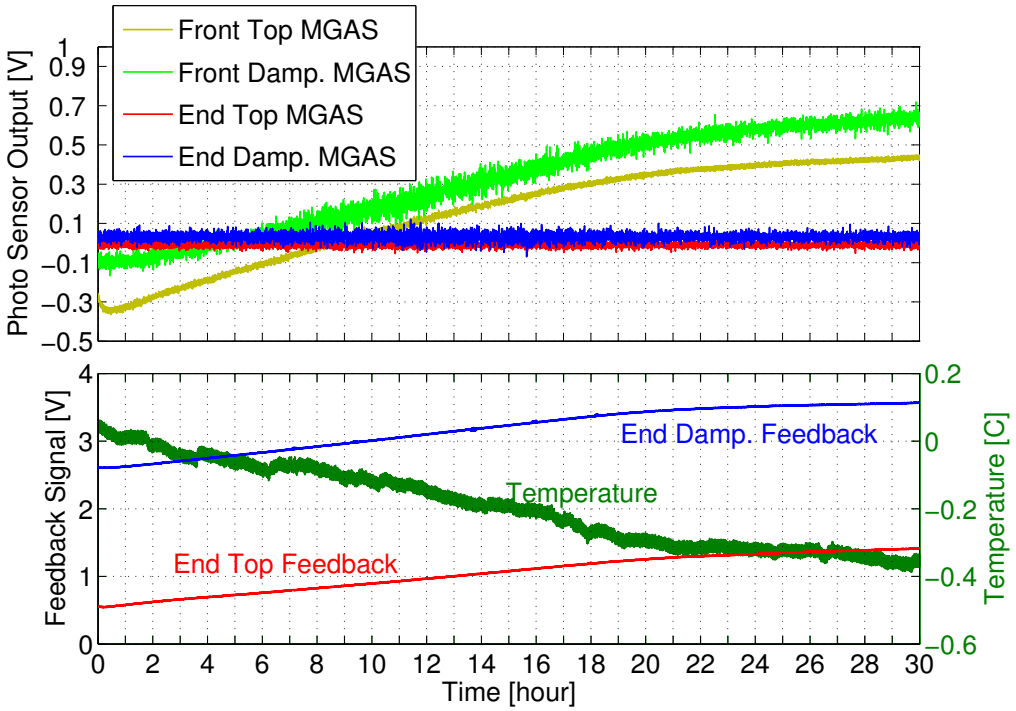

Fig. 3.52: 30 hours trend of the MGAS filters' working point variation. The working point stabilization servo is turned on in the end tower and off in the front tower. The outputs of the photo-sensors roughly correspond to $5 \times 10^{-4}\,\mathrm{m/V}$. The lower graph shows the feedback voltages and the temperature deviation from 25 C°.

of the blades is roughly[3] 0.5 mm/V. Without the stabilization, the working point moves about 1 mm/C° . When stabilized, the variation of the working point is reduced to less than 25 μm.

Length Control of the MIF and the SPI

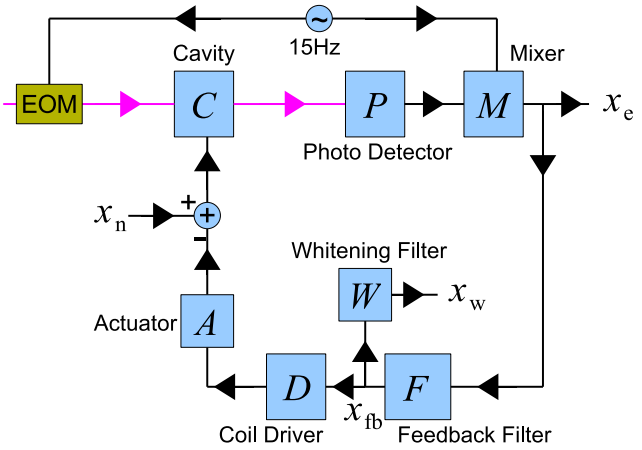

Fig. 3.53: The block diagram of the length control servo. C: The transfer function of the cavity from the displacement to the amplitude of the 15 MHz light power modulation. P: The detection gain of the photo detector at 15 MHz. M: Gain of the mixer. F: The transfer function of the feedback filter. D: The coil driver's transfer function. A: The transfer function from the output of the coil driver to the actual mirror displacement. W: The transfer function of the whitening filter. x_n is the displacement noise. x_e is the error signal. x_{fb} is the feedback signal. x_w is the output of the whitening filter.

The lengths of the MIF and the SPI have to be controlled to keep the interferometers in resonance. The error signals are obtained by the Pound-Drever-Hall method with 15 MHz phase modulation. Through a feedback filter, the error signal is fed back to the horizontal coil-magnet actuators of the mirrors (Fig. 3.53). In this experiment, the feedback signal is sent to both the front and the end mirrors. However, feedback to only one of those mirrors also works fine. The unity gain frequency (UGF) of the loops are both about 1 kHz.

The frequency responses of the feedback filters are shown in Fig. 3.54. At low-frequencies, below 10 Hz, a lag-lead filter is inserted to increase the DC gain. To recover the phase delay around the UGF, a first order high-pass filter with cut-off frequency of 500 Hz is used. In the SPI filter, a band-elimination filter is inserted at 3 kHz to remove the resonance of the SPI mass at this frequency and achieve a wider control bandwidth.

The open-loop transfer functions of the servo loops are shown in Fig. 3.55. At the frequency region of interest, i.e. below 10 Hz, the control gain is more than 80 dB for both

[3]The linearity of the sensors is not so good when the variation of the working point is large. This is the reason why the vertical positions are indicated by the raw output voltage.

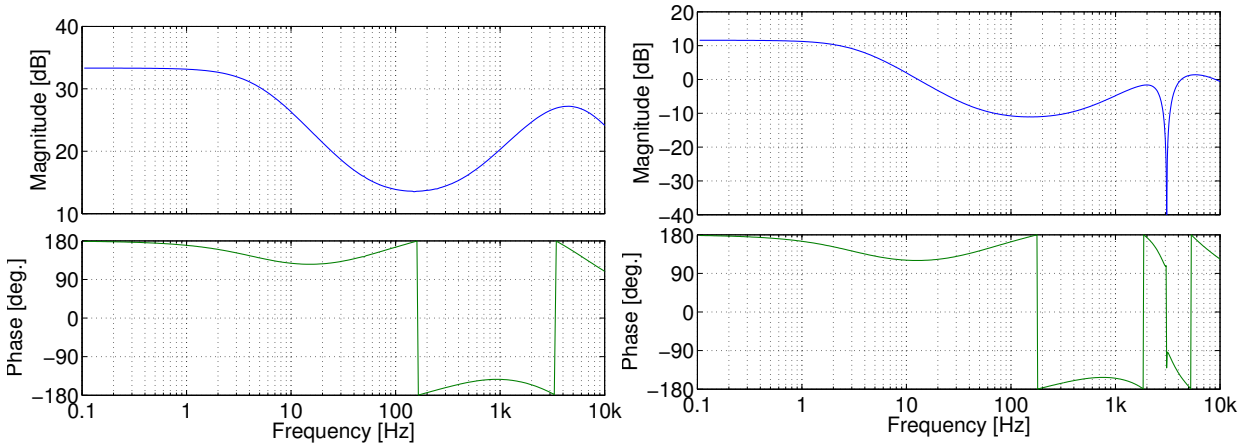

(a) Feedback filter for the MIF servo. (b) Feedback filter the SPI servo.

Fig. 3.54: Frequency responses of the feedback filters. (a) MIF, (b) SPI.

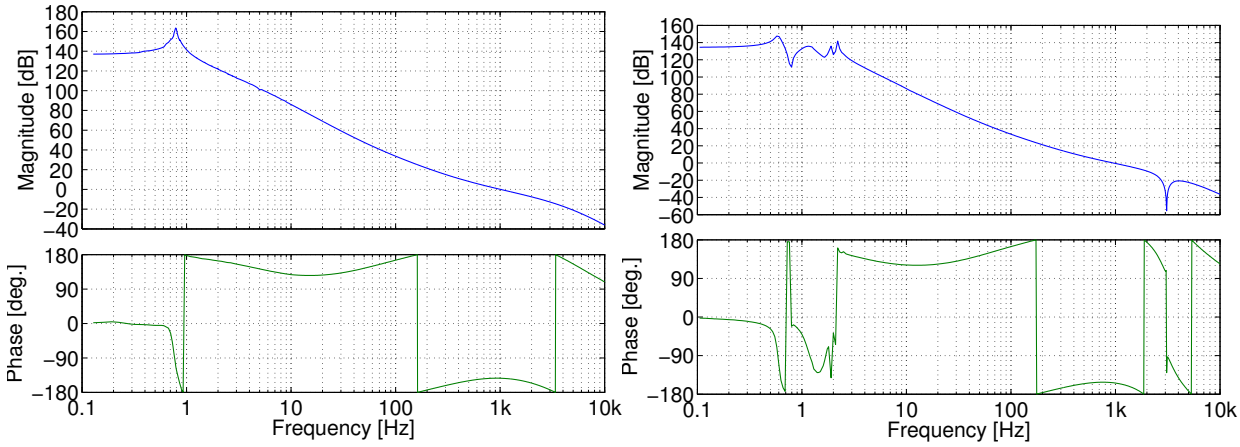

(a) Open-loop transfer function of the MIF servo. (b) Open-loop transfer function of the SPI servo.

Fig. 3.55: Open-loop transfer function of the length control loops. (a) MIF, (b) SPI.

interferometers. The phase margins at the UGFs are about 35° for the MIF loop and 25° for the SPI loop.

3.4.2 Alignment Adjustment

In order to effectively resonate the incident laser light inside the cavity, the mirrors have to be aligned properly to the axis of the incident beam. In this experiment, there are two interferometers to be aligned. They are optically independent interferometers, but mechanically not independent; the orientations of the upper and lower mirrors are coupled because they are connected by wires. So somewhat complicated procedure is needed to align the both interferometers at the same time.

The alignment procedure is basically a three-step process. First, the incident beam axis is adjusted by steering mirrors (M1-M4 in Fig. 3.8) so that the beam hit the center of both the front and the end mirrors. Then, the next step is to adjust the orientation of the mirrors to meet the following two conditions: (a) The axis of the reflected light from the front mirror should coincide with the incident axis, (b) The beam spots on the front mirror which are created by the incident light and the light reflected back from the end mirror should overlap. The orientations of the mirrors of the interferometers have to be adjusted to satisfy the requirements. The third step is the fine adjustment of the beam axis to the cavity axis by the steering mirrors again.

The second step is the most difficult part in this procedure because the orientations of the mirrors are not completely independent. When the SPI mirrors are moved, the mirrors of the MIF are also moved unavoidably. Therefore, the SPI mirrors should be adjusted first. To rotate the mirrors in yaw, the Picomotor on the top-stage MGAS filter is used. To change the pitch tilt of the mirrors, the balance weights on the damping mass are moved. Once the SPI is aligned, the orientations of the MIF mirrors are adjusted. To rotate an MIF mass in yaw, the MIF mass and the SPI mass above it is twisted by hands. Since the wires have some hysteresis, the orientation of the MIF mass is rotated relative to the SPI mass in the twisted direction even after the hands are released. This is a coarse method and requires many trial and errors to achieve a desired rotation. The pitch adjustment is done by attaching small weights on the front or back surfaces of the MIF mass. Small nuts were attached with two-sided tapes during the actual adjustment process.

Since the adjustment of the mirrors' orientation described above is somehow coarse, the fine adjustment of the beam axes should be done as the third step. The steering mirrors are equipped with Picomotor actuators, so that the fine adjustment can be done even when the vacuum chamber is closed.

3.4.3 Lock Acquisition

Lock acquisition is the process of drawing an interferometer to its working point. It is very simple for the interferometers in this experiment.

Mode Cleaner To draw the MC to the working point, the feedback gain of the PZT loop is first set to its maximum. Then a small offset is applied to the temperature control terminal. As the offset is increased slowly, the laser frequency approaches to the resonant frequency of the MC. When those frequencies are close enough, the PZT loop draws the laser frequency to the resonant one. Then the operator turns on the temperature loop.

In this experiment, the MC should always be operated to do any measurement on the MIF and the SPI. The MC is fairly stable and the locked state lasts for many hours. However, there may be a sudden interruption by an earthquake or human errors such as blocking the beam by mistake. In such a case, the MC loses the locked condition. Since the temperature loop includes a complete integrator as a part of the feedback filter, such a failure could result in the injection of a very large voltage to the temperature control terminal which may damage the laser. To avoid this, an "unlock detector" is used. It basically consists of a comparator and relays. It monitors the DC power of the reflected light from the MC. When the MC loses its resonance, the reflected light exhibits a sudden increase. Then the unlock detector, triggered by this increase, turns off the relays to cut the feedback loops.

The MIF and the SPI A suspended mirror exhibits a large motion at the resonances of its suspension system. Therefore, the MIF and the SPI frequently pass their working points as the mirrors swing. In order to lock these interferometers one has to set the feedback gain to an appropriate value and wait for a while. Within a minute, the servo loop catches a resonance and draw the interferometer to its working point.

Once locked, the interferometers are very stable and the locked state can be sustained for many hours. Actually, the interferometers never lose lock unless an operator intentionally turns off the control servos.

3.4.4 Calibration

In this section, the calibration method for the MIF and the SPI is described. Basically the method is the same for the both interferometers.

The block diagram of the length control servo is shown in Fig. 3.53. In this experiment, the measured signal was mainly the output of the whitening filter $x_{\rm w}$. From $x_{\rm w}$, the feedback signal $x_{\rm fb}$ can be easily obtained by dividing $x_{\rm w}$ with the transfer function of the whitening filter W.

If there is a displacement noise $x_{\rm n}$, the feedback signal can be written as

$$x_{\rm fb} = \frac{CPMF}{1+G} x_{\rm n} = \frac{G}{1+G} \frac{x_{\rm n}}{AD}, \tag{3.32}$$

where $G \equiv CPMFDA$ is the open-loop gain of the control loop. Since G is very large at the frequencies of interest,

$$\frac{G}{1+G} \simeq 1. \tag{3.33}$$

Therefore,

$$x_{\mathrm{n}} = AD \cdot x_{\mathrm{fb}} = A \cdot x_{\mathrm{fb}}. \tag{3.34}$$

Here the fact that $D = 1$ is used. To obtain the displacement noise from the feedback signal, x_{fb} is multiplied by the actuation efficiency A.

In order to measure A, a photo-sensor is used in the following way. A photo-sensor is faced to the surface of a mirror. The photo-sensor is mounted on a horizontal stage and the output of the photo-sensor is calibrated by moving the stage with a micrometer. Now A is obtained by measuring the transfer function from the voltage applied to the actuators on the mirror to the output of the photo-sensor.

Measured A for the MIF and the SPI are shown in Fig. 3.56.

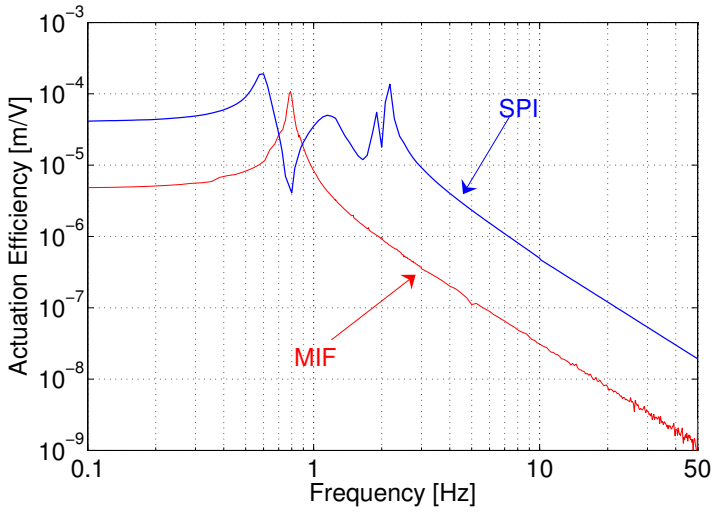

Fig. 3.56: Actuator efficiencies of the MIF and the SPI. The vertical axis is the ratio of the displacement (m) to the actuator input (V).

Chapter 4

Results

In this chapter, the results from the experiments are presented along with the estimation of noises. Basically, two types of the measurements were performed: the spectral measurement and the transfer function measurement. In the spectral measurement, the power spectrum density of the "estimated"[1] displacement noise of the MIF is measured. This measurement shows the vibration isolation performance achieved by the SPI.

In the spectral measurement, the apparent performance of the SPI was limited by couplings from the other degrees of freedom and noises other than the seismic noise. In order to estimate the potential vibration isolation performance of the SPI in the horizontal direction, the horizontal transfer functions of the suspension system with and without the SPI were measured. By comparing those two transfer functions, one can infer how much the vibration isolation can be improved potentially by the SPI.

4.1 Spectral Measurement

The spectral density of the MIF displacement noise was estimated from the feedback signal of the MIF servo as described in section 3.4.4. However, the displacement spectrum obtained in this way does not represent the real displacement of the MIF mirrors. In reality, the motions of the mirrors are suppressed by the servo control well below the obtained spectrum. What the spectrum actually represents is the estimated displacement which would have been induced if the servo had been turned off. In addition, the feedback signal may include noises other than the real vibration of the mirrors, such as the laser frequency noise. In this case, the noise is by no means "displacement", but it is a displacement "equivalent" noise. With those points in mind, the "estimated" or "equivalent" displacement spectra shown in this section are just called "displacement spectra" for simplicity.

Fig. 4.1 shows the displacement spectra of the MIF with and without the SPI locked. The blue spectrum was measured when the SPI was not controlled. When the SPI is locked, the noise of the MIF was reduced as shown in the red spectrum. The noise was reduced all over the frequencies below 10 Hz. The maximum noise-suppression ratio is more than

[1]The meaning of "estimated" is explained in section 4.1.

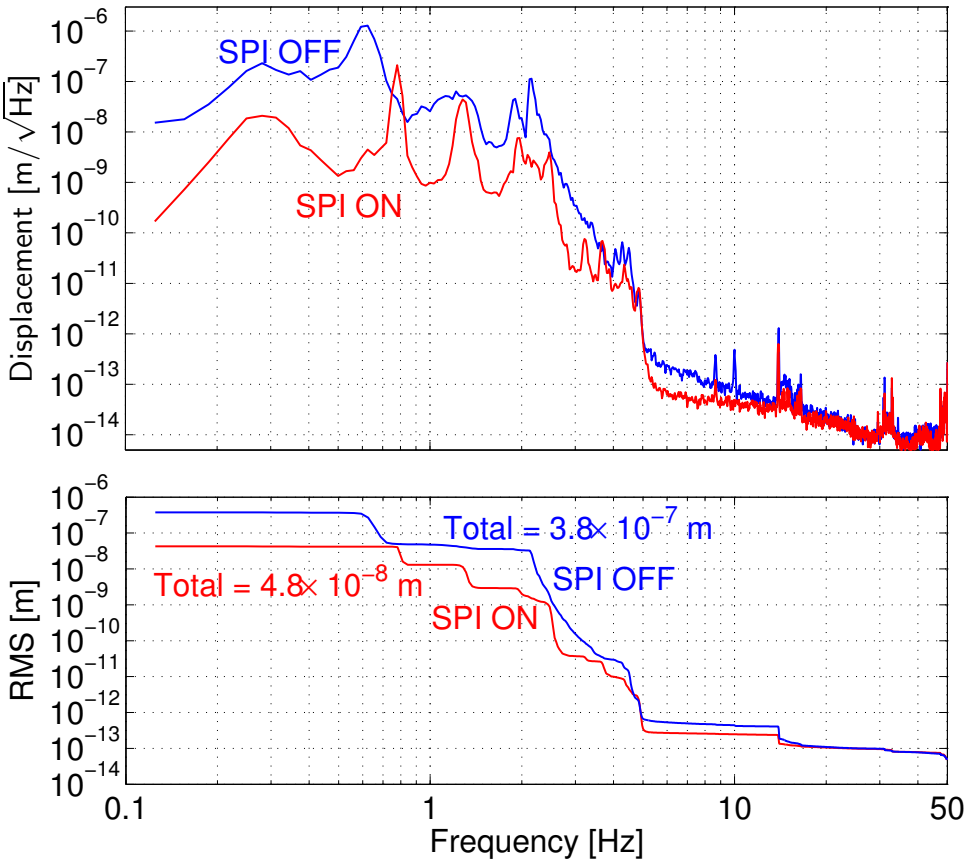

Fig. 4.1: Displacement noise spectra of the MIF. The lower graph shows the cumulative RMS of the spectra integrated from higher frequencies. The blue spectrum is measured when the SPI is turned off. The red one was measured with the SPI on. The total RMS of the blue spectrum is 3.8×10^{-7} m, and that of the red one is 4.2×10^{-8} m.

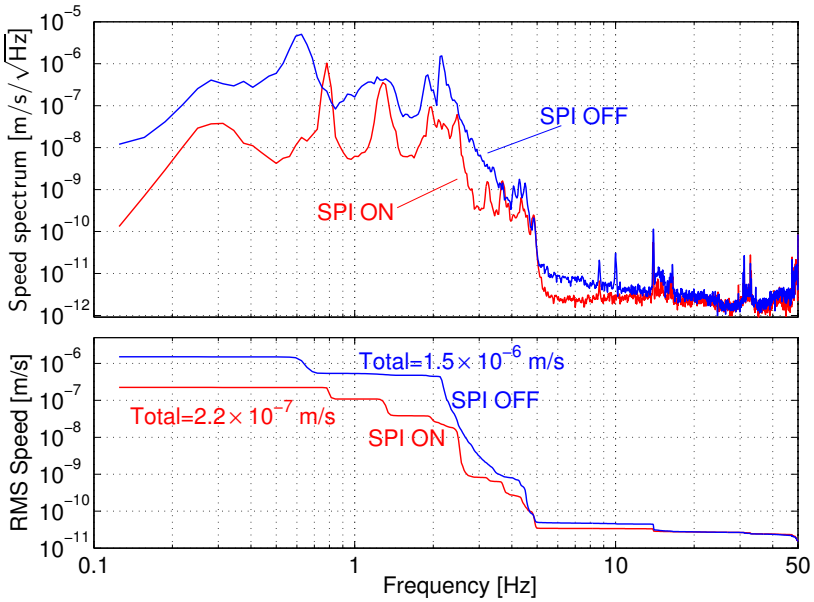

Fig. 4.2: The upper graph shows the speed spectra of the mirrors of the MIF. The lower part shows the cumulative RMSs of the speed spectra. The total RMS speed for the blue spectrum is 1.5×10^{-6} m/s, while it is 2.2×10^{-7} m/s for the red spectrum.

100, typically at 0.6 Hz. The 0.6 Hz peak in the blue curve corresponds to the resonance in which all the masses of the suspension chain coherently move like a single pendulum. It was well suppressed by the SPI and disappears in the red curve.

At 0.8 Hz, a large peak appears in the red curve whereas no corresponding peak can be found in the blue one. This is the resonance of the main pendulum. As described in section 2.4.4, the quality-factor of this resonance increases when the SPI is locked. This is a validation of the rigid-bar picture shown in Fig. 2.8.

The resonant peaks at 1.3 Hz, 1.9 Hz, and 2.5 Hz in the red curve correspond to the pitch resonances of the suspension. Therefore, at those frequencies the coupling from the pitch motion is limiting the performance of the SPI.

At frequencies between 3 Hz and 5 Hz, small peaks appear in the spectra. Those peaks limit the vibration suppression performance of the SPI. Also at frequencies above 5 Hz, the noise suppression ratio by the SPI becomes smaller. Those phenomena are discussed later in section 4.3.1.

The cumulative RMSs of the spectra integrated from higher frequencies are shown in the lower part of Fig. 4.1. The total RMS when the SPI is turned off is 3.8×10^{-7} m and it is reduced to 4.8×10^{-8} m when the SPI is turned on. Therefore, the residual motion of the mirrors is reduced by a factor of 9.

As discussed in section 2.5.5, the actuation force required for the lock acquisition is determined by the RMS speed of the mirrors. The speed spectrum $V(\omega)$ of the mirrors

can be calculated from a displacement spectrum $X(\omega)$ by,

$$V(\omega) = \omega X(\omega). \tag{4.1}$$

Then the RMS speed of the mirrors can be calculated by integrating $V(\omega)$. As shown in Fig. 4.2, it was 1.5×10^{-6} m/s for the measurement with the SPI off, and 2.2×10^{-7} m/s when the SPI was used; the RMS speed was reduced by a factor of 7. Therefore the minimum force required to lock the interferometer, which is proportional to the square of the RMS speed, was reduced by a factor of 49 (see (2.28)). If a maximum actuation force F is given, the maximum finesse of the cavity can be also determined by the RMS speed using (2.28) because the working range d is roughly proportional to the inverse of the finesse. In this case, the finesse of the cavity can be increased by the same factor as the reduction factor of the actuation force.

4.2 Transfer Function Measurement

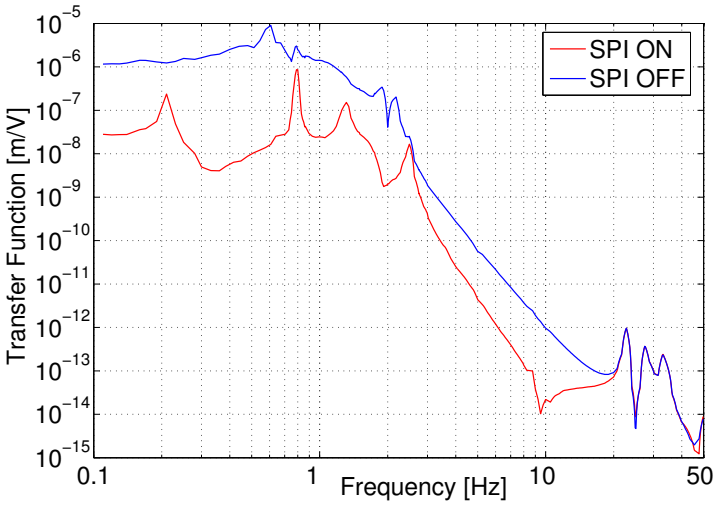

Fig. 4.3: Transfer functions from the input voltage of the horizontal actuator on the damping mass to the displacement of the MIF. The blue curve shows the transfer function when the SPI is off while the red one corresponds to the measurement with the SPI on.

The transfer function of the suspension system was measured in the following way. The damping mass of the end tower was horizontally excited by the horizontal coil-magnet actuators. Then the transmitted motion to the MIF mirrors was measured by the feedback signal of the MIF. Fig. 4.3 shows the transfer functions from the input voltage of the actuators to the displacement of the MIF mirrors. The blue curve was measured when the SPI was off while the red one was measured with the SPI on.

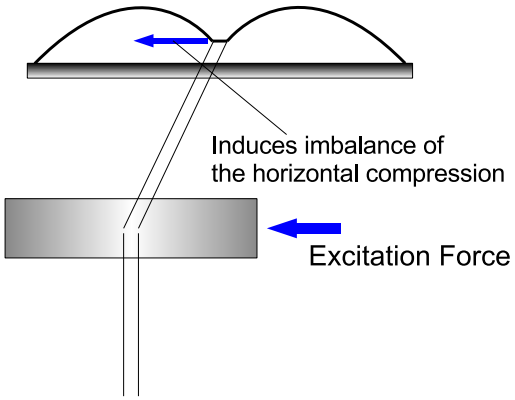

Fig. 4.4: Mechanism of the horizontal to vertical conversion in the top-stage MGAS filter.

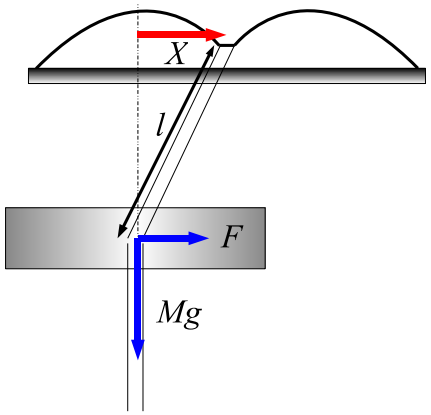

Fig. 4.5: Estimation of H_X from H_D.

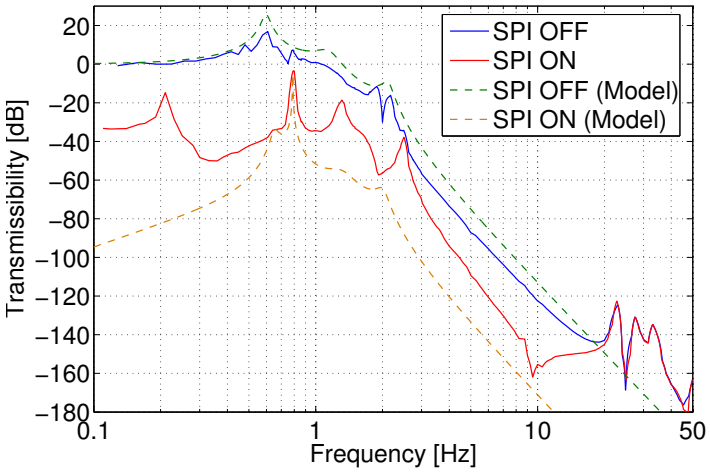

Fig. 4.6: Transfer functions from the horizontal seismic vibration at the top stage (X) to the displacement of the MIF mirror (x). The dashed lines show theoretical transfer functions calculated with an one-dimensional model of the suspension. While calculating the theoretical lines, 1% asymmetry for the wire length of the main pendulums was assumed. The peak at 0.6 Hz in the blue curve corresponds to the lowest horizontal resonance of the suspension chain. The peaks in the red curve are identified as follows. 0.2 Hz: The vertical resonance of the top-stage MGAS filter. 0.8 Hz: The horizontal resonance of the main pendulums. 1.3 Hz & 2.5 Hz: Pitch resonances of the suspension masses. The list of the resonances of the suspension system is given in Table 3.5.

From the measured transfer function, which is called $H_{\rm D}$ from now on, the transfer function from the motion of the top stage X to the motion x of the MIF mirror (called H_X) can be estimated as follows. In the transfer function measurement, the excitation force F was proportional to the voltage applied to the actuators at low frequencies where the inductance of the coils can be ignored. Therefore $H_{\rm D}$ is basically the transfer function from the force F to the displacement x (Fig. 4.5). As shown in the figure, the displacement X of the top stage induces a force $F \simeq Mg \cdot X/l$ to the damping stage, where M is the total mass of the damping mass, the SPI mass, the recoil mass and the MIF mass, l is the wire length, g is the Earth's gravitational acceleration. Since this conversion from X to F is frequency independent, the shapes of H_X and $H_{\rm D}$ are the same; H_X is obtained by scaling $H_{\rm D}$. The scaling factor can be determined from the fact that H_X approaches to unity at very low frequencies when the SPI is turned off. In Fig. 4.6, the X to x transfer functions obtained in this way are shown. Those transfer functions are used to estimate the contribution of the seismic noise to the MIF spectra in section 4.3.1.

Theoretical transfer functions calculated with an one-dimensional model of the suspension system are also shown in Fig. 4.6. To calculate those transfer functions, the asymmetry of the wire length of the main pendulums was assumed to be 0.25%, which is estimated from the resonant frequency measurements described in section 4.2.2.

4.2.1 Interpretation of the Measured Transfer Functions

In Fig. 4.6, the difference between the two curves indicates the potential vibration isolation performance of the SPI. In general, the improvement of the vibration isolation by a factor of 10 to 100 was achieved.

In principle, the performance of the SPI should be improved at low frequencies as discussed in section 2.4.1 and shown in Fig. 2.10. However at frequencies between 0.1 Hz and 0.3 Hz, the red curve has a peak. This peak corresponds to the resonance of the top-stage MGAS filter. The horizontal force exerted on the damping mass induces imbalance of the horizontal compression between the blades as shown in Fig. 4.4. Consequently, the vertical equilibrium position changes.

Two significant peaks in the red curve at 1.3 Hz and 2.5 Hz do not appear in the theoretical curve. Those peaks correspond to the pitch resonances of the suspension system. The asymmetry of the suspension system or the imbalance of the excitation force produce this pitch-to-horizontal coupling.

In the case of the SPI being on, the theoretical curve is below the measured transfer function except at the resonant frequency (0.8 Hz) of the main pendulum. It is most likely that couplings from other degrees of freedom limit the improvement of the transfer function. Considering the above discussions on the peaks in the transfer functions, the sources of the couplings are likely to be the vertical motion at frequencies below 0.8 Hz, and the pitch rotation at frequencies above 0.8 Hz.

Above 10 Hz, the measurement was contaminated probably by electric cross talk.

4.2.2 Asymmetry of the Main Pendulums

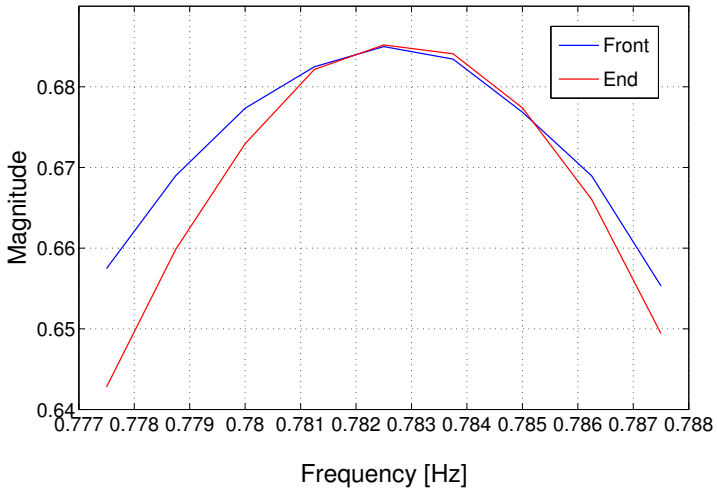

Fig. 4.7: Transfer functions of the main pendulums from the actuation voltage to the output of the photo sensor.

As discussed in section 2.4.1, the vibration isolation performance of the SPI is limited by the asymmetry of the pendulum length at frequencies higher than the resonances of the main pendulums. In order to measure this asymmetry, the resonant frequencies of the front and the end main pendulums were measured.

A photo sensor was faced to the surface of an MIF mirror. Then the transfer function from the input voltage of the horizontal actuators on the mirror to the output of the photo sensor was measured. This measurement was repeated for both of the suspensions. The results are shown in Fig. 4.7.

From those measurements, it can be inferred that the difference of the resonant frequencies is less than 1 mHz. This corresponds to 0.25% asymmetry of the pendulum lengths. Therefore, the CMRR is more than 50 dB at frequencies above this resonance (0.8 Hz). However the difference between the red and blue curves in Fig. 4.3 is less than 40 dB above 0.8 Hz. This is probably because couplings from other degrees of freedom is limiting the improvement of the vibration isolation at those frequencies. Especially a peak at 2.5 Hz in the red curve corresponds to a pitch resonance of the suspension system. Therefore, the pitch to in-line coupling appears to be dominant around this peak.

4.3 Noise Estimation

In this section, effects of various noises to the sensitivity of the MIF are estimated.

4.3.1 Seismic Noise

Seismic noise is supposed to be the dominant noise in this experiment. The contribution of the seismic noise to the MIF spectra is estimated in the following way. First, the spectrum of the seismic vibrations on the top stage in the in-line direction was measured by an accelerometer, RION LA-50. Then, the seismic noise at the MIF is estimated by multiplying the spectrum with the transfer function of the suspension system obtained by the transfer function measurements in section 4.2.

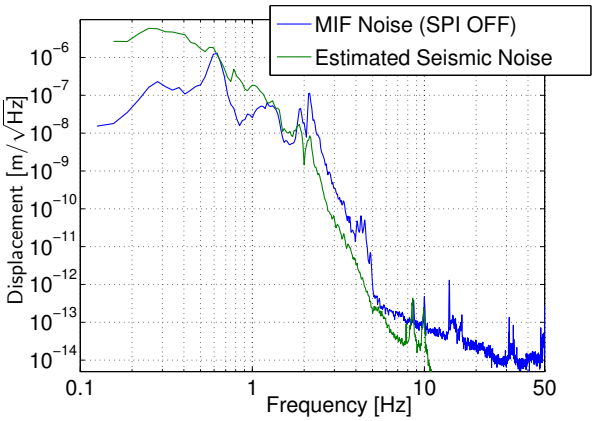

Fig. 4.8: The estimated seismic noise spectrum when the SPI is OFF.

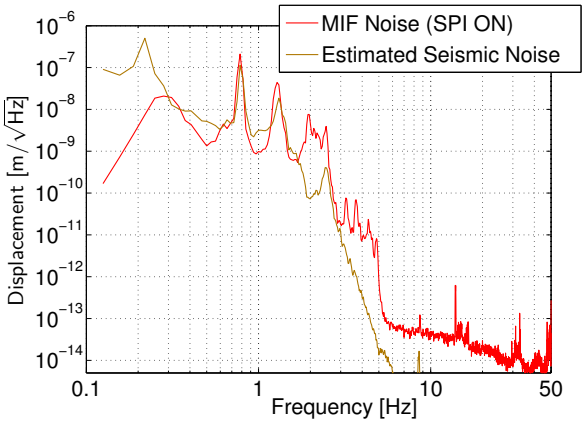

Fig. 4.9: The estimated seismic noise spectrum when the SPI is ON.

In Fig. 4.8 and Fig. 4.9, the estimated seismic noise spectra are shown along with the MIF noise spectra. In both figures, the estimated seismic noise is larger than the measured MIF noise at low frequencies. This is probably because of the common mode rejection due to the close placement of the two suspension towers.

At frequencies above 2 Hz in Fig. 4.8, the estimated seismic noise is below the measured noise. The reason for this difference is not clear, but there are several possibilities. First, the seismic vibration when the accelerometer measurement was done may have been quieter than when the MIF noise was measured. Another possibility is that couplings from other degrees of freedom, most probably from the pitch, may have increased the transmission of the seismic vibration to the MIF. In any case, the resemblance between the shape of the estimated and the measured noises strongly suggests that the MIF noise without the SPI is dominated by the seismic noise up to 5 Hz.

When the SPI is turned on, the estimated and measured noises match between 2.5 Hz and 3 Hz. This fact has an important implication for the mechanism of the couplings from the other degrees of freedom; a hypothetical model of the couplings can be constructed as follows. Since the MIF mass has a relatively simple structure, the conversion from the motions in the other degrees of freedom to the in-line motion is likely to happen mainly in the more complex upper suspension stages, the damping stage and the SPI stage. The difference between the blue and green curves in Fig. 4.8 above 2 Hz could be interpreted

as the result of this couplings. When the SPI is turned on, this converted horizontal motion can be suppressed by the SPI. Therefore, in Fig. 4.9, the two curves match between 2.5 Hz and 3 Hz. Since this is only a hypothetical model inferred from the measurements performed so far, further experimental confirmation is needed.

From 3 Hz to 5 Hz there are several peaks in the red curve in Fig. 4.9. The shapes of those peaks look like mechanical resonances. In order to find the source of the peaks, various transfer functions of the suspension system were measured changing the excitation and observation points. However, no resonance was found between 3 Hz and 5 Hz. Those peaks may be resonances of the fixed optical components such as the steering mirrors, the beam splitters or the photo detectors. The identification of those peaks is one of the first priority tasks to be done in the future.

Above 5 Hz, the noise slope of the MIF becomes more gradual and it clearly differs from the seismic noise slope. Therefore, it is reasonable to suppose that the noise in this region is not dominated by the seismic noise. However, as shown in the Fig. 4.1, the noise of the MIF in this frequency region was reduced by a factor of 2 or 3 when the SPI is used. The mechanism of this noise reduction has not yet fully understood. However, it is likely that the magnitude of the dominant noise in this region is somehow coupled to the RMS motion of the MIF mirrors; the reduction of the RMS by the SPI reduced the noise in this region. Laser intensity noise is well known to have this kind of behavior; it appears in an interferometer's output coupled with the RMS. However, the estimation of the intensity noise level given in section 4.3.3 excludes the possibility of this noise being the dominant noise in this region. Furthermore, none of the noises estimated in the following sections have an enough noise level to account for the measured MIF noise. Other candidate noises, which have not been measured yet, are the non-linearity of the actuators or the electric circuits, beam jitters, and other unknown noises. The determination of the dominant noise source above 5 Hz is also a high-priority future work.

The correlation between the seismic noise measured by an accelerometer and the noise of the MIF was measured. The accelerometer was placed on the floor of the laboratory between the front and the end vacuum chambers.

Fig. 4.10 shows the correlation between the vertical seismic vibration and the output of the MIF. At low frequencies (below 1 Hz), high correlation between them is observed when the SPI is on. This is a good evidence that the performance of the SPI is limited by the coupling from the vertical motion at those frequencies. When the SPI is off, high correlation with the vertical vibration only appears around 0.2-0.3 Hz, where the resonances of the MGAS filters reside.

Fig. 4.11 shows similar correlation plots with the in-line seismic vibration. In this case, the MIF noise has high correlation with the seismic vibration at low frequencies when the SPI is "off" in contrast to the case of the vertical vibration. In the both states of the SPI (on and off), the MIF output has a high correlation with the in-line seismic vibration between 1 Hz and 3 Hz. The correlation goes down rapidly when the SPI is on. Some correlation remains up to 4 Hz and then drops to almost zero in the case of the SPI being off. This destruction of the correlation is due to the peaks around 3 to 5 Hz. A small peak in the correlation between 5 and 6 Hz when the SPI is off suggests that there is still some

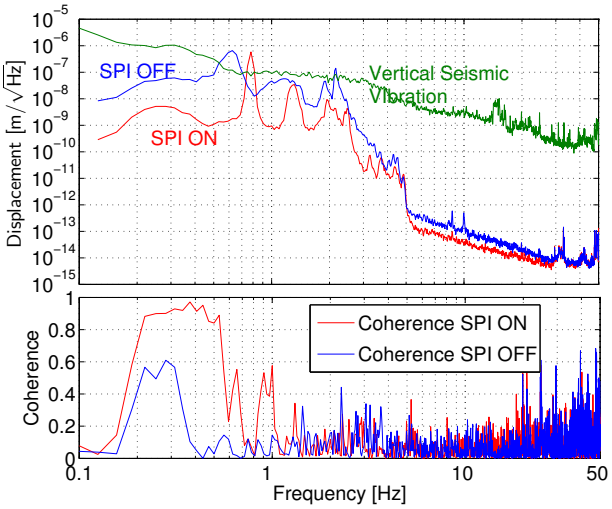

Fig. 4.10: Correlation between the vertical seismic noise and the noise of the MIF.

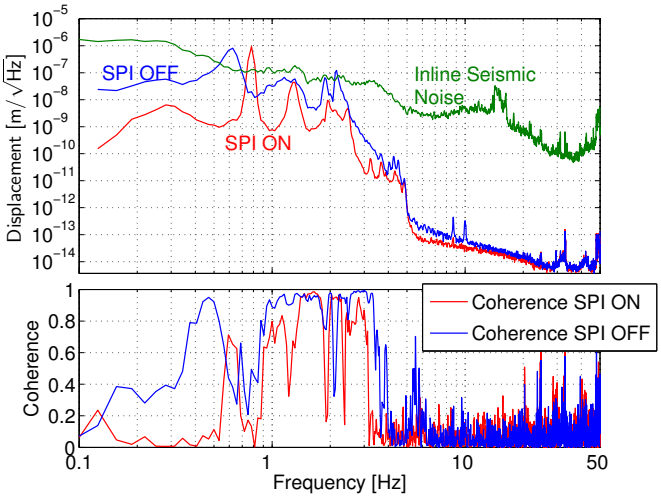

Fig. 4.11: Correlation between the in-line seismic noise and the noise of the MIF.

contribution from the seismic noise in the MIF without the SPI.

4.3.2 Electronic and Detector Noises

Various electric circuit noises were measured and their contributions to the MIF noise are shown in Fig. 4.12. "Detector noise" is the noise generated during the process of the photo detection and the demodulation. This noise includes shot noise, electric circuit noise of the photo detector and the mixer, and the RF amplitude modulation noise. The final one needs further explanation.

The 15 MHz EOM ideally does not generate any amplitude modulation. However, if the input polarization is not optimum, amplitude modulation at 15 MHz is induced. Besides, piezoelectric effect of the pockels cell induces the jitter of the transmitted beam at the modulation frequency. This jitter generates amplitude modulation if the beam is transmitted through an optical component with a small aperture. The magnitude of the amplitude modulation fluctuates if the EOM is shaken by the seismic vibration. The temperature variation also causes a fluctuation of the amplitude modulation. Those fluctuations are detected as a noise when it is demodulated by the mixer. It is called "RF amplitude modulation noise" in this thesis.

In order to estimate the detector noise, the noise v_{error} at the error signal port was measured while the light path inside the cavity was blocked to avoid the resonance. According to the block diagram shown in Fig. 3.53, the displacement equivalent detector noise x_{det} is obtained by

$$x_{\mathrm{det}} = \frac{ADF}{1+G} v_{\mathrm{error}}. \tag{4.2}$$

The brown curve in Fig. 4.12 shows the estimated detector noise. The orange colored curve is the detector when the 15 MHz signal is not sent to the EOM and the demodulator. Since the orange curve is well below the brown one, it can be said that the RF amplitude modulation noise is dominant in the detector noise.

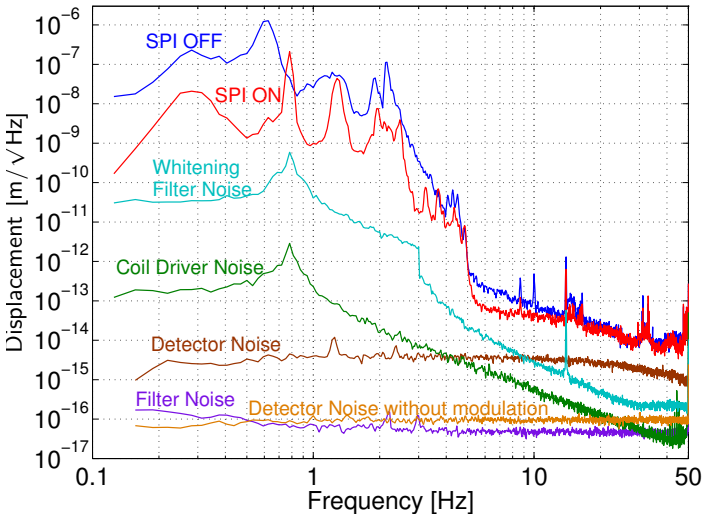

Fig. 4.12: Various electric noises and the detector noise.

The noise of the feedback filter is shown in the figure as a purple curve. To obtain the curve, the noise v_{filter} of the feedback filter was measured with its input grounded. Then it is converted to the displacement equivalent noise x_{filter} by

$$x_{\mathrm{filter}} = \frac{AD}{1+G} v_{\mathrm{filter}}. \tag{4.3}$$

The effect of the noise generated in the coil driver is estimated by

$$x_{\mathrm{coil}} = A v_{\mathrm{coil}}, \tag{4.4}$$

where x_{coil} is the displacement equivalent coil-driver noise and v_{coil} is the noise of the coil driver when its input is grounded.

In order to record the feedback signal with high resolution, whitening filters are used as shown in Fig. 3.53. The noise of the whitening filters converted to the displacement equivalent noise is shown in Fig. 4.12 as a light blue curve. Since two whitening filters are used, one for low frequency (below 3 Hz) and another for high frequency (above 3 Hz), the whitening filter noise exhibits a jump at 3 Hz.

4.3.3 Laser Intensity Noise

The laser intensity noise appears in the MIF signal coupled with the RMS of cavity length fluctuation as

$$x_{\mathrm{int}} = \frac{\Delta P}{P} x_{\mathrm{rms}}. \tag{4.5}$$

Here, x_{int} is the displacement equivalent intensity noise, x_{rms} is the RMS of the cavity length fluctuation, P and ΔP are the power of the laser light and its fluctuation.

In Fig. 4.13, the relative intensity noise ($\Delta P/P$) of the incident light power to the MIF is shown.

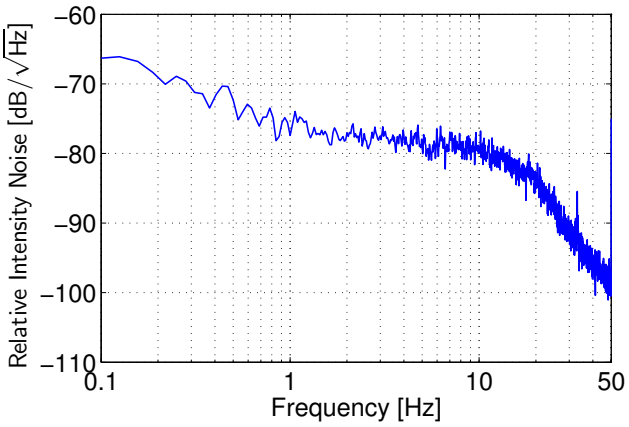

Fig. 4.13: Relative intensity noise of the laser power just before injected into the MIF.

In order to convert this noise to the displacement equivalent noise, the transfer function from the intensity modulation to the corresponding signal of the MIF was measured as follows.

First, the half-wave plate after the EOM was slightly rotated so that a fraction of the incident light is reflected by the PBS before the MIF (Fig. 3.8). The reflected light was detected by a photo detector to monitor the intensity fluctuation. Then, the laser light intensity was modulated by changing the LD current sinusoidally. When the modulation is large enough, a peak appears in the MIF signal at the modulation frequency. By sweeping the modulation frequency, the transfer function from the intensity modulation to the MIF signal was measured.

By multiplying the intensity noise spectrum shown in Fig. 4.13 with the measured transfer function, the displacement equivalent intensity noise level was estimated (Fig. 4.14). The noise level is more than an order of magnitude below the MIF noise.

4.3.4 Laser Frequency Noise

The laser frequency noises estimated in section 3.4.1 are shown in Fig. 4.15 as displacement equivalent noises. The laser frequency noise without the stabilization is larger than the

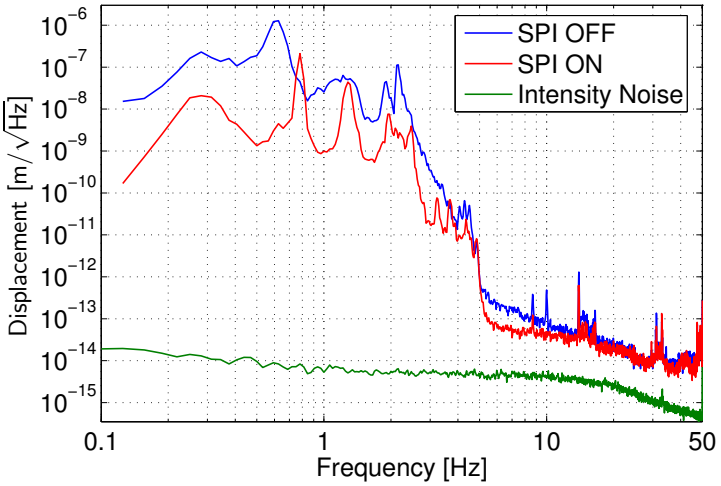

Fig. 4.14: Contribution of the intensity noise to the noise of the MIF.

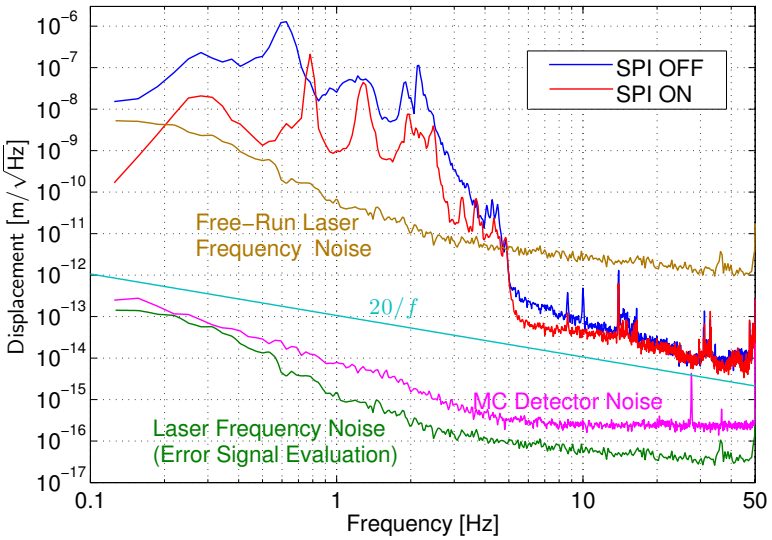

Fig. 4.15: Contributions of the frequency noises to the noise of the MIF.

achieved sensitivity of the MIF. Therefore the frequency stabilization with the MC is crucial in this experiment. The MC detector noise is well below the noise of the MIF. However, if the $20/f$ noise is assumed for the fluctuation of the MC cavity length, the frequency noise level increases close to the MIF noise level above 5 Hz. As discussed in section 3.4.1, the real frequency noise may be larger than this. Therefore, the frequency noise is a considerable candidate of the limiting noise above 5 Hz.

4.3.5 Other Noises

Shot Noise

In the detector noise estimated in section 4.3.2, the shot noise was included. Here, the shot noise level is estimated theoretically.

The DC photo current i_{DC} on the RF photo detector was 5.6 mA. From this, the power spectrum density of the shot noise current i_{sn} is obtained using the elementary charge e,

$$i_{\mathrm{sn}} = \sqrt{2ei_{\mathrm{DC}}} = 4.2 \times 10^{-11}\,\mathrm{A}/\sqrt{\mathrm{Hz}}. \tag{4.6}$$

This shot noise current is converted to the displacement equivalent noise using the gain of the photo detector's pre-amp and the demodulator. The obtained shot noise level is $1.1 \times 10^{-16}\,\mathrm{m}/\sqrt{\mathrm{Hz}}$. This is almost the same as the detector noise without modulation (see Fig. 4.12). The estimated shot noise is shown in Fig. 4.16 as a pink line.

Thermal Noises

Suspension Thermal Noise To estimate the suspension thermal noise level, the quality factor of the main pendulum was measured by observing its ring down. Since the eddy current damping is applied between the MIF mass and the recoil mass, the quality factor was very low, $Q = 26.5$.

The power spectrum density of the suspension thermal noise is calculated by the following formula:

$$x_{\mathrm{susth}}(\omega) = \sqrt{\frac{4k_{\mathrm{B}}T}{mQ}\frac{\omega_0}{\left(\omega^2 - \omega_0^2\right)^2 + \omega_0^2\omega^2/Q^2}}. \tag{4.7}$$

Here, k_{B} is the Boltzmann constant, T is the temperature, m is the mass of the MIF mass, and ω_0 is the angular resonant frequency of the pendulum. This formula is the direct consequence of the fluctuation-dissipation theorem applied to a harmonic oscillator. Since the first violin mode frequency of the suspension wires is high enough (170 Hz), the contributions from the violin mode resonances are not taken into account.

The estimated suspension thermal noise is shown in Fig. 4.16 as a green curve. Around 5 to 6 Hz, this noise is close to the MIF noise. The contribution of the suspension thermal noise to the MIF noise may be considerable in this frequency region.

Mirror Thermal Noise The mirror thermal noise is estimated by the following formula [38],

$$x_{\mathrm{mth}}(f) = \sqrt{\frac{4k_{\mathrm{B}}T}{f}\frac{1-\sigma^2}{\pi^3 Er}I\phi}. \tag{4.8}$$

Here, E and σ are the Young's modulus and the Poisson ratio of the mirror substrate, r is the radius of the laser beam on the mirror, and $I = 1.87322$ in the case of a Gaussian beam. The loss angle ϕ is related to the quality factor Q by $\phi = 1/Q$ in the case of the structure damping model.

In this experiment, the mirror is glued to an aluminum body. Therefore, the mechanical quality factor is expected to be low. The mirror thermal noise calculated with $Q = 1000$ is shown as an orange line in Fig. 4.16. The line is well below the MIF noise floor. Hence, the mirror thermal noise is considered to have no contribution to the MIF noise.

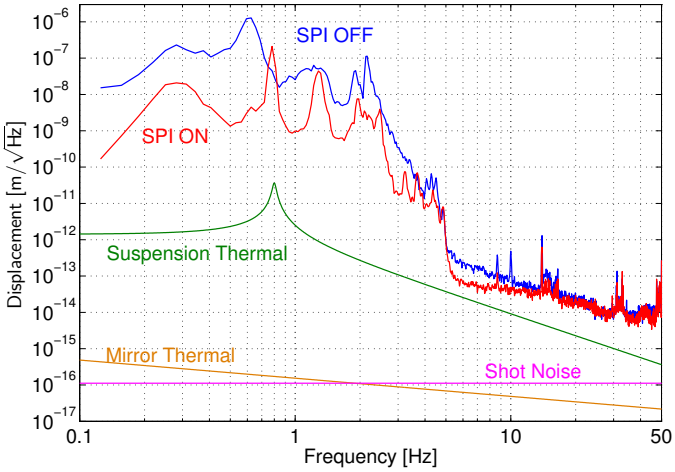

Fig. 4.16: The shot noise and the thermal noises.

Residual Gas Noise

The random motion of the residual gas molecules causes the fluctuation of the index of refraction. This fluctuation induces the variation of the effective optical length of the cavity. The noise generated by this fluctuation is called "residual gas noise".

The magnitude of the residual gas noise is estimated by the following formula [9]:

$$x_{\mathrm{gas}} = \sqrt{\frac{L(n_0-1)^2 k_B T_0^2 p}{2\pi r p_0^2 u_0 T}\sqrt{\frac{T_0}{T}}}. \tag{4.9}$$

L is the length of the cavity; n_0, p_0, u_0 and T_0 are the index of refraction, the pressure, the mean speed of molecules and the temperature in the standard state ($T_0 = 273.15\,\mathrm{K}$,

p_0 =1 atm), respectively. T and p are the temperature and the pressure inside the vacuum chambers. Using $n_0 - 1 = 3 \times 10^{-4}$ and $u_0 = 0.42\,\mathrm{km/s}$, the residual gas noise is estimated to be $1.8 \times 10^{-21}\,\mathrm{m}/\sqrt{\mathrm{Hz}}$, when $p = 10^{-2}\,\mathrm{Pa}$. This is completely negligible.

4.3.6 Noise of the SPI

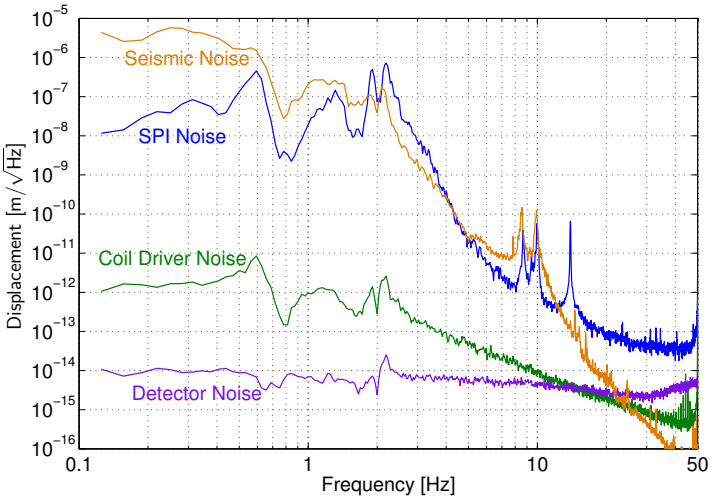

Fig. 4.17: Noise spectra of the SPI.

The displacement noise of the SPI is shown in Fig. 4.17. The noise is likely to be limited by the seismic noise up to 10 Hz. This is supported by the correlation measurement shown in Fig. 4.18, where the correlation between the in-line seismic noise and the SPI signal was measured.

If the sensitivity of the SPI is limited by noises other than the seismic noise, the noise could be transmitted to the MIF as an extra noise. An important result of this experiment is that the noise of the MIF is not increased by the use of the SPI at all frequencies; the SPI does not introduce any extra noise to the MIF. This is a virtue of the SPI because an active vibration system often introduces some extra noises to the system to be stabilized at frequencies where its sensor has a poor sensitivity.

4.3.7 Summary of the Noises

In order to obtain the total noise estimation, the noises estimated above are added quadratically. In Fig. 4.19, the total estimated noises[2] are shown in both cases of SPI is on and off. The estimations are a little bit smaller than the measured spectra, though the noise shapes are quite similar.

[2]The $20/f$ noise of the MC is not included.

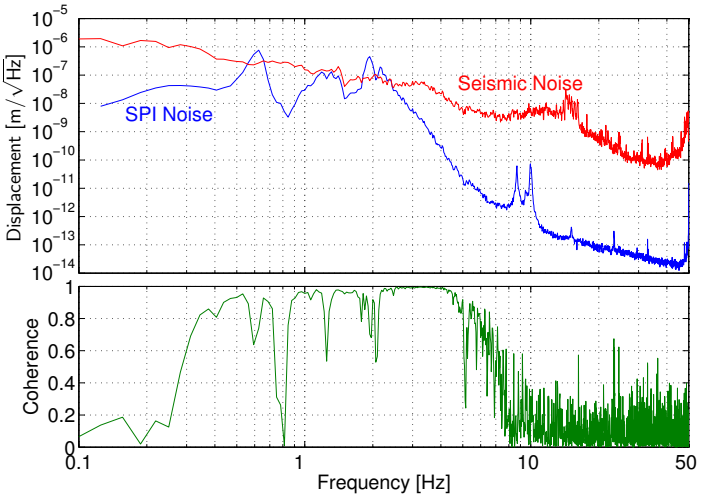

Fig. 4.18: Correlation between the seismic noise and the SPI noise.

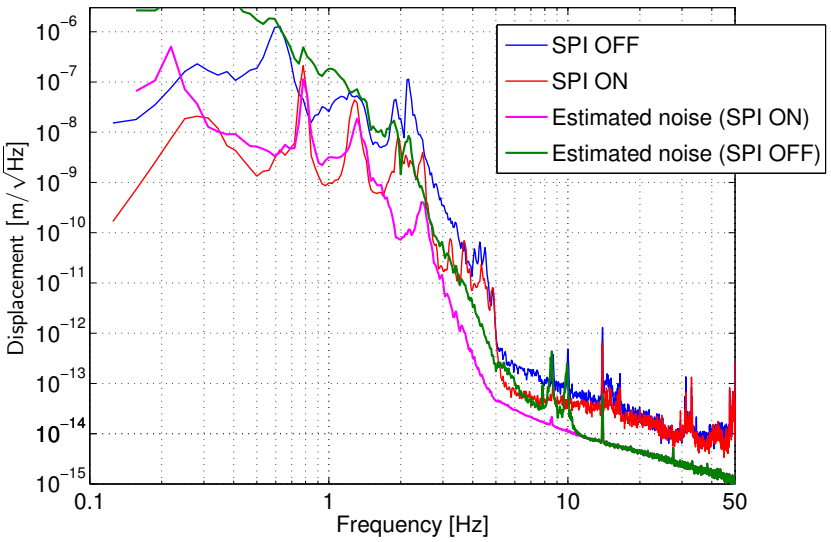

Fig. 4.19: Sum of the estimated noises in the MIF.

At low frequencies (below 5 Hz), the noise of the MIF was determined by the seismic noise. When the SPI is used, the coupling from the vertical motion becomes dominant below 1 Hz. Above 5 Hz several noises are likely to contribute to the MIF noise. Possible noises include the light intensity noise, the detector noise, and the suspension thermal noise. Also the laser frequency noise may have a major contribution in this region.

Chapter 5

Conclusion and Future Works

5.1 Conclusion

In this experiment, the practical operation and the performance of an SPI were tested. The operation of the interferometers were very stable. Lock was never lost unless intentionally turned off.

From the spectral measurement, it was shown that the noise of the MIF was reduced at maximum over 40dB below 10 Hz. The suppression ratio was limited by coupling from the vertical motion at low frequencies (below 1 Hz). The source of the resonances in 3-5 Hz and the dominant noise source above 5 Hz need to be determined in the future. The RMS motion of the MIF mirrors was reduced by a factor of 9 with the SPI.

The transfer function measurement showed the potential performance of the SPI. It has the vibration suppression performance of 20 dB to 40 dB at frequencies below 10 Hz.

5.2 Future Works

Several ideas for the future works on the SPI are presented here.

5.2.1 Alignment Mechanism

This experiment confirmed the principle and a practical performance of the SPI. However, before going to implement this scheme in large interferometers, an important issue has to be addressed, that is, how to adjust the alignment of the SPI and the MIF independently. The alignment procedure used in this experiment can not be applied to larger interferometers because, with the coarse "twisting" method, the alignment precision required for large scale interferometers is likely to be not satisfied. Therefore, some mechanisms to allow independent alignment adjustment are needed.

One idea is to use composite mirrors for the SPI. A conceptual design is shown in Fig. 5.1. The mirror is attached to a body mass through some actuators. With the actuators, the mirror can be tilted with respect to the body. In this way, the orientation of the

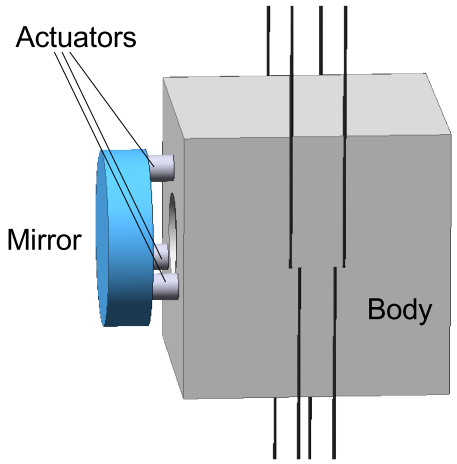

Fig. 5.1: Composite mirror for the SPI.

SPI mirror can be changed without affecting the MIF mirror below.

The composite structure is expected to have a lower mechanical quality factor than the monolithic one. The mirrors of the MIF are required to have a very high quality factor to achieve a low thermal noise. Therefore, the use of monolithic mirrors is mandatory. However, the requirement for the SPI mirror is relaxed as explained in section 2.4.5. Typically at 10 Hz the noise requirement for the SPI is relaxed from that for the MIF by a factor of 100. Since the thermal noise is inversely proportional to the square-root of the quality factor, this means the quality factor can be 10^4 times lower. Therefore, the use of the composite structure is a possible option for the SPI mirrors.

The actuators supporting the mirror could be PZT actuators. However, the actuation range of PZTs may be too small. Besides, the noise of the voltage applied to the PZTs may introduce an extra noise to the SPI. In LCGT, the SPI stage is cooled down to 15 K. Therefore, the actuators also have to work in that low temperature. To meet those requirements, further studies and experimental tests should be done on this problem.

5.2.2 SPI at an Upper Stage of a Suspension System

The SPI was installed one stage above the MIF in this experiment. This is because the experiment was designed with application to LCGT in mind; in order to suppress the vibrations from heat links, the SPI should be placed close to the MIF. However, in room-temperature interferometers, an SPI could be installed at upper stages of the suspension system.

At upper stages of a suspension, the vibration to be suppressed is large because it is not well attenuated by the suspension system. Therefore, the requirement for the sensitivity of the SPI is further relaxed. One can use a very low-finesse cavity or even a Michelson interferometer with corner-cube end mirrors as in [4]. This will simplify the construction and operation of the SPI.

One disadvantage of this configuration is that the performance of the SPI is likely to be limited more severely by couplings from other degrees of freedom. The reason is discussed as follows. When an SPI is installed close to the MIF, the SPI can suppress the in-line vibration which was converted from motions in the other degrees of freedom at upper stages. In contrast, when the SPI is installed at an upper stage of the suspension, the conversion which occurs at stages below the SPI directly affects the MIF. Therefore, an SPI installed at an upper stage may have poor high-frequency performance. Still, this configuration is useful for reducing large seismic motions at low frequencies to improve the stability of the interferometer and help lock acquisition.

5.2.3 Dual Band Interferometers

The SPI can have potentially the same sensitivity as the MIF at high frequencies where the seismic noise is not dominant. Therefore, the SPI can be used to detect gravitational waves at those frequencies. One possibility is to optimize the SPI for high frequencies while optimizing the MIF for low frequency gravitational waves.

Suppose that the sensitivities of the interferometers are limited only by quantum noises, the shot noise and the radiation pressure noise. The radiation pressure noise is significant at low frequencies. In order to reduced this noise, the light power has to be reduced. However, this will increase the shot noise, which becomes significant at high frequencies. If a low power laser is used for the MIF, the MIF is optimized for low frequencies at the expense of a poor high-frequency sensitivity. In order to complement the high frequency sensitivity, a high power laser is used for the SPI, and it is responsible for the high frequency region. The combination of those interferometers will give a wide bandwidth interferometer.

Since this is a mere idea, further considerations on a practical design to realize this configuration are needed.

Appendix A

Application to LCGT

In this chapter, application of SPI to LCGT interferometer is discussed. A schematic illustration of the suspension system of LCGT is shown in Fig. A.1 [19]. It is based on Seismic Attenuation System (SAS) developed for LIGO and TAMA [39]. The whole suspension chain is supported by inverted pendulums, which are ultra low-frequency horizontal vibration isolation devices. A good vertical vibration isolation performance is provided by a series of MGAS filters.

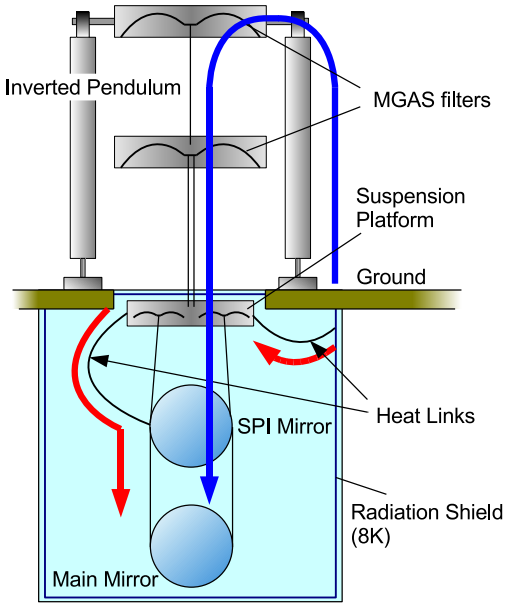

Fig. A.1: The suspension system of LCGT.

An SPI is formed one stage above the main interferometer. The SPI mirror is connected to the radiation shield, which is cooled down to 8 K, through heat links. The heat links are made of pure aluminum wires and used to conduct heat in order to cool down the mirrors.

The mirror for the main interferometer is suspended from the SPI mirror by sapphire wires to ensure good heat conduction.

Seismic vibration is transmitted to the main mirror through two paths. The first path is the one through the suspension chain (indicated by a blue arrow in the figure). The vibration introduced through this path is significant at low frequencies (below 1 Hz) and determines the amount of the RMS motion of the mirror. The second path is the one through the heat links; it is indicated by red arrows in the figure. This path becomes significant at high frequencies (above 1 Hz).

The SPI is expected to provide mainly two benefits to LCGT, the vibration attenuation of the heat links, and the reduction of the RMS motion of the mirrors. The heat link issue is discussed in section A.1. The RMS reduction will improve the stability of the interferometer and allow us to use more delicate actuators for the control of the interferometer. Consequently, some of the technical noises such as actuator noise will be reduced. Quantitative estimation of the RMS reduction and its effect on actuator noise are discussed in section A.2.

A.1 Attenuation of Vibrations Introduced from Heat Links

In LCGT, the heat links are necessary to cool down the mirrors. However, the heat links could be a bypass to introduce vibrations from the radiation shield, because the radiation shield vibrates as much as the ground and the heat link wires are attached to the stages close to the main mirror. The SPI can be used to actively attenuate this extra vibrations introduced from the heat links.

In Fig. A.2, estimations of vibration introduced from the heat links to the main mirror are shown along with the target sensitivity of LCGT. The estimated noise spectra are calculated with a point-mass model of the suspension system and the heat links developed by T. Uchiyama [19]. The attenuation performance of the SPI was assumed to be -40 dB. Cross-couplings of 1 % from the vertical and perpendicular vibrations to the in-line direction are taken into account in this simulation.

Without the SPI, the vibration introduced from the heat links prevent us from achieving the target sensitivity of LCGT. By making use of the SPI, this extra vibration can be reduced mostly below the target sensitivity.

A.2 Reduction of the RMS Motion of the Mirrors

One of the virtues of SPI is its ability to suppress large motion of the mirrors at low frequencies. Using the results from a three-dimensional simulation of the suspension system of LCGT developed by A. Takamori, the reduction of the RMS motion of the mirrors by the SPI in the case of LCGT is estimated here. In this simulation, the introduction of

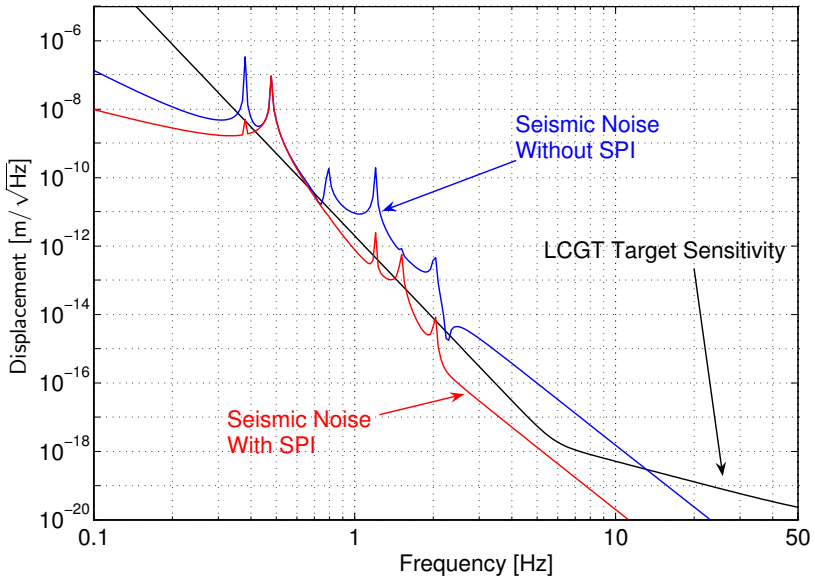

Fig. A.2: Seismic noise introduced from the heat links, by courtesy of T. Uchiyama.

vibration from the heat links was not taken into account, because it is only significant at higher frequencies and does not contributes to the RMS so much.

In Fig. A.3, the seismic noise spectra of LCGT with and without the SPI are shown. To calculate those spectra the ground motion spectrum of Kamioka mine was modeled as,

$$x_{\mathrm{seis}} = \begin{cases} \left(\frac{10^{-8}}{f^2}\right) \mathrm{m}/\sqrt{\mathrm{Hz}} & f \geq 0.1\mathrm{Hz} \\ 10^{-6}\mathrm{m}/\sqrt{\mathrm{Hz}} & f < 0.1\mathrm{Hz} \end{cases}. \tag{A.1}$$

This spectrum was multiplied with the transfer functions of the suspension system calculated by the simulation to get a seismic noise spectrum. The seismic motion is assumed to be isotropic, i.e. the ground moves by the same amount in the horizontal and vertical directions. The horizontal vibration attenuation by the SPI was assumed to be $-40\,\mathrm{dB}$, and the cross-couplings from the vertical or perpendicular vibrations to the in-line motion were assumed to be $1\,\%$.

In the lower region of Fig. A.3, the cumulative RMSs of the above spectra are shown. The total RMS of the mirror motion is $2.2\,\mu$m in the case of SPI is off, and reduced to $0.055\,\mu$m when the SPI is turned on. The reduction ratio is 1/40.

In order to estimate the actuation force required to lock the interferometer, the RMS speed of the mirror is calculated from the displacement spectra in Fig. A.3. First, the speed spectra of the mirror are calculated by multiplying the displacement spectra with ω, the angular frequency (Fig. A.4). Then by integrating the spectra, the RMS speed of the mirror is obtained; it is $450\,\mathrm{nm/s}$ when the SPI is off, and $69\,\mathrm{nm/s}$ when the SPI is turned on.

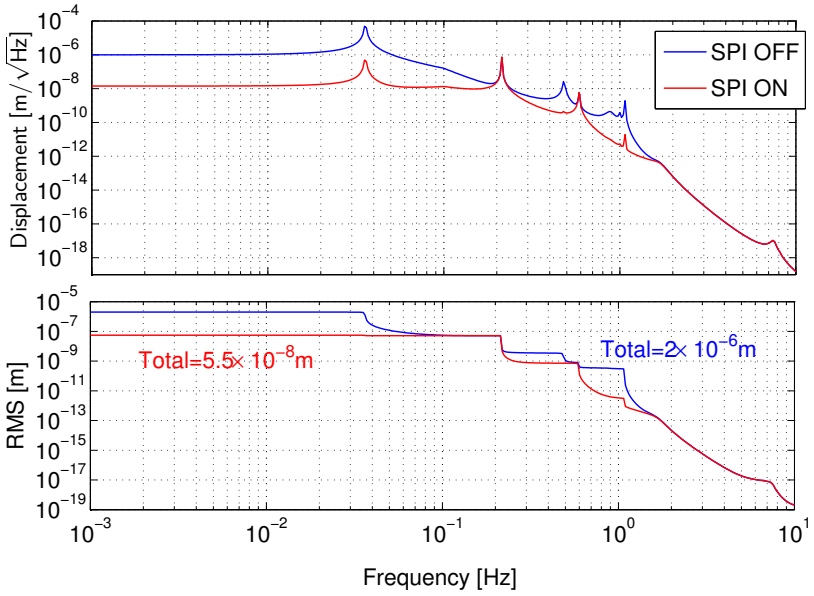

Fig. A.3: Seismic noise of LCGT without the effect of the heat links.

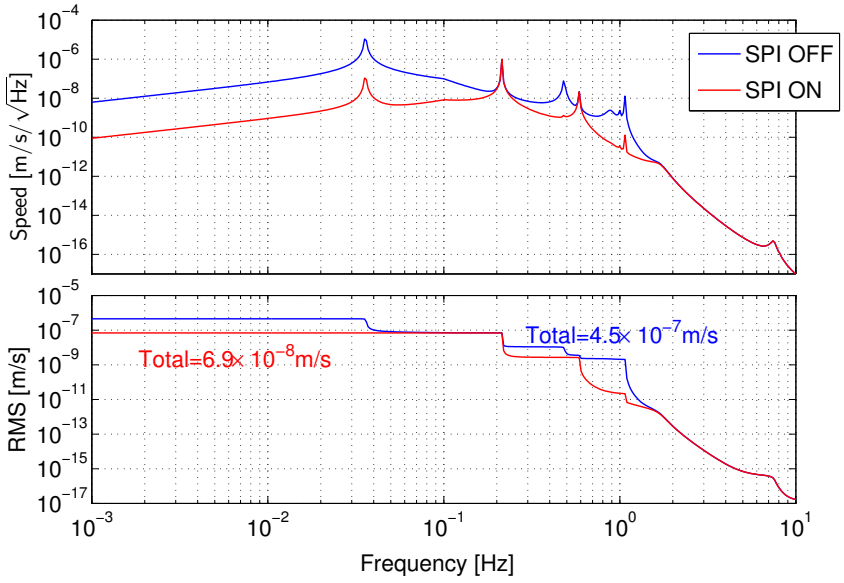

Fig. A.4: Speed spectra of LCGT mirrors.

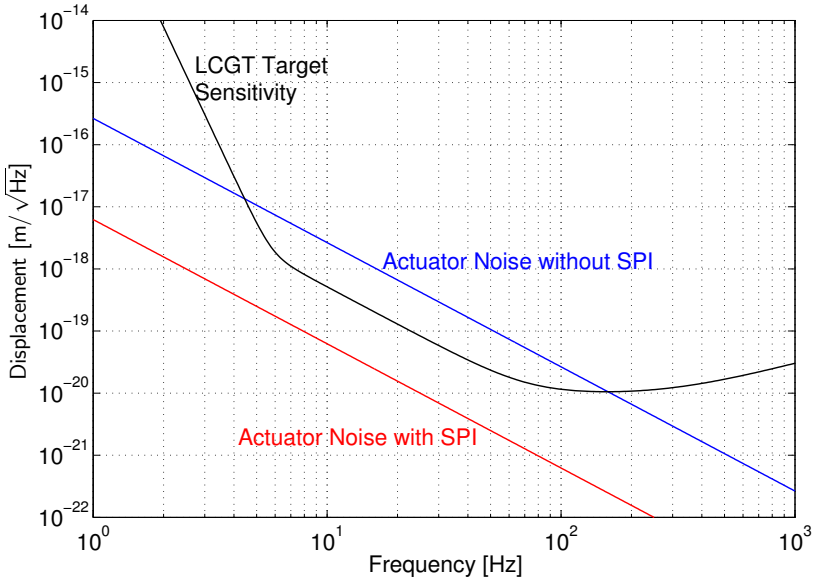

Fig. A.5: Actuator Noise of LCGT.

As discussed in section 2.5.5, the minimum force F required to lock the interferometer is related to the speed of the mirror v_{m} as,

$$F = \frac{1}{2}\frac{mv_{\mathrm{m}}^2}{d}, \tag{A.2}$$

where m is the mass of the mirror, d is the working range of the interferometer. The working range d is roughly equal to the wavelength of the laser divided by the finesse. In the case of LCGT, the wavelength is 1064 nm and the finesse is 1550. Therefore, d is 6.9×10^{-10} m. Now suppose that the required force F is produced by the actuator when the maximum input voltage V_{max} is applied to the actuator. Assuming that the actuator's output force is linear to its input voltage, the actuation coefficient, the ratio of the actuation force to the input voltage, is F/V_{max}. Using the input-equivalent voltage noise V_{n} of the actuator driver, the force noise F_{n} is given by,

$$F_{\mathrm{n}} = \frac{mv_{\mathrm{m}}^2}{2dV_{\mathrm{max}}}V_{\mathrm{n}}. \tag{A.3}$$

At the frequencies of interest, which is well above the resonance of the main pendulum, the mirror acts as a free mass. Therefore, its response to the force is $1/m\omega^2$ in frequency domain. Consequently, the displacement noise x_{n} induced by the actuator driver's noise is,

$$x_{\mathrm{n}} = \frac{v_{\mathrm{m}}^2}{2dV_{\mathrm{max}}\omega^2}V_{\mathrm{n}}. \tag{A.4}$$

The actuator noise spectra calculated by substituting the RMS speeds obtained in Fig. A.4 for $v_{\rm m}$ in the above formula are shown in Fig. A.5. Here, $V_{\rm max} = 15\,{\rm V}$, and $V_{\rm n} = 1{\rm nV}/\sqrt{\rm Hz}$ are assumed. Without the SPI, the actuators have to be so strong that the actuator noise is larger than the target sensitivity by nearly an order of magnitude. The RMS reduction by the SPI enables us to use weaker actuators. As a result, the actuator noise can be reduced well below the target sensitivity.

A.3 Works to be done for LCGT

As seen in the above sections, SPI is one of the essential technologies to attain the target sensitivity of LCGT. Given the results presented in this thesis, the next step is to design a practical SPI system for LCGT in collaboration with people working on the suspension system and the cryogenic system of LCGT. The most challenging part will be the development of an independent alignment system as discussed in section 5.2.

The optical system for the SPI also has to be considered. For example, whether the SPI will share a laser with the main interferometer or not should be decided. If the two interferometers share the same laser, the optical interference between two interferometers has to be carefully avoided. A possible solution to this problem is to shift the laser frequency for the SPI by an AOM (Acousto-Optical Modulator). If a separate laser is used for the SPI, the stabilization scheme and requirements for the laser have to be considered.

Currently, the SPI is not supposed to be operated as a recombined interferometer for the reason explained in section 2.3. However, if the stabilization of the Michelson part is required, an experimental test of the recombined operation of an SPI using a prototype interferometer like the one used in the experiment of this thesis may be needed. An assessment of this possibility is necessary.

Appendix B

Pound-Drever-Hall scheme

Pound-Drever-Hall scheme [25] is a way to obtain the deviation of the length of a Fabry-Perot cavity from the resonant condition, i.e. an integral multiple of the wavelength of the incident laser. The scheme is outlined as follows. At first, the phase of a laser beam is modulated at a certain frequency ω_{M} before injected into a cavity. Then the reflected light from the cavity is received by a photo-detector. The output of the photo detector is demodulated at the same frequency as the phase modulation. The demodulated signal is proportional to the deviation of the cavity length from the resonance. In this section the mechanism of this signal extraction scheme is described.

Suppose that a laser beam is injected into a Fabry-Perot cavity with a length L and reflectivities of the front and end mirrors, $r1$ and $r2$.[1] The electric field of the laser beam before injected into the cavity is represented as follows using its amplitude E_0 and the angular frequency of the light Ω:

$$E_{\mathrm{in}} = E_0 e^{i\Omega t}. \tag{B.1}$$

The phase of this light is modulated at angular frequency ω_{m},

$$E_{\mathrm{in}}^{\mathrm{m}} = E_0 e^{i(\Omega t + m\cos\omega_{\mathrm{m}} t)}, \tag{B.2}$$

where m is the modulation depth.

$E_{\mathrm{in}}^{\mathrm{m}}$ can be expanded by Bessel functions J_n as

$$\begin{aligned} E_{\mathrm{in}}^{\mathrm{m}} &= E_0 e^{i\Omega t} \sum_{n=-\infty}^{\infty} J_n(m)\, i^n e^{in\omega_{\mathrm{m}} t} \\ &\simeq E_0 \left[J_0(m)\, e^{i\Omega t} + iJ_1(m)\, e^{i(\Omega+\omega_{\mathrm{m}})t} + iJ_1(m)\, e^{i(\Omega-\omega_{\mathrm{m}})t} \right] \end{aligned} \tag{B.3}$$

The last approximation is valid, when $m \ll 1$. There are three frequency components in the above expression. The Ω component is called "carrier" and the other two components with frequencies $\Omega \pm \omega_m$ are called upper and lower "side bands". Now the reflectivities of the cavity for the carrier, and the upper and lower side bands are denoted by $r_{\mathrm{c}0}$, $r_{\mathrm{c}+1}$, and $r_{\mathrm{c}-1}$, respectively. Then the reflected light field is

[1] The reflectivities in this section are always amplitude reflectivities.

$$E_{\mathrm{r}} = E_0 \left\{ r_{\mathrm{c}0} J_0(m)\, e^{i\Omega t} + i J_1(m) \left(r_{\mathrm{c}+1} e^{i(\Omega+\omega_m)t} + r_{\mathrm{c}-1} e^{i(\Omega-\omega_m)t} \right) \right\}. \tag{B.4}$$

When the carrier is resonated in the cavity, $r_{\mathrm{c}+1} \simeq r_{\mathrm{c}-1} \simeq 1$.

From (1.46), $r_{\mathrm{c}0}$ is

$$r_{\mathrm{c}0} = r_1 - \frac{t_1^2 r_2 e^{-2i\delta}}{1 - r_1 r_2 e^{-2i\delta}}, \tag{B.5}$$

where $\delta = L\Omega/c$. By expanding $r_{\mathrm{c}0}$ around the resonance ($\delta = n\pi$) using $\delta' = \delta - n\pi$.

$$\begin{aligned} r_{\mathrm{c}0} &\simeq r_1 - \frac{t_1^2 r_2 (1 - 2i\delta')}{1 - r_1 r_2 (1 - 2i\delta')} \\ &\simeq r_1 - \frac{t_1^2 r_2}{1 - r_1 r_2} - i \frac{2 t_1^2 r_2 (1 - 2 r_1 r_2)}{(1 - r_1 r_2)^2} \delta'. \end{aligned} \tag{B.6}$$

Therefore,

$$E_{\mathrm{r}} = E_0 e^{i\Omega t} \left[\left(r_1 - \frac{t_1^2 r_2}{1 - r_1 r_2} - i \frac{2 t_1^2 r_2 (1 - 2 r_1 r_2)}{(1 - r_1 r_2)^2} \delta' \right) J_0(m) + 2 i J_1(m) \cos \omega_m t \right] \tag{B.7}$$

The photo detector measures the power of the reflected light as $|E_{\mathrm{r}}|^2$. By extracting the $\cos \omega_m t$ term of $|E_{\mathrm{r}}|^2$, one obtains

$$\frac{8 t_1^2 r_2 (1 - 2 r_1 r_2)}{(1 - r_1 r_2)^2} J_1(m)\, \delta' \cos \omega_m t. \tag{B.8}$$

When this signal is demodulated by an in-phase signal ($\cos \omega_m t$), a signal linearly proportional to δ' is obtained. δ' is expressed by the fluctuation ΔL of the cavity length and $\Delta\Omega$ of the laser frequency as

$$\delta' = \frac{\Delta L \Omega + L \Delta\Omega}{c}. \tag{B.9}$$

If $\Delta\Omega = 0$, the variation of the cavity length can be obtained from the signal. However, in general $\Delta\Omega \neq 0$. Therefore, the variation of the laser frequency is indistinguishable from the variation of the cavity length. For the case of the mode cleaner, L is considered to be stable ($\Delta L = 0$). In this case, the laser frequency noise can be obtained from the demodulated signal.

Appendix C

Shooting Method

C.1 Boundary Value Problem

Shooting method is a way to solve a boundary value problem of a system of ordinary differential equations numerically. This method was used to solve (3.17) (3.18). Those equations are written again below.

$$\frac{dp\left(\xi\right)}{d\xi} = G_x \sin\theta\left(\xi\right) - G_y \cos\theta\left(\xi\right) \tag{C.1}$$

$$\frac{d\theta\left(\xi\right)}{d\xi} = \gamma\left(\xi\right) p\left(\xi\right) \tag{C.2}$$

There are two parameters to be integrated, $\theta(\xi)$ and $p(\xi)$. The boundary conditions are $\theta(0) = \theta_0$ and $\theta(1) = \theta_L$. Once the initial value $p(0)$ is given, it is easy to integrate those equations from $\xi = 0$ to 1 as an initial value problem. Mathematica has a function for this purpose. However, if $p(0)$ is arbitrarily chosen, it is not guaranteed that the resultant solution satisfies the boundary condition $\theta(1) = \theta_L$. Therefore, our task is to find $p(0)$ which produces a solution satisfying $\theta(1) = \theta_L$.

Now, $\theta(1)$ can be regarded as a function of $p(0)$. This function is denoted as $\theta(1) = \theta_1(p_0)$, where $p(0)$ is shortened to p_0. Then the task is to find the root of the equation

$$\theta_1(p_0) = \theta_L. \tag{C.3}$$

Using the Newton-Rapson method, the root of the above equation can be numerically computed. During the iteration process of the Newton-Rapson method, many trial p_0 are tested by comparing $\theta_1(p_0)$ with θ_L (see Fig. C.1). This is like trying to shoot θ_L by adjusting p_0. Therefore this algorithm is called "shooting method".

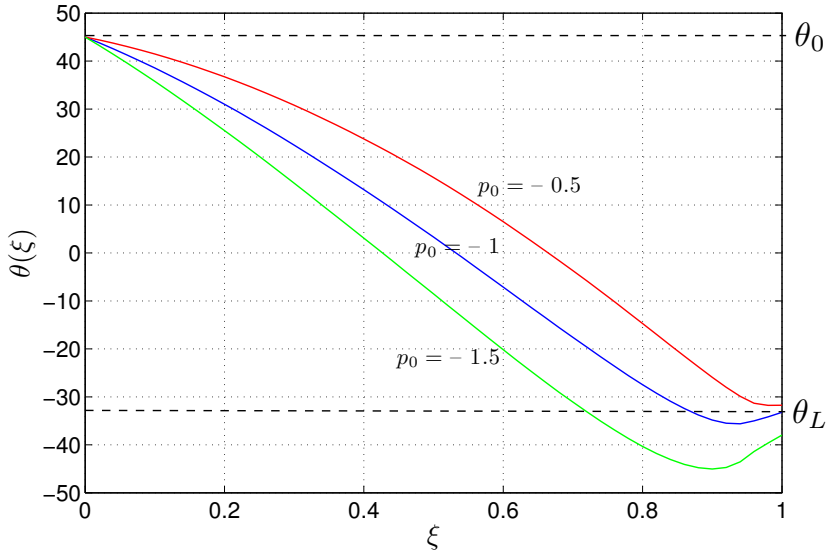

Fig. C.1: Solutions with different initial condition p_0. The blue curve ($p_0 = -1$) hits θ_L. The other curves missed the target.

C.2 Boundary Value Problem with Integral Constraint

In order to draw loci shown in Fig. 3.18, equations (C.1) (C.2) have to be solved under the constraint,

$$x_{\mathrm{t}}^{\mathrm{fix}} = \int_0^1 \cos\theta(\xi) d\xi. \tag{C.4}$$

In this case, G_x is determined as a result of the constraint.

Using the shooting method described above, the position of the blade's tip (x_t, y_t) can be calculated from (G_x, G_y). This situation can be written as functions S_x and S_y,

$$x_t = S_x\left(G_x, G_y\right), \qquad y_t = S_y\left(G_x, G_y\right). \tag{C.5}$$

Now our task is to find G_x which satisfies $x_{\mathrm{t}}^{\mathrm{fix}} = S_x\left(G_x, G_y\right)$ given a certain value of G_y. This can be accomplished by again the Newton-Rapson method. Once G_x is determined, y_t can be calculated by $S_y\left(G_x, G_y\right)$.

Appendix D

Vertical Suspension Point Interferometer

D.1 Principle

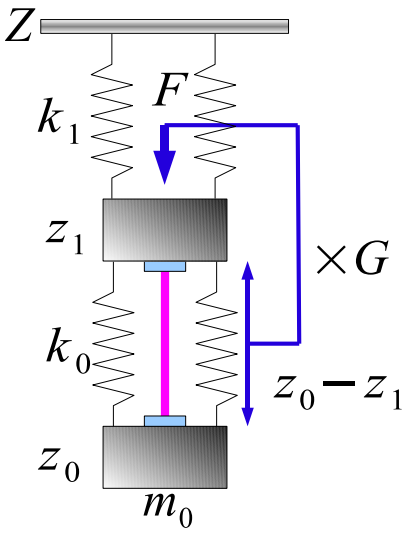

Fig. D.1: Conceptual configuration of a VSPI.

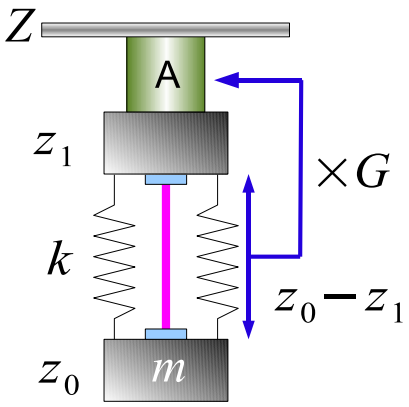

Fig. D.2: Model used for the calculation.

Vertical suspension point interferometer (VSPI) is an active vibration isolation scheme for vertical direction. It makes use of a vertically arranged Fabry-Perot interferometer as shown in Fig. D.1. The differential motion of the upper and lower stages is monitored by a vertical Fabry-Perot interferometer called VSPI. The output of the VSPI is fed back to the upper stage with a gain G. Since the lower stage is quieter than the upper one, owing to the vibration isolation by the springs connecting them, this feedback reduces the vertical

motion of the upper stage using the lower stage as an inertial reference.

To see it more clearly, consider the equations of motion of the system illustrated in Fig. D.2. For the simplicity of the calculation, the upper mass is assumed to be rigidly connected to the ground through an actuator A, whose response is so fast that the feedback quantity can be regarded not as a force but a displacement. Then the equations of motion are

$$m\ddot{z}_0 = -k\left(z_0 - z_1\right) - \gamma\left(\dot{z}_0 - \dot{z}_1\right), \tag{D.1}$$

$$z_1 = -G\left(z_1 - z_0\right) + Z. \tag{D.2}$$

Performing Fourier transformations on both sides of the above equations, one obtains the transfer function from the seismic motion Z to the motion of the lower mass z,

$$\frac{\tilde{z_0}}{\tilde{Z}} = \left\{\frac{\omega_0^2}{1+G} + i\frac{\omega_0}{(1+G)\,Q}\omega\right\} \Big/ \left\{\frac{\omega_0^2}{1+G} + i\frac{\omega_0}{(1+G)\,Q}\omega - \omega^2\right\}. \tag{D.3}$$

$$\omega_0 \equiv \sqrt{\frac{k}{m}}, \qquad Q \equiv \frac{m\omega_0}{\gamma}. \tag{D.4}$$

From this transfer function, one can see that the resonant frequency ω_0 of the system is effectively reduced by a factor of $1/\sqrt{1+G}$ and the quality factor Q is increased by a factor of $\sqrt{1+G}$. In this way, a very low vertical resonant frequency can be realized.

D.2 Experiment

To test the VSPI scheme, I constructed a small VSPI system. The experimental set up is shown in Fig. D.3. The suspension system consists of three stages. The top stage is suspended by small MGAS filters with resonant frequencies of about 1.2 Hz. At this stage, an eddy current damping is applied. The second stage is suspended from the first stage by blade springs. The input mirror of the VSPI is attached on this stage. The last stage is also suspended by blade springs from the second stage. The end mirror of the VSPI is attached on this stage. Each stage can be actuated vertically by coil-magnet actuators. The last stage is actuated from the second stage.

The light from the laser is phase modulated at 15 MHz by an EOM. Then the spatial mode of the laser is adjusted by mode matching lenses. After passing through the circulator formed by a quarter-wave plate and a PBS, the light is injected into the VSPI.

The reflected light from the VSPI is detected by a photo detector. The differential motion of the second and the third stages is obtained by demodulating the output of the photo detector at 15 MHz.

The error signal of the VSPI is fed back to the second stage through the coil-magnet actuators. However, the DC length of the VSPI cannot be changed by this feedback. Therefore, the signal is also fed back to the third stage at low frequencies.

Fig. D.4 shows the vertical transfer functions from the applied voltage to the actuators on the first stage to the displacement of the third stage measured by a photo sensor. The

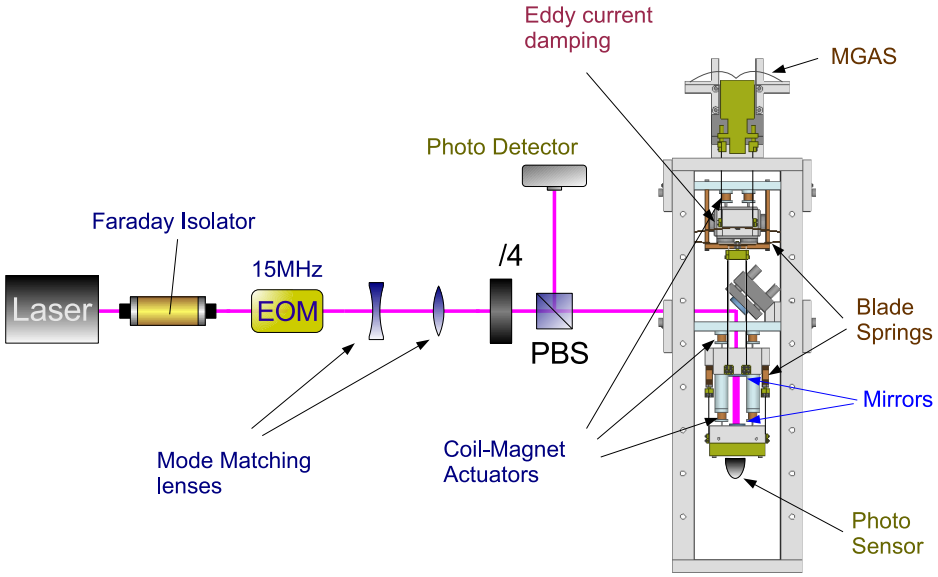

Fig. D.3: The experimental setup of the VSPI experiment.

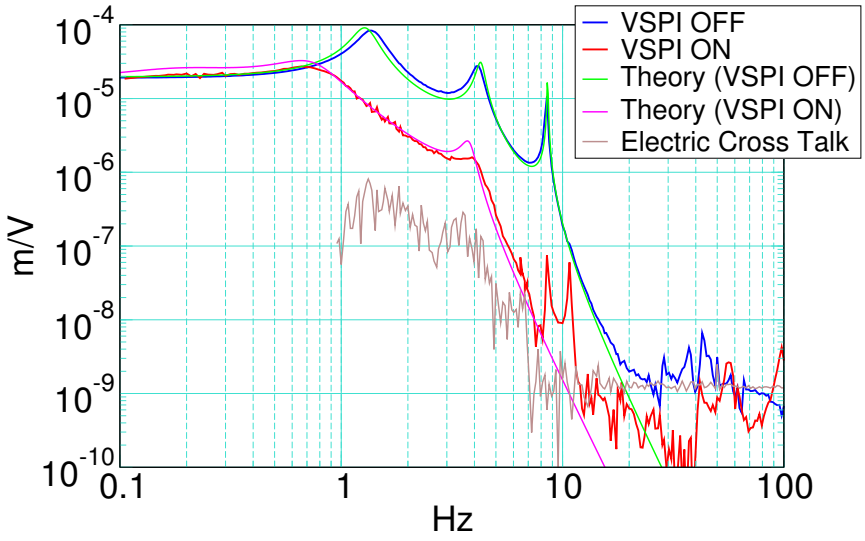

Fig. D.4: Vertical transfer functions of the suspension with and without the VSPI.

blue curve shows the transfer function measured when the VSPI is not controlled. The red curve corresponds to the transfer function when the VSPI is controlled. The vibration isolation performance is improved between 1 Hz and 20 Hz by the VSPI. The measured transfer functions are in good agreement with the theoretical predictions (the green and pink curves). Above 10 Hz, the measurements were contaminated by electric crosstalks.

With this experiment, the principle of the VSPI was confirmed. In the experiment explained in chapter 3, the MGAS filters took care of the vertical vibration isolation. If further attenuation is required, VSPI is a possible option.

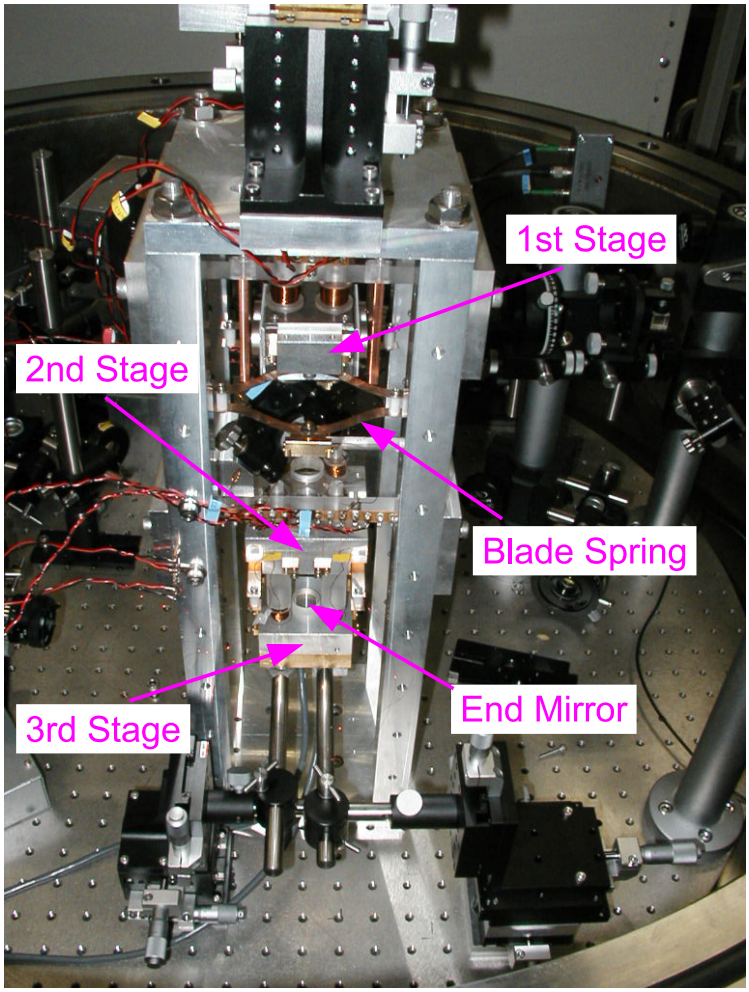

Fig. D.5: VSPI photograph

References

[1] A. Einstein, *Ann. der Phys.* **49** (1916) 769

[2] J.H. Taylor, J.M. Weisberg, *Ap. J.***345** (1989) 435

[3] R.W.P. Drever, *LIGO Document* T870001-00-R (1987)

[4] R.W.P. Drever, S.J. Augst, *Classical Quant. Grav.*, **19** (2002) 2005.

[5] V.Kalogera et al., *Astro. phys. J.*, **614** (2004) L137

[6] L. Lindblom, *Astorophys. J.* **398** (1992) 569

[7] K. Hurley et al., *Nature*, **434** (2005) 1098

[8] H. Dimmelmeier, J.A. Font and E. Müller, *Astro. Astrophys.*, **393** (2002) 523

[9] T. Nakamura, N. Mio, M. Ohashi, *Detecting gravitational waves*, Kyoto University Press (1998)

[10] C. Hogan, *Mon. Not. R. Astr. Soc.*, **218** (1986) 629

[11] R. W. P. Drever, *Fabry-Perot cavity gravity-wave detectors*, in: *The detection of gravitational waves* p. 306-328, ed: D. G. Blair, Cambridge University Press (1991) .

[12] V.B. Braginsky, F.Y. Khalili, *Quantum Measurement*, Cambridge University Press (1992)

[13] H.J. Kimble, et. al., *Phys. Rev. D*, **65** (2001) 022002

[14] H. B. Callen, T. A. Welton, *Phys. Rev.*, bf 83 (1951) 34

[15] M. Ando, K. Arai. et al.,*Phys. Rev. Lett.* **86**, 3950(2001)

[16] J. Mizuno et al., *Phys. Lett. A*, **175** (1993) 273

[17] Kuroda, et. al., *Int. J. Mod. Phys.D*, **8** (1999) 557

[18] *LCGT design document* (2003), available from http://www.icrr.u-tokyo.ac.jp/gr/LCGTdoc.pdf

[19] *Technical Report of LCGT*(2005), available from http://www.icrr.u-tokyo.ac.jp/ kuroda/review-lcgt.pdf

[20] F. J. Raab, *Class. Quantum. Grav.* **18**, 4107(2001)

[21] H. Luck, *Class. Quantum. Grav.* **14**, 1471(1997)

[22] R. Passaquieti and Virgo collaboration, *Nucl. Phys. B-Proc sup* **85**, 241(2000)

[23] L.E. Holloway,*Nucl. Phys. B Suppl.*, **54B** (1997) 176

[24] *LISA System and Technology Study Report*, ESA-SCI (2000) 11

[25] R.W.P. Drever, J.L.Hall, et al, *Appl. Phys. B* **31**, (1983) 97

[26] Y. Aso, Master's thesis, University of Tokyo (2001)

[27] Y. Aso, M. Ando, K. Kawabe, S. Otsuka, K. Tsubono, *Phys. Lett. A*, **327** (1) 1-8, 2004

[28] H.Kogelnik, T.Li, *Proc. of The IEEE.* **54**, 1312(1966)

[29] Yu. Levin, *Phys. Rev. D* **57**, 042069(1998)

[30] K. Tsubono, A. Araya, K. Kawabe, S. Moriwaki, N. Mio, *Rev. Sci. Instrum.* **64** (1993) 2237.

[31] Winterflood, D.G. Blair, *Phys. Lett. A*, **243** (1998) 1.

[32] A. Bertolini, G. Cella, R. DeSalvo, V. Sannibale, *Nucl. Instrum. Meth. A* **435** (1999) 475.

[33] G. Cella, R. DeSalvo, V. Sannibale, H. Tariq, N. Viboud, A. Takamori, *Nucl. Instrum. Meth. A* **487** (2002) 652.

[34] G. Cella, V. Sannibale, R. DeSalvo, S. Márka, A. Takamori, *Nucl. Instrum. Meth. A* **540** (2005) 502.

[35] K. Kawabe, Doctor's thesis, University of Tokyo, 1998.

[36] Y. Saito, Y. Ogawa, G. Horikoshi, N. Matuda, R. Takahashi, M. Fukushima, *Vacuum* **53** (1999) 353.

[37] M. Musha, T. Kanaya, K. Nakagawa, K. Ueda, *Opt. Comm.*, **183** (2000) 165.

[38] Y. Levin, *Phys. Rev. D*, **57** (1997) 659.

[39] A. Takamori, PhD thesis, University of Tokyo (2002).